Article

Favorable Redox Thermodynamics of SrTi$_{0.5}$Mn$_{0.5}$O$_{3-\delta}$ in Solar Thermochemical Water Splitting

Xin Qian, Jiangang He, Emanuela Mastronardo, Bianca Baldassarri, Christopher Wolverton, and Sossina M. Haile*

Read Online

ACCESS | Metrics & More | Article Recommendations | Supporting Information

ABSTRACT: Two-step, solar thermochemical splitting of water using nonstoichiometric redox-active metal oxides has emerged as an intriguing approach for large-scale hydrogen production. Perovskites have been proposed as alternatives to state-of-the-art fluorite CeO$_{2-\delta}$ because of their potential for lowering reduction temperature while maintaining high fuel productivity. Guided by computational insights, we explore the thermodynamic properties and water splitting efficacy of the cubic perovskite SrTi$_{0.5}$Mn$_{0.5}$O$_{3-\delta}$ (STM55). Thermogravimetric analysis is performed under controlled oxygen partial pressures (pO$_2$) and temperatures up to 1500 °C, from which both the enthalpy and entropy of reduction as a function of oxygen nonstoichiometry are determined. STM55 provides an attractive combination of moderate enthalpy, 200−250 kJ (mol-O)$^{-1}$, and high entropy, with unusual δ dependence. Using a water splitting cycle in which the material is thermally reduced at 1350 °C (pO$_2$, $\sim$10^{-5} atm) and subsequently exposed to steam at 1100 °C (steam partial pressure of pH$_2$O = 0.4 atm), we demonstrate a hydrogen yield of 7.4 mL g^{-1}. Through both half-cycles, the material remains largely in quasi-equilibrium with the gas phase, as reflected in the agreement of the measured data with predicted profiles based on the thermodynamic data. This behavior indicates rapid surface and bulk diffusion kinetics. Cyclic operation showed the material to be free of degradation and always resulted in a 2:1 yield of H$_2$/O$_2$. Overall, STM55 provides outstanding performance characteristics for thermochemical hydrogen production.
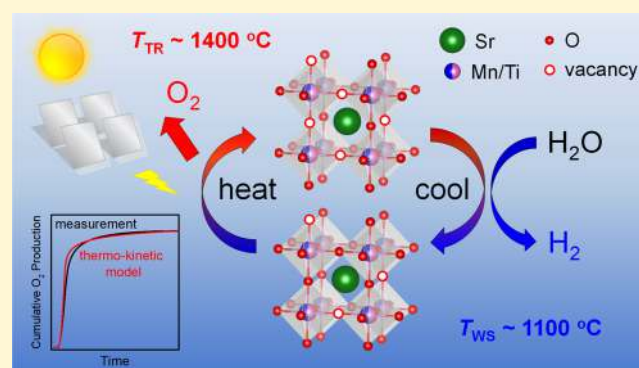
1. INTRODUCTION

Solar thermochemical generation of hydrogen via thermochemical redox cycling has emerged in recent years as a candidate route for storing the earth's vast supply of solar energy in an easily dispatched and environmentally benign form.[1,2] In its simplest embodiment, solar thermochemical hydrogen (STCH) production is a two-step process encompassing high-temperature reduction of a variable valence oxide, followed by reaction of the reduced oxide with steam. In the second, water-splitting step, typically carried out at lower temperature than the first one, the oxide preferentially removes oxygen (O$_2$) from steam to attain a more oxidized state, consequently releasing hydrogen (H$_2$). The STCH process, which includes more complex reaction schemes than that offered by variable valence oxides, is one among a broad range of approaches currently under development in pursuit of solar fuels, where chemical energy carriers are produced using sunlight as the energy source.[3−6] In comparison to these other approaches, STCH offers several advantages including utilization of the entire solar spectrum, no need for precious metal catalysts, and temporal isolation of the oxygen and hydrogen production steps (easing gas separation requirements). Implementation using variable valence oxides offers the additional advantage of

reliance on robust materials that can operate for many hundreds of cycles.

The first demonstration of technological viability of the variable valence oxide approach was achieved with ceria,[7] a material that enables not only hydrogen production but also reduction of CO$_2$ for CO and even methane production.[8] In the intervening years, the need to develop alternative STCH materials that function at reduced temperature relative to ceria has been recognized.[2] Ideally, thermal reduction can be carried out at a temperature of no more than $\sim$1400 °C so as to minimize solar re-radiation losses and ensure long lifetimes of auxiliary reactor components, without penalizing the fuel productivity (fuel generated per cycle). Perovskite-structured oxides, of generic stoichiometry ABO$_3$, have garnered significant attention in this regard.[9−12] For high-temperature thermochemical applications, the B cation is a

variable valence species, typically a transition metal, whereas the A cation is an alkaline or rare earth element. The redox properties are exquisitely tunable by partial substitution and doping on the A and B sites, and investigations of this family of compounds have given rise to materials with attractive fuel productivity. Examples include $La_xSr_{1-x}Mn_{1-y}Al_{1-y}O_{3-\delta}$[13,14] ($0 \leq x \leq 1$, $0 \leq y \leq 1$), $La_{1-x}Sr_xMnO_{3-\delta}$[15,16] ($x = 0.1–0.4$), $La_{0.6}Ca_{0.4}Mn_{0.6}Al_{0.4}O_{3-\delta}$,[17] $LaGa_{0.4}Co_{0.6}O_{3-\delta}$,[18] and the perovskite-related material $BaCe_{0.25}Mn_{0.75}O_{3-\delta}$.[19] These advances demonstrate the viability of perovskites for STCH applications and open the door toward the development of materials with even higher fuel productivity than attained to date, a key step toward high efficiency in the sunlight-to-fuel conversion process.

Given the vast composition space available for exploration within the perovskite system, one can anticipate continued progress beyond the achievements demonstrated to date, particularly if guided by insights into materials chemistry. Defining the optimal set of thermodynamic properties of a STCH material, however, remains a vexing problem. A material that readily releases oxygen in the thermal reduction step typically has a small driving force for reoxidation by steam in the water splitting step,[2] resulting in a poor steam to hydrogen conversion ratio.[15,16,20] In a temperature swing thermochemical cycle (as opposed to an isothermal cycle), this contradiction can in principle be overcome by developing a material with a large entropy of reduction.[21] To date, however, materials development efforts have largely focused on manipulating the enthalpy of reduction as a parameter that can rationally tuned by selecting elements with known oxygen binding energies[22] or by following atomistic computational predictions.[23–25] Few strategies for manipulating the entropy of reduction have emerged. The challenge, as is well known, lies in the fact that the entropy is largely dominated by the configurational entropy that results from creating oxygen vacancies.[26] Furthermore, in many cases, demonstrations of fuel productivity by direct thermochemical cycling are presented without the corresponding thermodynamic data,[19] and thus, it is difficult to assess the origins of attractive fuel yields.

In a recent study aimed at evaluating oxygen storage materials, Bulfin et al.[27] reported the thermodynamic properties of $CaMnO_{3-\delta}$ and $Ca_{0.8}Sr_{0.2}MnO_{3-\delta}$ and revealed (experimentally) that these materials display relatively large entropies of reduction. The properties of $CaMnO_{3-\delta}$ are in general agreement with the results obtained by the present authors in a study of candidate thermochemical heat storage materials.[28] Perovskites of the form $AMnO_3$, in which A is an alkaline earth metal, have historically received less attention than those in which A includes partial or complete substitution with a lanthanide,[29–31] and thus, their thermodynamic properties are relatively poorly characterized. The potential of such materials for thermochemical applications has been suggested in recent computational studies of a large chemical space of $A(B'B'')O_3$[32] and $(A'A'')(B'B'')O_3$[24] materials in which A-site cations are alkaline earth elements and B′ and B″ include transition metal elements, and promising experimental results have been reported from $BaCe_{0.25}Mn_{0.75}O_3$,[19] a hexagonal perovskite-related material. Among the end member $AMnO_3$ compounds (A = Mg, Ca, Sr, or Ba), only $CaMnO_3$ adopts a perovskite-type structure under ambient conditions, in this case with an orthorhombic distortion.[33] No compound of stoichiometry $MgMnO_3$ appears in the literature, whereas $SrMnO_3$ and $BaMnO_3$ adopt hexagonal structures related to hexagonal $BaTiO_3$.[33] Although the high entropy of reduction of $CaMnO_{3-\delta}$ renders it attractive as a STCH material, it suffers

from a relatively low enthalpy of reduction, particularly in the cubic phase (the structure adopted upon slight reduction), implying a thermodynamic constraint on the water splitting step. Moreover, the thermal stability of this material is relatively poor.[28]

In this work, we examine $SrTi_{0.5}Mn_{0.5}O_{3-\delta}$ (STM55) as a candidate STCH material that may retain the high entropy benefits of $CaMnO_{3-\delta}$-based compositions, as well as their rapid kinetics,[27] while overcoming the disadvantages of too low enthalpy and poor thermal stability. First, STM55 (unlike $CaMnO_3$) is known to adopt the cubic perovskite structure at room temperature,[34] and consequently, potential mechanostructural challenges associated with crystallographic phase changes from lower symmetric phases upon heating are avoided. Second, based on the understanding of enthalpy trends now evident in the perovskite literature,[14,22–24] we anticipate that partial substitution of Mn with less reducible Ti will increase the enthalpy to a more desirable value and that this will also outweigh the lower enthalpy anticipated by replacing Ca with Sr. The potential influence of Sr is expected from the experimental observation that cubic $SrMnO_3$ has a lower enthalpy than cubic $CaMnO_{3-\delta}$.[35] Third, because the entropy values reported by Bulfin et al. for $CaMnO_3$ and $Ca_{0.8}Sr_{0.2}MnO_3$ are equal to one another within experimental uncertainty,[27] we anticipate that the large entropy of reduction observed in $CaMnO_3$ will be retained in an Sr analogue. A relatively high entropy in alkaline earth-rich manganite perovskites is further suggested by the trends in the experimentally measured properties of $La_{1-x}Sr_xMnO_3$.[36] In brief, STM55 is pursued because of its potentially ideal characteristics, specifically, high entropy of reduction, moderate enthalpy of reduction, good thermal stability, and cubic phase across the operating regime, for STCH applications.

The work presented here encompasses a comprehensive thermochemical evaluation of STM55. From a combination of in situ and ex situ X-ray powder diffraction studies, we establish the thermal stability of the cubic perovskite phase. We perform ab initio computation to evaluate the hypothesis that cubic STM55 will have a greater enthalpy of reduction than cubic $CaMnO_{3-\delta}$. Using thermogravimetric analysis (TGA), we measure the oxygen nonstoichiometry (δ) over a range of temperatures and oxygen partial pressures (pO_2) and analyze these data to extract the model-independent enthalpy and entropy of reduction as a function of nonstoichiometry. We further carry out reactor-based hydrogen production experiments over a range of cycling conditions. By comparison to gas evolution quantities predicted from the thermodynamic data, we find that the macroscopic fuel production rate over STM55 is largely limited by thermodynamic parameters rather than material kinetic parameters, with the latter becoming important when the temperature of the water splitting step is reduced. Although the fuel productivity naturally depends on the details of the cycle employed, as one example, we achieve a hydrogen productivity of 8.3 mL g^{-1} in a cycle involving thermal reduction at 1400 °C, water splitting at 1100 °C, and a total cycle time of 90 min. These results render STM55 a competitive material for thermochemical hydrogen production and underscore the importance of quantitative thermodynamic measurements to both predict fuel production profiles under realistic cycling conditions and guide insights for future materials engineering.

2. RESULTS AND DISCUSSION

2.1. Synthesis and Phase Stability.
The material STM55 was synthesized by a solid-state reaction at 1400 °C under air (Section A: Methods, Supporting Information). As evident from
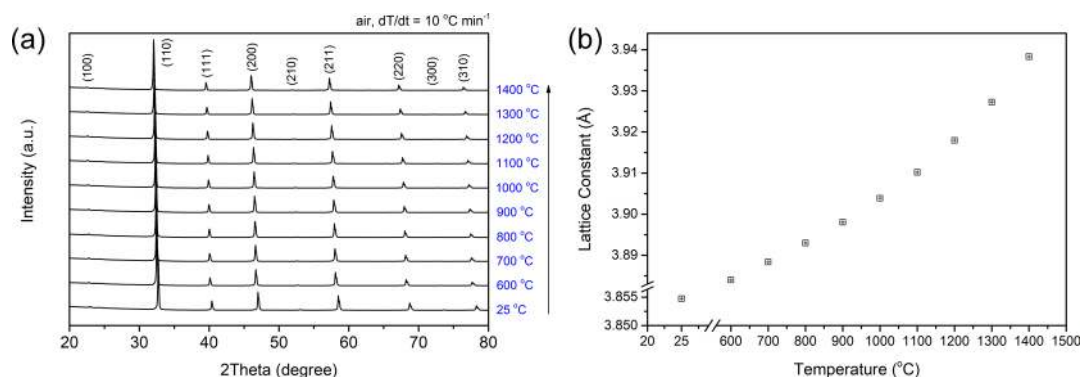
Figure 1. High-temperature in situ XRD of $SrTi_{0.5}Mn_{0.5}O_3$ under air: (a) diffraction patterns obtained at the temperature indicated, upon heating, with peaks indexed, and (b) refined lattice parameter, reflecting influences of both thermal and chemical expansion. Chemical expansion becomes important above ~900 °C.

the XRD data (Figure S1, Supporting Information), the material adopts the archetypical cubic perovskite crystal structure, with Ti and Mn randomly distributed on the B site, and no evidence of ordering. Porous monoliths (~51% porosity) for thermal analysis and thermochemical cycling were prepared by lightly pressing the STM55 powder and sintering at 1400 °C (2 h, under air). Elemental analysis by energy-dispersive X-ray spectroscopy (EDS) broadly confirmed that the targeted stoichiometry had been attained (Figure S2b, Supporting Information). Quantitative chemical analysis by inductively coupled plasma optical emission spectrometry (ICP-OES) revealed a Sr/Ti/Mn ratio of 1:0.539:0.490, slightly deficient in Sr and rich in Ti relative to the target composition, a factor accounted for in subsequent interpretation of the TGA data. The overall stoichiometry at a reference state selected for TGA (1000 °C and $pO_2 = 0.075$ atm) was further evaluated via a complete reduction experiment in which the material was exposed to 3% H_2 (balance Ar) at 1000 °C (Figure S3a, Supporting Information). X-ray diffraction (XRD) analysis of the product revealed a mixture of MnO, Sr_2TiO_4, and a small amount of $Sr_3Ti_2O_7$, with phase fractions in quantitative agreement with the ICP chemical analysis (Figure S3b, Supporting Information). Recognizing that A-site vacancies are the most common cation defect type in perovskites,[37] the stoichiometry of the fully oxidized material is deduced to be $Sr_{0.97}Ti_{0.53}Mn_{0.47}O_{2.97}$ (with an uncertainty of ~3% in each elemental stoichiometry). Hereafter, the oxygen nonstoichiometry is reported relative to this deduced stoichiometry, which differs slightly from the target composition of $SrTi_{0.5}Mn_{0.5}O_3$ for the fully oxidized state. For notational convenience, we retain the acronym STM55 to refer to the material characterized in this work.

The phase stability of STM55 on heating under air was evaluated by in situ X-ray powder diffraction. The lattice constant increases smoothly from 3.8548(1) Å at ambient temperature to 3.9383(1) Å at 1400 °C, Figure 1, with no indication of phase change or decomposition. Ex situ diffraction measurements of the material after exposure to temperatures as high as 1600 °C under air and as high as 1500 °C under an oxygen partial pressure as low as 4.00×10^{-5} atm (Table S1, Supporting Information) showed the presence of only the cubic phase (Figure S4, Supporting Information). The behavior is generally consistent with the high thermal stability of the end member compounds $SrMnO_3$ (stable to 1740 °C under air[38]) and $SrTiO_3$ (stable to 2050 °C under air[39]). The morphological stability of the porous structure used for fuel production in thermochemical cycling was evaluated by

scanning electron microscopy (SEM) imaging before and after completion of the cycling experiments.

2.2. Thermodynamics of Reduction. Our speculation that the enthalpy of reduction of STM55 will be higher than that of (cubic) $CaMnO_3$ is supported by density functional theory (DFT) studies performed as part of a broader computational effort to screen perovskite oxides for suitable vacancy formation energetics.[32] This approach was first validated by evaluating the computed enthalpy of $AMnO_3$ compounds and comparing them to experimental results. In the case of $CaMnO_3$, the computed vacancy formation energy in the ground-state orthorhombic structure is 222 kJ $(mol\text{-}O)^{-1}$, identical to the experimental value [also ~222 kJ $(mol\text{-}O)^{-1}$].[28] To simplify the calculations of STM55, we use a small (10−20 atoms) perovskite supercell, cubic Sr_2TiMnO_6 ($Fm\overline{3}m$), with a rock-salt-ordered arrangement of Ti and Mn cations. This choice is motivated by the observation that nearly all the ordered B-site perovskites are rock-salt-ordered.[40] Recognizing that the experimental structure shows a disordering of B-site cations, we computed the oxygen vacancy formation energy for each of the symmetry-distinct oxygen atoms in different Wyckoff positions. We find only a modest difference in oxygen vacancy formation energy [less than 10 kJ $(mol\text{-}O)^{-1}$] across these sites, suggesting that the impact of ordering on the computed energies is small. We take the lowest value result from this analysis, ~310 kJ $(mol\text{-}O)^{-1}$, to be representative of the material behavior. As anticipated, this value is distinctly higher than the experimentally observed enthalpy of reduction of ~173 kJ $(mol\text{-}O)^{-1}$ in cubic $CaMnO_{2.9}$.[28]

Turning to the experimental studies, mass loss profiles were recorded up to a temperature of 1500 °C under 10 different oxygen partial pressure conditions between 0.208 and 3.00×10^{-5} atm, Table 1. Because TGA yields the relative change of mass of a sample, a measurement under the reference state conditions (1000 °C and $pO_2 = 0.075$ atm) was included as part of each suite of TGA experiments. A relatively large sample (1.388 g) was employed so as to maximize the absolute mass change and hence achieve high sensitivity. In the low oxygen partial pressure conditions, it was observed that because of the large size, the volume of oxygen released from the sample released caused the sample environment to deviate from that of the inlet gas. Rather than employing excessively low heating rates to alleviate this problem, a stepped heating protocol involving 100 °C steps with 1−4 h of hold times and numerical extrapolation to equilibrium behavior was implemented. For measurements under an oxygen partial pressure of 0.0087 atm and higher, a ramp rate of 2 °C min^{-1} was found to be sufficiently slow that the sample

Table 1. Experimental Protocol for Thermogravimetric Measurements of STM55^a

oxygen partial pressure, atm flow rate: 250 mL min^{-1}	temperature range, °C ramp rate: 2 °C min^{-1}	method and hold time, h
0.208(2)	300–1500	continuous
0.150(2)	300–1500	continuous
0.075(3)	300–1500	continuous
0.028(1)	300–1500	continuous
0.0087(1)	300–1500	continuous
0.0046(1)	300–1500	stepped, 1 or 2
$8.19(3) \times 10^{-4}$	900–1500	stepped, 2
$2.14(4) \times 10^{-4}$	900–1500	stepped, 3
$9.79(9) \times 10^{-5}$	1000–1500	stepped, 4
$3.00(8) \times 10^{-5}$	1000–1500	stepped, 4

^{a}The mass change of the ~1.388 g sample was sufficiently rapid in the higher pO_2 range to enable accurate data collection under continuous heating. At low pO_2, measurements were recorded in 100 °C steps using long hold times, as indicated. The number in parenthesis is the uncertainty in the final digit of the oxygen partial pressure value.

environment was not perturbed by the oxygen release. Shown in Figure 2 are example profiles for the two regimes. At $pO_2 = 0.0087$ atm (Figure 2a), the overlap of the data in heating and cooling steps provides the evidence that the equilibrium values of mass have been recorded. Furthermore, the experimentally measured oxygen partial pressure remains at the inlet value. In the case of measurement under $pO_2 = 0.0046$ atm (Figure 2b), increases in oxygen partial pressure that relax back toward the inlet value are evident for each heating step. The complete set of thermogravimetric measurements and oxygen nonstoichiometry analyses, including extrapolation protocols for low pO_2 conditions, are presented in Figures S5–S8 (Supporting Information).

The oxygen nonstoichiometry profiles implied by TGA are summarized in Figure 3a. The thermodynamic functions, the enthalpy and entropy of reduction, were obtained from analysis of nonstoichiometry behavior according to the van't Hoff method.[41] Specifically, the reduction of an ABO$_3$ perovskite can be written as

$$\frac{1}{\Delta\delta}ABO_{3-\delta_i} \rightarrow \frac{1}{\Delta\delta}ABO_{3-\delta_f} + \frac{1}{2}O_2 \tag{1}$$
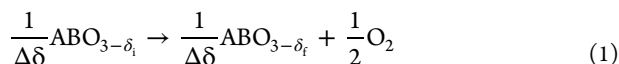
where $\Delta\delta = \delta_f - \delta_i$ is the change in oxygen nonstoichiometry between the initial and final values. In the limit $\Delta\delta \rightarrow 0$, $\Delta_{red}G^\Theta(T,\delta)$, the standard Gibbs energy of reduction at specified δ is given by

$$\Delta_{red}G^\Theta(T, \delta) = -RT \ln(K_{red}^{eq}) = -RT \ln(\hat{p}O_2)^{1/2}$$
$$= \Delta_{red}H^\Theta(\delta) - T\Delta_{red}S^\Theta(\delta) \tag{2}$$

in which R is the universal gas constant, T is the temperature, and K_{red}^{eq} is the equilibrium reaction constant. The quantity $\hat{p}O_2$ is pO_2/p_{ref}, equal to the oxygen partial pressure, pO_2, referenced to the standard pressure, $p_{ref} = 1$ atm. $\Delta_{red}H^\Theta(\delta)$ and $\Delta_{red}S^\Theta(\delta)$ are the standard enthalpy and entropy of reduction, respectively, defined on a per mole (or atom) of oxygen basis. Rearranging eq 2 yields

$$R \ln(\hat{p}O_2)^{1/2} = -\frac{\Delta_{red}H^\Theta(\delta)}{T} + \Delta_{red}S^\Theta(\delta) \tag{3}$$

If $\Delta_{red}H^\Theta(\delta)$ and $\Delta_{red}S^\Theta(\delta)$ are independent of temperature, as is often observed, an Arrhenius plot of a set of $T-pO_2$ pairs at a given δ yields a linear curve, with the enthalpy and entropy of reduction given by the slope and intercept, respectively.

Examples of isostoichiometric sets of data along with the linear fits ($R^2 > 0.99$ in all cases) are displayed in Figure 3b. The enthalpy and entropy of reduction for STM55 extracted from the analysis are shown in Figure 4, along with the analogous data for ceria,[41] La$_{0.6}$Sr$_{0.4}$MnO$_{3-\delta}$ (LSM64),[36] and CaMn$_{0.9}$Fe$_{0.1}$O$_{2.95-\delta}$ (CMF91).[28] The noise in the $\Delta_{red}H^\Theta(\delta)$ and $\Delta_{red}S^\Theta(\delta)$ functions of STM55 at high δ results from the required transition to discrete TGA data at low pO_2. In addition, slight jumps in the thermodynamic functions occur at δ values at which the number of $\delta(T)$ profiles contributing to the analysis decreases from, for example, 5 to 4.

Consistent with the targeted behavior, the enthalpy of reduction of STM55 is higher than that of undoped or lightly B-site-doped alkaline manganites such as CMF91[28] (shown in Figure 4a), CaMnO$_3$ [178,[22] 175,[35] 161 kJ (mol-O)$^{-1}$,[27] and SrMnO$_3$ [147 kJ (mol-O)$^{-1}$].[22] Furthermore, it is smaller than that of LSM64 (Figure 4a), consistent with computational and experimental results which show that the reduction enthalpies in La$_{1-x}$Sr$_x$BO$_3$ decrease with increasing Sr content.[23,42–45] The enthalpy of STM55 is approximately linear with δ, as is commonly observed in perovskites,[43] and is described by

$$\Delta_{red}H^\Theta(\delta) = 196.1 \pm 0.6 + (276 \pm 5) \times \delta \text{ kJ (mol-O)}^{-1} \tag{4}$$

Because the complete reduction experiment yielded product phases with Ti retained in the 4+ oxidation state (Figure S3, Supporting Information), this enthalpy reflects the redox activity
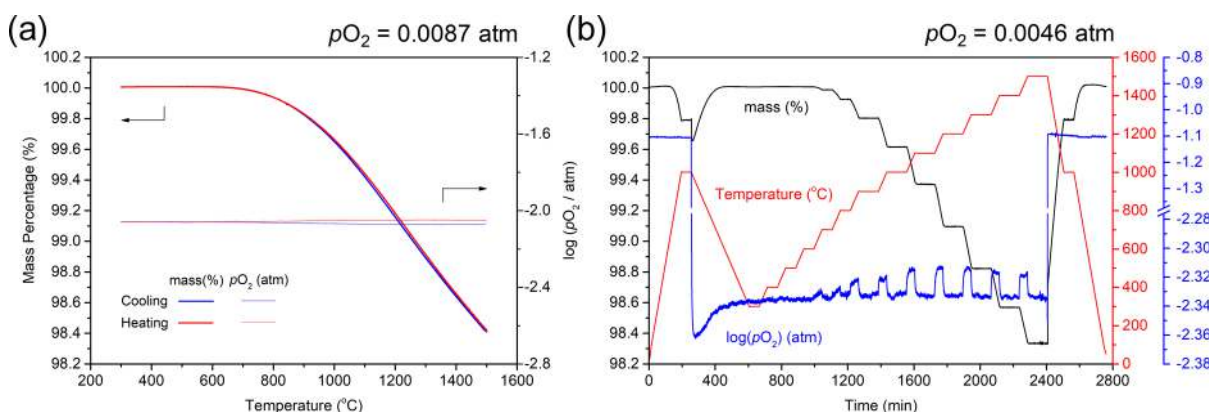

Figure 2. Representative thermogravimetric results for the quantification of STM55 nonstoichiometry as a function of T and pO_2: (a) mass and pO_2 profiles during heating and cooling under an experimental inlet $pO_2 = 0.0087$ atm using a continuous heating protocol, $m_0 = 1388.02$ mg, and (b) mass, temperature, and pO_2 profiles under an experimental inlet $pO_2 = 0.0046$ atm using a stepped heating protocol, $m_0 = 1387.94$ mg.

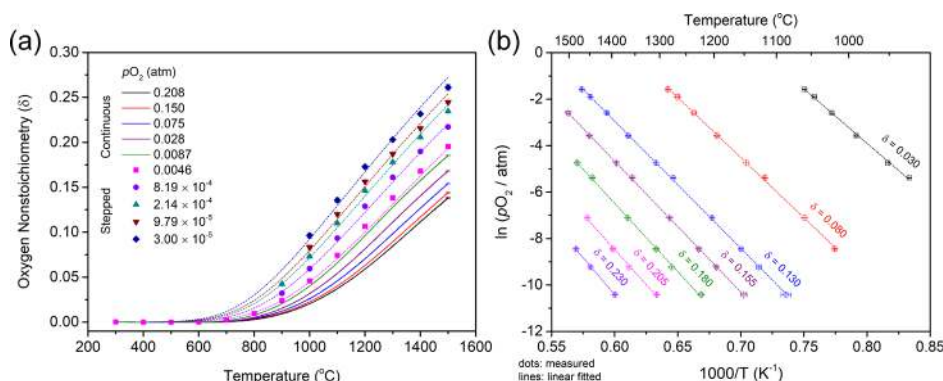**Figure 3.** Oxygen nonstoichiometry of STM55 as a function of temperature and oxygen partial pressure: (a) δ as a function of T at each pO_2 of measurement (Table 1), showing results from both continuous heating (solid lines) and stepped heating (symbols) profiles, and (b) Arrhenius representation isostoichiometric conditions at representative δ between 0.030 and 0.230 as employed for extraction of thermodynamic properties by the van't Hoff method. Dashed lines in (a) overlaying the discrete data from stepped heating are computed from the fitted thermodynamic parameters reported in Figure S9 (Supporting Information).
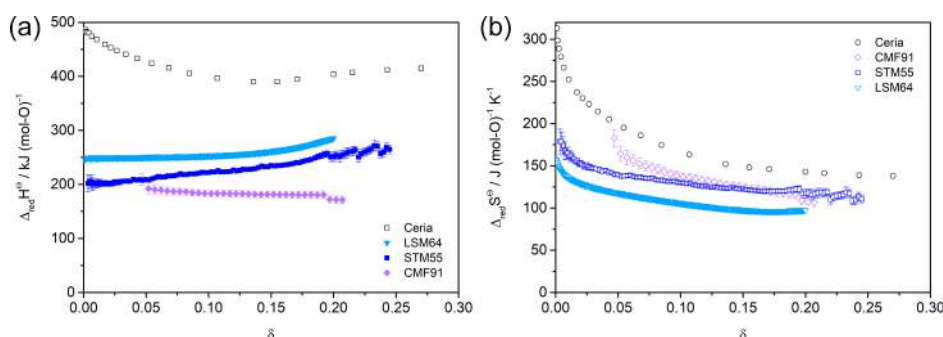

Figure 4. Thermodynamic properties of STM55 (this work) as compared to selected other materials for which data over a similar δ range is available: (a) enthalpy and (b) entropy of reduction. Data sources: ceria, Panlener et al.;[41] LSM64 (=La$_{0.6}$Sr$_{0.4}$MnO$_{3-\delta}$), Ignatowich et al.;[36] and CMF91 (=CaMn$_{0.9}$Fe$_{0.1}$O$_{2.95-\delta}$, for clarity, only data for the cubic phase are shown), Mastronardo et al.[28]
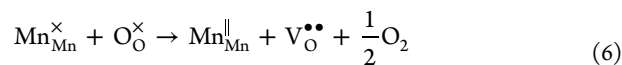
of Mn. As the inherent affinity between Mn and O is fixed, the influence of Ti on STM55, shifting the enthalpy of reduction to a higher value than in SrMnO$_3$, may derive from its influence on the electronic structure and energetics of electronic defect formation. The DFT calculation, as discussed above, predicts a slightly higher enthalpy [$\sim$308 kJ (mol-O)$^{-1}$] than that measured experimentally. The discrepancy may be due to the challenges of assigning the value of the Hubbard correction factor U for the Mn^{4+} species,[32] the appropriate value of which may vary depending on the influence of other B site atoms.

Turning to the entropy, here also, the behavior follows the targeted outcome. The entropy of reduction of STM55 is generally comparable to that of CMF91, albeit with a distinct functional form. It is substantially larger than in LSM64, a material with competitive thermodynamic properties for STCH applications. The entropy of reduction in variable valence oxides depends on nonstoichiometry as a consequence of the changing number of configurations available to the system as the number of vacancies changes. The functional form of $\Delta_{\mathrm{red}}S^{\Theta}(\delta)$ is highly sensitive to the nature of the defects, the extent of their interactions, and in the case of electronic defects, the extent of localization. Here, the entropy of reduction of STM55 is surprisingly well described by

$$\Delta_{\mathrm{red}}S^{\Theta}(\delta) = -2R \ln\left(\frac{\delta}{3-\delta}\right) + \Delta S_O^{\mathrm{excess}}$$

$$\Delta S_O^{\mathrm{excess}} = 72 \pm 2 \text{ J (mol-O)}^{-1} \text{ K}^{-1} \qquad (5)$$

a function that obeys the expected divergence in entropy at $\delta \to 0$. Although development of a complete model that rationalizes this result is beyond the scope of this work, we note that a reduction reaction that predominantly produces localized Mn^{2+} species according to

$$\mathrm{Mn}_{\mathrm{Mn}}^{\times} + \mathrm{O}_O^{\times} \to \mathrm{Mn}_{\mathrm{Mn}}^{\parallel} + \mathrm{V}_O^{\bullet\bullet} + \frac{1}{2}\mathrm{O}_2 \qquad (6)$$

(expressed in Kroger−Vink notation) would yield a configurational entropy described by the first term in eq 5. For the purposes of assessment of the thermochemical fuel productivity, the data are expressed according to a function with polynomial terms in addition to those in eq 5 (shown in Figure S9, Supporting Information).

2.3. Thermochemical Hydrogen Production. *2.3.1. Equilibrium Fuel Productivity.* On the basis of the thermodynamic data, it is possible to compute the nonstoichiometry of STM55 at almost any arbitrary condition. Thus, it is also possible to compute the equilibrium fuel productivity for any given cycle, where equilibrium productivity is that which results from allowing the oxide to react with the supplied gas for a sufficiently long time that equilibrium is achieved. Shown in Figure S10 (Supporting Information) are the expected equilibrium fuel production values for thermal reduction (eq 1) under a sweep gas of 10 ppm O$_2$ in Ar at temperatures, T_{TR}, between 1200 and 1400 °C, and the water splitting step
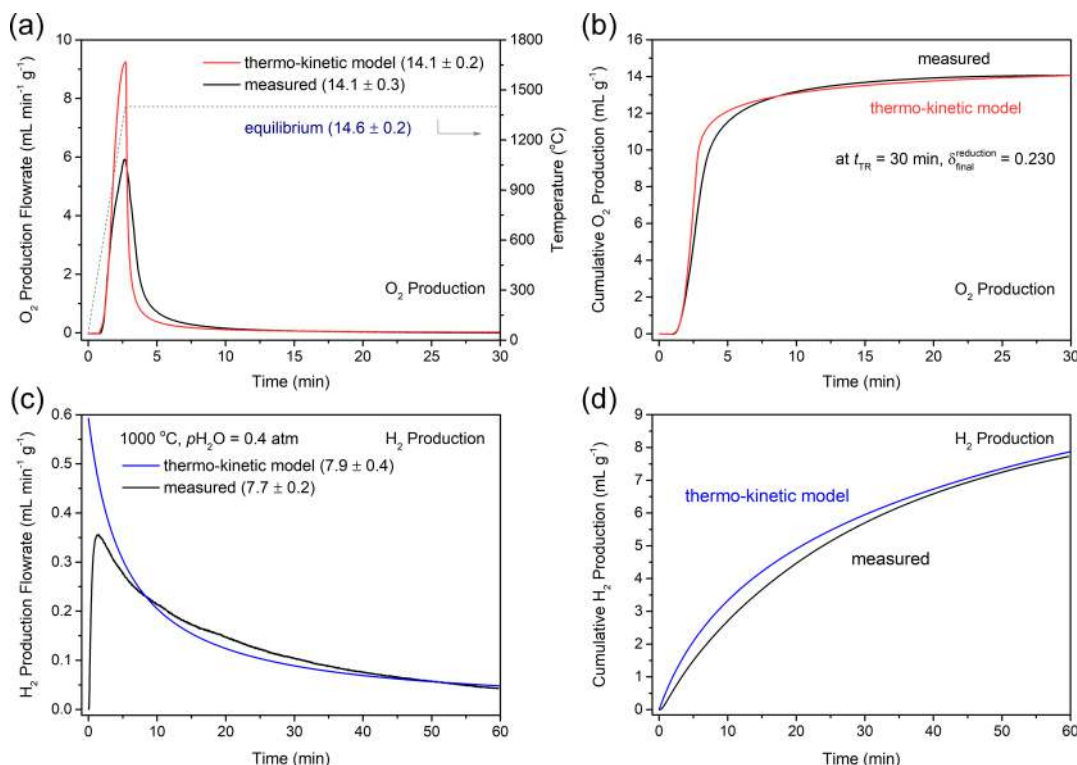
Figure 5. Experimental and predicted gas evolution characteristics of STM55 under (a,b) thermal reduction and (c,d) water splitting. See text for model description and Figure S12 (Supporting Information) for complete experimental details. The relatively good agreement between model and experiment indicates the reactions that are largely limited by the rate at which gas is supplied (thermokinetic model) rather than by material kinetic factors.
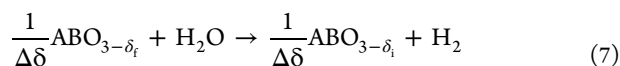
$$\frac{1}{\Delta\delta}ABO_{3-\delta_f} + H_2O \rightarrow \frac{1}{\Delta\delta}ABO_{3-\delta_i} + H_2 \qquad (7)$$

performed at a variable temperature, T_{WS}, between 800 and 1200 °C, using a steam partial pressure of either $pH_2O = 0.2$ or 0.4 atm. For consistency with eq 1, the nonstoichiometry at the completion of the reduction step (initiation of the water splitting step) is denoted as δ_f. The calculation requires slight extrapolation to more reducing conditions than experimentally accessed in the TGA measurements. This is implemented by extrapolating the $\Delta_{red}H^{\ominus}(\delta)$ and $\Delta_{red}S^{\ominus}(\delta)$ functions to a slightly larger δ than those shown in Figure 4 (see Figure S9, Supporting Information) and correspondingly slightly lower pO_2 than those examined experimentally, as shown in Figure 3a.

The prediction summarized in Figure S10 (Supporting Information) represents the upper bound for fuel productivity because allowing the system to reach equilibrium is rarely optimal for realistic reactor operation. Nevertheless, the values are very high and merit comment. For example, for a cycle in which reduction is carried out at 1400 °C under inert gas (10 ppm O_2 in Ar) and oxidation is carried out at 1000 °C with $pH_2O = 0.4$ atm, δ is predicted to swing between 0.256 and 0.113, respectively, with a corresponding hydrogen production of 17.4 mL g^{-1}. Motivated by this analysis, several experiments in which hydrogen production was directly measured were performed.

2.3.2. Half-Cycles for Predictable Hydrogen Production. In a first set of experiments, two half-cycles were carried out by initiating reduction of STM55 from its fully oxidized state, attained by first oxidizing the material at ambient temperature according to the experimental protocol shown in Figure S11 (Supporting Information). In this way, it was possible to directly compare gas evolution behavior against thermodynamic expectations and assess the extent to which material kinetics influence

the fuel production rate. The gas evolution profiles were predicted within the framework of a quasi-equilibrium or thermokinetic model we have presented previously.[46,47] In brief, when surface reaction and bulk diffusion rates are fast relative to the mass-normalized gas flow rate, the material can remain in quasi-equilibrium with the gas phase. In such case, the rate of reaction becomes limited by the rate of gas-phase mass transport. If, in addition, the temperature across the oxide and the composition of the gas phase in the oxide vicinity are spatially invariant during the half-cycle of interest, a situation encountered when the sample is small relative to the heating zone and when high porosity in the solid enables easy gas access, the oxygen nonstoichiometry in the oxide will also be spatially invariant. The rate of change of the oxygen nonstoichiometry upon thermal reduction, $d\delta_{red}/dt$, under these conditions and at a given thermal reduction temperature, T_{TR}, is described according to[46]

$$\frac{d\delta_{red}}{dt} = \frac{2F_{TR}}{n_{oxide}} \frac{(pO_2(\delta,\ T_{TR}) - pO_2^{TR})}{(p_{tot} - pO_2(\delta,\ T_{TR}))} \qquad (8)$$

in which n_{oxide} is the number of moles of the oxide (STM55 in this study), F_{TR} is the molar flow rate of the gas supplied in the thermal reduction step, pO_2^{TR} is the oxygen partial pressure of the supplied reduction gas, p_{tot} is the total pressure (set at 1 atm), and $pO_2(\delta,T_{TR})$ describes the relationship between the instantaneous pO_2 and δ at the reduction temperature as given in eq 3. The temperature ramp during reduction is readily treated by applying an appropriate increment in temperature with each time step of the calculation.

The analogous expression for the rate of change of the oxygen nonstoichiometry in the water splitting half-cycle, $d\delta_{ox}/dt$, at a given temperature, T_{WS}, is given as

Table 2. Results of Thermochemical Cycling Studies Performed under the Multicycle Conditions Indicated[a]

figure & cycle ID		mass (g)	T_{TR} (°C)	V_{TR} (mL min⁻¹)	T_{WS} (°C)	pH₂O (atm)	t_{WS} (min)	peak H₂ (mL min⁻¹ g⁻¹)	cumulative H₂ (mL g⁻¹)	peak O₂ (mL min⁻¹ g⁻¹)	cumulative O₂ (mL g⁻¹)	H₂/O₂ ratio
S13	M1	0.5225	1400	500	800	0.2	60	0.22(1)	3.7(1)	1.17(4)	1.9(1)	2.0(1)
S14	M2	0.5225	1400	500	1000	0.2	60	0.30(2)	5.3(1)	1.31(6)	2.6(1)	2.0(1)
S15	M3	0.5225	1400	500	1000	0.4	60	0.50(4)	6.9(1)	2.48(8)	3.4(2)	2.0(1)
6	M4	0.5225	1400	500	1100	0.4	60	0.39(1)	8.3(1)	1.16(3)	4.1(1)	2.0(1)
S16	M5	0.5225	1400	500	1200	0.4	60	0.28(1)	6.0(1)	0.57(2)	3.0(1)	2.0(1)
S17	M6	0.5225	1350	1000	1100	0.4	60	0.24(2)	6.3(1)	0.62(2)	3.2(2)	2.0(1)
S18	M7	0.2529[b]	1350	1000	1100	0.4	60	0.46(2)	7.4(1)	4.09(14)	3.7(2)	2.0(1)
S19	M8	0.5225	1350	500	1100	0.4	15	0.20(1)	2.3(2)	0.13(2)	1.2(1)	2.0(1)
S20	M9	0.5225	1350	1000	1100	0.4	15	0.26(2)	3.0(2)	0.21(4)	1.5(2)	2.0(1)
S21	M10	0.2529[b]	1350	1000	1100	0.4	15	0.48(3)	3.8(1)	1.82(9)	1.9(1)	2.0(1)

[a]Reduction is carried out under 10 ppm O₂ ($pO_2 = 10^{-5}$ atm) for 30 min and oxidation (water splitting) is carried out under a flow rate of 300 mL min⁻¹ of Ar using a porous monolith sample of STM55 with mass as indicated. Number in parentheses is the uncertainty in the final digit obtained from the spread in values over the 8−10 cycles. [b]Varying the mass has the effect of varying the mass normalized flow rate during both thermal reduction and water splitting; hence despite a fixed F_{WS}, the thermodynamic driving force for hydrogen production is increased by the mass reduction.

$$\frac{d\delta_{ox}}{dt} = \frac{F_{WS}}{n_{oxide}} \frac{\frac{2pO_2(\delta, T_{WS})^{3/2}}{p_{ref}^{1/2}} + 2pO_2(\delta, T_{WS})K_{H_2O,T_{WS}} - \chi_{H_2O}K_{H_2O,T_{WS}}(p_{tot} - pO_2(\delta, T_{WS}))}{(\frac{pO_2(\delta, T_{WS})^{1/2}}{p_{ref}^{1/2}} + K_{H_2O,T_{WS}})(p_{tot} - pO_2(\delta, T_{WS}))}$$

(9)

in which F_{WS} is the molar flow rate of the gas in the water splitting step, $pO_2(\delta,T_{WS})$ again describes the relationship between instantaneous pO_2 and δ, now at T_{WS}, $K_{H_2O,T_{WS}}$ is the equilibrium thermolysis reaction constant (again at T_{WS}), p_{tot} is the total pressure (typically 1 atm), and χ_{H_2O} is the mole fraction of water in the reactant gas stream. Gas evolution profiles for both thermal reduction and water splitting were computed here in a stepwise fashion using a time increment of 0.01 min.

Shown in Figure 5 are comparisons of the experimental gas evolution profiles that are predicted by the thermokinetic model for (a) reduction of 0.5225 g of STM55 on heating from ambient temperature to 1404 °C under a heating rate of 500 °C min⁻¹ and holding at the reduction temperature for 30 min using a reduction sweep gas of 33.5 ppm O₂ in Ar, supplied at a volumetric flow rate ($V_{TR} = F_{TR} \times$ reduction gas molar volume) of 500 mL min⁻¹, followed by (b) oxidation of this reduced material (for 60 min) at 1000 °C using an oxidation stream of pH₂O = 0.4 atm, balance Ar, supplied at a volumetric rate, V_{WS}, of 300 mL min⁻¹. The experiment was performed in a tubular flow reactor heated with an infrared heating source, integrated with an in-line mass spectrometer for off-gas analysis and an oxygen partial pressure sensor. Procedures used for determining the true experimental reduction conditions represented in the calculation, which differed slightly from the nominal conditions (1400 °C and 10 ppm O₂), are described in detail in Figure S12a,b (Supporting Information).

The agreement between the experiment and model is rather good for both oxygen release and hydrogen production, where it is to be emphasized that there are no fit parameters associated with the model. The cumulative oxygen evolution amounts are both 14.1 mL g⁻¹ and as such are in particularly good agreement. The equivalent oxygen nonstoichiometry values after the 30 min reduction period is 0.230 (experimental value) and 0.231 (model value). Extrapolation to 4 h of reduction time is predicted to increase the nonstoichiometry value to 0.239, effectively matching the eventual equilibrium value. Thus, only marginal increases in fuel production per cycle are expected with increased

reduction times. Direct comparison of the full profiles reveals that the experimental oxygen release begins to lag the predicted value once the sample reaches a temperature of ∼800 °C (Figure S12c, Supporting Information). At this temperature, the driving force for reduction becomes large (Figure 4), and the disagreement indicates an inability of the material to remain in quasi-equilibrium with the gas phase. The implication is that the overall rate becomes limited (or colimited) by material kinetic factors, likely the surface reaction step rather than solid-state diffusion. Within ∼4 min of reduction at 1404 °C, the cumulative oxygen release approximately reaches that of the model, reflective of rapid material kinetics at this high temperature. Turning to the water splitting step, the cumulative hydrogen production over the 60 min of reaction is 7.7 mL g⁻¹, as compared to the predicted value of 7.9 mL g⁻¹, where it is again emphasized that the prediction is made without any fitting parameters and only accounts for gas-phase mass transport limitations. The disagreement at the initial stages of the hydrogen production half-cycle, at which the thermodynamic driving force for the reaction is large, suggests again a process that is initially limited (or colimited) by material kinetics. Such behavior has been observed in both LSM[36] and ceria.[48] The long tail in the hydrogen production profile, in contrast, can be understood to result from the decrease in ΔG for reaction 7 as δ approaches its final equilibrium value corresponding to the temperature and gas atmosphere conditions at which water splitting is performed. This moderate driving force for the water splitting half-reaction also results in a low steam-to-hydrogen conversion (Figure S12d, Supporting Information), a common challenge for perovskite-based STCH materials operated on the basis of nonstoichiometric oxygen release and uptake.[16]

2.3.3. Steady-State Cycling. In a second set of experiments, steady-state cycling was performed with the objective of assessing material behavior under reactor-relevant conditions. Ten different sets of conditions were evaluated, Table 2, with 8−10 cycles performed for each set of conditions. Here, the thermal reduction gas was fixed at a nominal value of $pO_2 = 10^{-5}$ atm (balance Ar), the
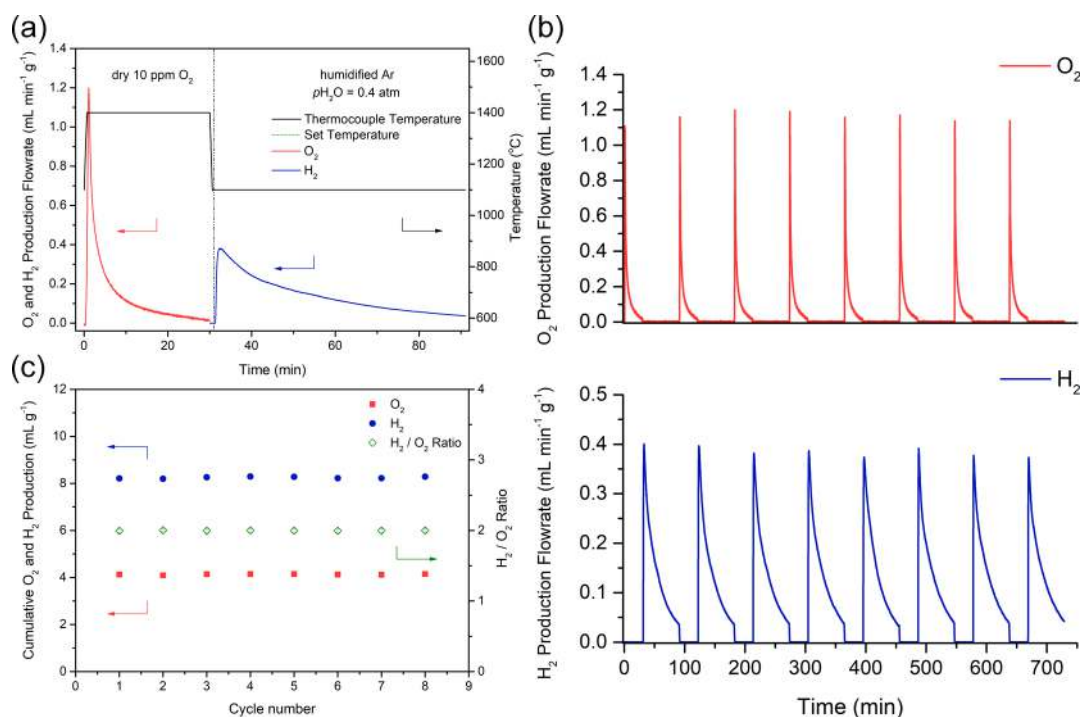
Figure 6. Representative thermochemical cycling results from STM55 using protocol M4 of Table 2 with reduction at 1400 °C and water splitting at 1100 °C with $pH_2O = 0.4$ atm: (a) typical reduction (30 min) and water splitting (60 min) as evolution profiles; (b) profiles for steady-state cycling over eight cycles; and (c) total amount of H_2 and O_2 produced in each cycle and the corresponding H_2/O_2 ratio.

reduction time was fixed at 30 min, and the flow rate of the steam-saturated Ar in the water splitting half-cycle was fixed at 300 mL min^{-1}. Parameters varied were T_{TR} (1350 or 1400 °C), T_{WS} (800–1200 °C), the water splitting time (t_{WS}, 15 or 60 min), V_{TR} (500 or 1000 mL min^{-1}), pH_2O (0.2 or 0.4 atm), and oxide mass (0.5225 or 0.2529 g). Because the deviation between set and actual reduction temperatures was found to be averaged out as a consequence of the multiple cycles, results are reported with respect to the set (nominal) temperature, without the need to correct for the true temperature.

Representative results of cyclic O_2 and H_2 production for one of these conditions are shown in Figure 6, with the remainder documented in Figures S13−S23 (Supporting Information). Three features are immediately evident from Figure 6: (1) oxygen release is much faster than hydrogen production, consistent with quasi-equilibrium behavior and the measured thermodynamic properties; (2) fuel production is highly reproducible between cycles, with no evidence of decay; and (3) the cumulative volumetric H_2/O_2 ratio is almost precisely 2:1 for all cycles, as expected for complete utilization of all oxygen vacancies generated in the thermal reduction step for hydrogen production in the water splitting step. Consistent with the stable fuel productivity over the many hours of cumulative operation, X-ray powder diffraction analysis of the material after the conclusion of the cycling experiments (Figure S24, Supporting Information), showed that the perovskite phase was retained. Furthermore, the open porosity, designed to provide easy access for gases to react with the solid phase and limit solid-state diffusion distances to no more than a few microns, was largely retained, although there is a noticeable growth in the average feature size compared to the as-prepared material, Figure 7. This coarsening is likely to have preceded the data collection. The experimental protocol of instrument validation involved exposure of the sample to high temperature (1400 °C), reducing conditions ($pO_2 = 10^{-5}$ atm) for
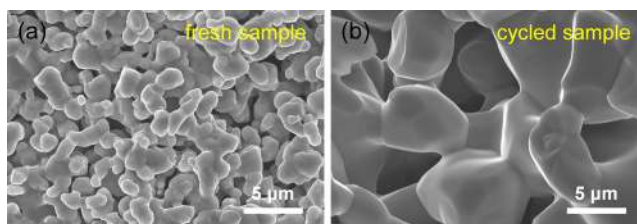

Figure 7. SEM top view of the microstructures of $SrTi_{0.5}Mn_{0.5}O_{3-\delta}$ porous monolith sample (a) before and (b) after thermochemical water splitting measurements.

an integrated period of several days prior to performing the thermochemical cycling experiments reported here. The stability of the fuel production behavior over the 8−10 cycles of each of the 10 cycling conditions shown in Figures 6 and S13−S21 is indicative of a stable morphology, particularly when the water splitting step is as low as 800 °C (Figure S13).

The results from the steady-state cycling experiments are summarized in Figure 8. Several important trends are apparent. First, with all other parameters fixed, a decrease in T_{WS} does not produce a monotonic increase in fuel production, Figure 8a, as might be naively expected based on thermodynamic considerations (see, e.g., Figure S10, Supporting Information). The behavior suggests that the reaction is limited (or colimited) by material kinetic parameters at ~1000 °C and lower, consistent with the conclusion drawn from the analysis of the thermal reduction profile in Figure 5a,b. Second, in agreement with thermodynamic expectations, the fuel production increases with an increase in pH_2O in the oxidation gas stream, as evidenced from a comparison of cycling conditions M2 and M3. Third, a decrease in the thermal reduction temperature results in a decrease in cumulative hydrogen production, as also thermodynamically expected. This third effect can be discerned from a comparison of
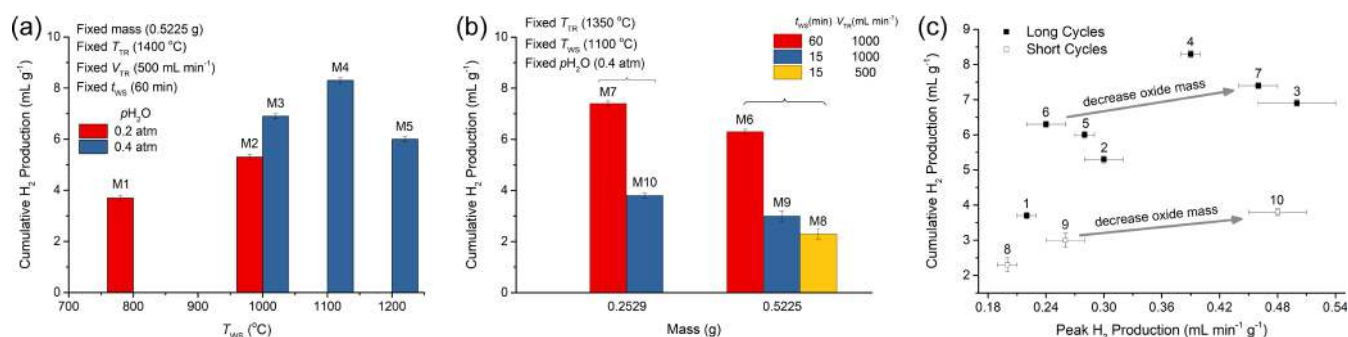
Figure 8. Experimentally measured hydrogen productivity over STM55 porous monolith for multiple-cycle thermochemical water splitting experiments for the conditions described in Table 2. (a) Impact of changing water splitting temperature and steam partial pressure; (b) impact of varying the oxide mass, reduction time, and reduction gas flow rate; and (c) summary of the cumulative hydrogen production values and peak production rates for all multicycle experiments, with the impact of changing oxide mass with all other parameters fixed highlighted.

the results from conditions M4 and M6, for which is it seen that, despite the larger gas flow rate in the thermal reduction half-cycle in M6, the fuel production is diminished by almost 25%. Fourth, as predicted from the thermokinetic model for capturing gas-phase mass transport limitations, decreasing the oxide mass increases the fuel production, Figure 8b. Here, a decrease in mass by a factor of ∼2 results in an increase in gravimetric fuel production by 21% for a 15 min water splitting half-cycle (M9 vs M10) and by 15% when the half-cycle is 60 min (M6 vs M7). Finally, decreasing the cycle time, specifically t_{WS}, with all other factors held constant, predictably decreases the fuel production per cycle. However, the decrease in per cycle hydrogen production is accompanied by a desirable increase in the time-averaged hydrogen productivity because of the high rate of hydrogen production at the initiation of the water splitting half-cycle.

The behavior of the peak hydrogen production, which occurs close to the initiation of the water splitting half-cycle, merits some discussion. This parameter appears surprisingly uncorrelated with the cumulative hydrogen production, Figure 8c. The behavior suggests that, similar to the single-cycle experiment, Figure 5c, the initial and later stages of the process may be limited by distinct factors. In particular, the initial rate, during which the thermodynamic driving force is large, is likely to be influenced by surface reaction kinetics (i.e., a colimited process), whereas the later stages in the process are likely to be limited by a diminishing thermodynamic driving force. The significant impact on the mass-normalized peak production rate by decreasing oxide mass suggests a role of thermodynamics even in the initial stages, as opposed to a process that is entirely limited by material kinetics. With material kinetic factors impacting only the very initial stages of fuel production, approximate optimization of the cycling strategy may be possible analytically under the assumption of quasi-equilibrium behavior throughout the process, without resort to extensive cycling experiments. Development of the formalism required to treat this steady-state problem is beyond the scope of the present work.

Because fuel production per cycle can be manipulated by varying seemingly unimportant cycling parameters, it is a flawed metric for evaluating material efficacy for the STCH process. Nevertheless, it is perhaps the most quoted metric, and as such, there is value in comparing the present results with state-of-the-art materials reported in the literature with respect to this parameter. As a first step toward expanding the definition of desirable characteristics within the framework of data derived from cycling experiments, we consider fuel productivity (fuel produced per unit time) as a second important metric. Shown in Figure 9 is a
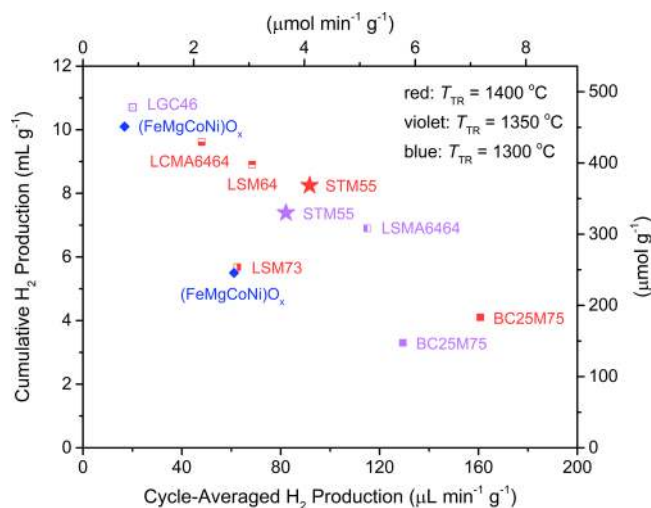

Figure 9. Selected results of thermochemical cycling studies performed on STM55 (stars, this work) under the conditions indicated, shown in comparison to literature results for other promising materials. The representation reveals the trade-off between high cumulative hydrogen production for a single cycle and high production rate as averaged over the complete cycle time. Data sources: LGC46 (=LaGa$_{0.4}$Co$_{0.6}$O$_3$), Chen et al.;[18] (FeMgCoNi)O$_x$, Zhai et al.;[51] LCMA6464 (=La$_{0.6}$Ca$_{0.4}$Mn$_{0.6}$Al$_{0.4}$O$_3$), Wang et al.;[17] LSM64 (=La$_{0.6}$Sr$_{0.4}$MnO$_3$) and LSM73 (=La$_{0.7}$Sr$_{0.3}$MnO$_3$), Yang et al.;[15] LSMA6464 (=La$_{0.6}$Sr$_{0.4}$Mn$_{0.6}$Al$_{0.4}$O$_3$), McDaniel et al.;[13] and BC25Mn75 (Ba-Ce$_{0.25}$Mn$_{0.75}$O$_3$), Barcellos et al.[19]

summary of data reported in the literature for cycles with thermal reduction temperatures of 1400 °C or lower, against the axes of fuel production and fuel productivity, where values from the literature for the latter term are computed from the reported cycle times. Even acknowledging the uncertainty associated with unknown parameters such as gas flow rates and sample mass in the literature results, the summary reveals that STM55 is among the most competitive materials reported to date for STCH production. Presentation of the performance criteria in this manner emphasizes the need to develop rigorous standards for comparing materials, while accentuating the improbability that any single material will outperform all others for all cycling strategies. Instead, it is likely that material- and architecture-specific cycling strategies that balance the trade-off between fuel per cycle and fuel per unit time will be developed for each candidate STCH material.

3. CONCLUSIONS

In sum, we demonstrate that the cubic perovskite STM55 has high capacity and stable performance for hydrogen production by the solar thermochemical approach. This material has an ideal combination of high thermal stability, large entropy of reduction, and moderate enthalpy of reduction. From the enthalpy and entropy functions, we compute the gas evolution profiles predicted by quasi-equilibrium behavior (i.e., gas-phase mass transport limitations) and find reasonable agreement with the measured profiles. Thus, under the conditions studied, the global rate of hydrogen production is largely independent of the material kinetic parameters, specifically surface reaction rate and bulk oxygen diffusivity, although the surface reaction step may colimit the process when the thermodynamic driving force is large (at the initiation of the reaction) or the water splitting temperature is low (1000 °C or lower). The potential for predicting kinetic behavior from the thermodynamic functions underscores the importance of careful measurements of the T and pO_2 dependence of the oxygen nonstoichiometry. Methods for attaining reliable and comprehensive nonstoichiometry data from TGA are presented. In particular, it is emphasized that under reducing conditions, long equilibration times may be required to complete the oxygen evolution from the sample, which typically has large mass to ensure sensitivity to small changes in relative mass. The redox chemistry of STM55 displays intriguing behavior. The enthalpy of reduction is larger than in cubic $SrMnO_3$ and cubic $CaMnO_3$, and complete reduction experiments suggest that Mn rather than Ti changes oxidation state during cycling. Thus, the presence of Ti must impact the overall strength of the Mn−O bond within the perovskite structure. The entropy of reduction of STM55 is unusually large. The limited experimental measurements of $AMnO_3$ perovskites, in which A represents alkaline earth elements, hint at the possibility that high reduction entropy may be a general feature of such materials, potentially because of a Mn^{4+}/Mn^{2+} redox couple. Finally, we propose a comparison of thermochemical materials on a basis that includes the cycle-time-averaged hydrogen production rate in addition to the hydrogen produced by any given cycle. We further note that both of these metrics can be manipulated by control of the cycling process parameters and thus complete experimental details are required in order to faithfully rank materials for hydrogen production efficacy. In this regard, reporting thermodynamic properties, which are process independent, may have a higher value than reporting fuel production rates.

4. METHODS

Complete details of the computational and experimental methods employed in this work are detailed in the Supporting Information. A brief description is provided here. The material STM55 was synthesized by a solid-state reaction of $SrCO_3$ (≥99.9% trace metal basis, Sigma-Aldrich), TiO_2 (≥99.8% trace metal basis, Sigma-Aldrich), and MnO_2 (Reagent Plus, ≥ 99%, Sigma-Aldrich). The materials were hand-milled, then formed into a disc, and held at 1250 °C for 36 h. After collecting diffraction data, these steps were repeated three times using a reaction temperature 1400 °C and reaction time of 12 h, at which point no further changes were observed in the diffraction pattern. The chemical composition of the bulk material was ascertained by ICP-OES (iCAP7000 Thermo Fisher Scientific in axial configuration) for simultaneous detection of Sr, Ti, and Mn. SEM studies were performed with a Hitachi SU8030 field emission scanning electron microscope equipped with an Oxford Aztec X-max 80 silicon drift detector for chemical analysis by EDS. X-ray powder diffraction (XRD) studies, both ex and in situ, were performed using a Rigaku Ultima IV diffractometer, with additional high-resolution, ex situ experiments performed using a

Rigaku SmartLab diffractometer offering high flux. In situ (high temperature) diffraction data were collected under air using an Ultima HTK 1200 heating chamber, with total dwell times of 22 min at each measurement temperature. Thermogravimetric data were collected using a Netzsch simultaneous thermal analyzer (STA449C) coupled with a MicroPoas Sentag oxygen sensor. Uncertainties reported in Table 1 and Figure 3 reflect the (small) uncertainties in oxygen partial pressure and mass after following manufacturer specified calibration procedures. Thermochemical hydrogen production was carried out using an in-house constructed test station[8] composed of an infrared gold imaging furnace (ULVAC RHL-E44VHT), a quadrupole mass spectrometer (Pfeiffer Thermostar GSD301T2) for off-gas detection, and a MicroPoas Sentag oxygen sensor for in situ measurement of pO_2. The uncertainty reported in Figure 5 for measured cumulative gas production reflects the uncertainties in the mass spectrometer calibration after following stringent calibration procedures using standard premixed gases. Computational prediction of vacancy formation energies was performed by DFT calculations using the projector-augmented wave method as implemented in the Vienna Ab Initio Simulation Package (VASP).[49,50]

■ ASSOCIATED CONTENT

ⓢ Supporting Information

The Supporting Information is available free of charge at https://pubs.acs.org/doi/10.1021/acs.chemmater.0c03278.

> Computational methods, sample preparation, crystallographic and morphological characterization, TGA, thermochemical water splitting, XRD pattern of as-synthesized material, SEM image and EDS chemical analysis, TGA and XRD of complete reduction experiment, thermal stability evaluation, XRD patterns post-thermal exposure, continuous heating and cooling TGA profiles, stepped heating TGA profiles, analysis methods of stepped heating TGA profiles, oxygen nonstoichiometry derived from stepped heating TGA profiles, enthalpy and entropy of reduction as functions of δ, predicted equilibrium fuel productivity for selected cycling conditions, experimental protocol for predictable hydrogen production, extended analysis of measured and predicted oxygen and hydrogen evolution profiles, cyclic thermochemical fuel production, conditions provided in Table 2, comparison of hydrogen production profiles from cyclic operation, comparison of oxygen evolution profiles from cyclic operation, and comparison of XRD patterns before and after extensive cycling (PDF)

■ AUTHOR INFORMATION

Corresponding Author

Sossina M. Haile − *Department of Materials Science and Engineering, Program of Applied Physics, and Department of Chemistry, Northwestern University, Evanston, Illinois 60208, United States;* ● orcid.org/0000-0002-5293-6252; Email: sossina.haile@northwestern.edu

Authors

Xin Qian − *Department of Materials Science and Engineering, Northwestern University, Evanston, Illinois 60208, United States;* ● orcid.org/0000-0002-6537-616X

Jiangang He − *Department of Materials Science and Engineering, Northwestern University, Evanston, Illinois 60208, United States;* ● orcid.org/0000-0001-9643-3617

Emanuela Mastronardo − *Department of Materials Science and Engineering, Northwestern University, Evanston, Illinois 60208, United States; Institute of Catalysis and Petrochemistry, Spanish National Research Council (CSIC), E-28049 Madrid, Spain*

Bianca Baldassarri — *Program of Applied Physics, Northwestern University, Evanston, Illinois 60208, United States*

Christopher Wolverton — *Department of Materials Science and Engineering and Program of Applied Physics, Northwestern University, Evanston, Illinois 60208, United States;* orcid.org/0000-0003-2248-474X

Complete contact information is available at:
https://pubs.acs.org/10.1021/acs.chemmater.0c03278

Notes

The authors declare no competing financial interest.

REFERENCES

(1) Scheffe, J. R.; Steinfeld, A. Oxygen exchange materials for solar thermochemical splitting of H_2O and CO_2: a review. *Mater. Today* **2014**, *17*, 341−348.

(2) Bulfin, B.; Vieten, J.; Agrafiotis, C.; Roeb, M.; Sattler, C. Applications and limitations of two step metal oxide thermochemical redox cycles; a review. *J. Mater. Chem. A* **2017**, *5*, 18951−18966.

(3) Lund, H. Renewable energy strategies for sustainable development. *Energy* **2007**, *32*, 912−919.

(4) Chum, H. L.; Overend, R. P. Biomass and renewable fuels. *Fuel Process. Technol.* **2001**, *71*, 187−195.

(5) Centi, G.; Perathoner, S. Towards Solar Fuels from Water and CO_2. *ChemSusChem* **2010**, *3*, 195−208.

(6) Young, K. J.; Martini, L. A.; Milot, R. L.; Snoeberger, R. C.; Batista, V. S.; Schmuttenmaer, C. A.; Crabtree, R. H.; Brudvig, G. W. Light-driven water oxidation for solar fuels. *Coord. Chem. Rev.* **2012**, *256*, 2503−2520.

(7) Chueh, W. C.; Falter, C.; Abbott, M.; Scipio, D.; Furler, P.; Haile, S. M.; Steinfeld, A. High-Flux Solar-Driven Thermochemical Dissociation of CO_2 and H_2O Using Nonstoichiometric Ceria. *Science* **2010**, *330*, 1797−1801.

(8) Chueh, W. C.; Haile, S. M. A thermochemical study of ceria: exploiting an old material for new modes of energy conversion and CO_2 mitigation. *Philos. Trans. R. Soc., A* **2010**, *368*, 3269−3294.

(9) Kubicek, M.; Bork, A. H.; Rupp, J. L. M. Perovskite oxides — a review on a versatile material class for solar-to-fuel conversion processes. *J. Mater. Chem. A* **2017**, *5*, 11983−12000.

(10) Rao, C. N. R.; Dey, S. Solar thermochemical splitting of water to generate hydrogen. *Proc. Natl. Acad. Sci. U.S.A.* **2017**, *114*, 13385.

(11) Haeussler, A.; Abanades, S.; Jouannaux, J.; Julbe, A. Non-Stoichiometric Redox Active Perovskite Materials for Solar Thermochemical Fuel Production: A Review. *Catalysts* **2018**, *8*, 611.

(12) Bayon, A.; de la Calle, A.; Ghose, K. K.; Page, A.; McNaughton, R. Experimental, computational and thermodynamic studies in perovskites metal oxides for thermochemical fuel production: A review. *Int. J. Hydrogen Energy* **2020**, *45*, 12653−12679.

(13) McDaniel, A. H.; Miller, E. C.; Arifin, D.; Ambrosini, A.; Coker, E. N.; O'Hayre, R.; Chueh, W. C.; Tong, J. Sr- and Mn-doped $LaAlO_{3-\delta}$ for solar thermochemical H_2 and CO production. *Energy Environ. Sci.* **2013**, *6*, 2424−2428.

(14) Ezbiri, M.; Takacs, M.; Theiler, D.; Michalsky, R.; Steinfeld, A. Tunable thermodynamic activity of $La_xSr_{1-x}Mn_yAl_{1-y}O_{3-\delta}$ ($0 \leq x \leq 1, 0 \leq y \leq 1$) perovskites for solar thermochemical fuel synthesis. *J. Mater. Chem. A* **2017**, *5*, 4172−4182.

(15) Yang, C.-K.; Yamazaki, Y.; Aydin, A.; Haile, S. M. Thermodynamic and kinetic assessments of strontium-doped lanthanum manganite perovskites for two-step thermochemical water splitting. *J. Mater. Chem. A* **2014**, *2*, 13612−13623.

(16) Scheffe, J. R.; Weibel, D.; Steinfeld, A. Lanthanum-Strontium-Manganese Perovskites as Redox Materials for Solar Thermochemical Splitting of H_2O and CO_2. *Energy Fuels* **2013**, *27*, 4250−4257.

(17) Wang, L.; Al-Mamun, M.; Liu, P.; Wang, Y.; Gui Yang, H.; Zhao, H. $La_{1-x}Ca_xMn_{1-y}Al_yO_3$ perovskites as efficient catalysts for two-step thermochemical water splitting in conjunction with exceptional hydrogen yields. *Chin. J. Catal.* **2017**, *38*, 1079−1086.

(18) Chen, Z.; Jiang, Q.; Cheng, F.; Tong, J.; Yang, M.; Jiang, Z.; Li, C. Sr- and Co-doped $LaGaO_{3-\delta}$ with high O_2 and H_2 yields in solar thermochemical water splitting. *J. Mater. Chem. A* **2019**, *7*, 6099−6112.

(19) Barcellos, D. R.; Sanders, M. D.; Tong, J.; McDaniel, A. H.; O'Hayre, R. P. $BaCe_{0.25}Mn_{0.75}O_{3-\delta}$—a promising perovskite-type oxide for solar thermochemical hydrogen production. *Energy Environ. Sci.* **2018**, *11*, 3256−3265.

(20) Hao, Y.; Yang, C.-K.; Haile, S. M. Ceria−Zirconia Solid Solutions ($Ce_{1-x}Zr_xO_{2-\delta}$, $x \leq 0.2$) for Solar Thermochemical Water Splitting: A Thermodynamic Study. *Chem. Mater.* **2014**, *26*, 6073−6082.

(21) Meredig, B.; Wolverton, C. First-principles thermodynamic framework for the evaluation of thermochemical H_2O- or CO_2-splitting materials. *Phys. Rev. B* **2009**, *80*, 245119.

(22) Bakken, E.; Norby, T.; Stølen, S. Redox energetics of perovskite-related oxides. *J. Mater. Chem.* **2002**, *12*, 317−323.

(23) Deml, A. M.; Stevanović, V.; Holder, A. M.; Sanders, M.; O'Hayre, R.; Musgrave, C. B. Tunable Oxygen Vacancy Formation Energetics in the Complex Perovskite Oxide $Sr_xLa_{1-x}MnyAl_{1-y}O_3$. *Chem. Mater.* **2014**, *26*, 6595−6602.

(24) Vieten, J.; Bulfin, B.; Huck, P.; Horton, M.; Guban, D.; Zhu, L.; Lu, Y.; Persson, K. A.; Roeb, M.; Sattler, C. Materials design of perovskite solid solutions for thermochemical applications. *Energy Environ. Sci.* **2019**, *12*, 1369−1384.

(25) Emery, A. A.; Saal, J. E.; Kirklin, S.; Hegde, V. I.; Wolverton, C. High-Throughput Computational Screening of Perovskites for Thermochemical Water Splitting Applications. *Chem. Mater.* **2016**, *28*, 5621−5634.

(26) Naghavi, S. S.; Emery, A. A.; Hansen, H. A.; Zhou, F.; Ozolins, V.; Wolverton, C. Giant onsite electronic entropy enhances the performance of ceria for water splitting. *Nat. Commun.* **2017**, *8*, 285.

(27) Bulfin, B.; Vieten, J.; Starr, D. E.; Azarpira, A.; Zachäus, C.; Hävecker, M.; Skorupska, K.; Schmücker, M.; Roeb, M.; Sattler, C. Redox chemistry of $CaMnO_3$ and $Ca_{0.8}Sr_{0.2}MnO_3$ oxygen storage perovskites. *J. Mater. Chem. A* **2017**, *5*, 7912−7919.

(28) Mastronardo, E.; Qian, X.; Coronado, J. M.; Haile, S. M. The favourable thermodynamic properties of Fe-doped $CaMnO_3$ for thermochemical heat storage. *J. Mater. Chem. A* **2020**, *8*, 8503−8517.

(29) Jiang, S. P. Development of lanthanum strontium manganite perovskite cathode materials of solid oxide fuel cells: a review. *J. Mater. Sci.* **2008**, *43*, 6799−6833.

(30) Ramirez, A. P. Colossal magnetoresistance. *J. Phys.: Condens. Matter* **1997**, *9*, 8171−8199.

(31) Stoerzinger, K. A.; Risch, M.; Han, B.; Shao-Horn, Y. Recent Insights into Manganese Oxides in Catalyzing Oxygen Reduction Kinetics. *ACS Catal.* **2015**, *5*, 6021−6031.

(32) Wolverton, C. *Transformative Materials for High- Efficiency Thermochemical Production of Solar Fuels*, 2019.

(33) Bhalla, A. S.; Guo, R.; Roy, R. The perovskite structure—a review of its role in ceramic science and technology. *Mater. Res. Innovations* **2000**, *4*, 3−26.

(34) Sharma, S.; Singh, K.; Rawat, R.; Lalla, N. P. Structural and magnetic properties of chemically disordered perovskite $SrTi_{0.5}Mn_{0.5}O_3$. *J. Alloys Compd.* **2017**, *693*, 188−193.

(35) Rørmark, L.; Morch, A. B.; Wiik, K.; Stolen, S.; Grande, T. Enthalpies of oxidation of $CaMnO_{3-\delta}$, $Ca_2MnO_{4-\delta}$ and $SrMnO_{3-\delta}$ - Deduced redox properties. *Chem. Mater.* **2001**, *13*, 4005−4013.

(36) Ignatowich, M. J.; Bork, A. H.; Davenport, T. C.; Rupp, J. L. M.; Yang, C.-k.; Yamazaki, Y.; Haile, S. M. Impact of enhanced oxide reducibility on rates of solar-driven thermochemical fuel production. *MRS Commun.* **2017**, *7*, 873−878.

(37) Akhtar, M. J.; Akhtar, Z.-U. -N.; Jackson, R. A.; Catlow, C. R. A. Computer Simulation Studies of Strontium Titanate. *J. Am. Ceram. Soc.* **1995**, *78*, 421−428.

(38) Negas, T.; Roth, R. S. The system $SrMnO_{3-x}$. *J. Solid State Chem.* **1970**, *1*, 409−418.

(39) Bednorz, J. G.; Scheel, H. J. Flame-fusion growth of $SrTiO_3$. *J. Cryst. Growth* **1977**, *41*, 5−12.

(40) Vasala, S.; Karppinen, M. $A_2B'B''O_6$ perovskites: A review. *Prog. Solid State Chem.* **2015**, *43*, 1−36.

(41) Panlener, R. J.; Blumenthal, R. N.; Garnier, J. E. A thermodynamic study of nonstoichiometric cerium dioxide. *J. Phys. Chem. Solids* **1975**, *36*, 1213−1222.

(42) Ezbiri, M.; Becattini, V.; Hoes, M.; Michalsky, R.; Steinfeld, A. High Redox Capacity of Al-Doped $La_{1-x}Sr_xMnO_3$- Perovskites for Splitting CO_2 and H_2O at Mn-Enriched Surfaces. *Chemsuschem* **2017**, *10*, 1517−1525.

(43) Mizusaki, J.; Mima, Y.; Yamauchi, S.; Fueki, K.; Tagawa, H. Nonstoichiometry of the perovskite-type oxides $La_{1-x}Sr_xCoO_{3-\delta}$. *J. Solid State Chem.* **1989**, *80*, 102−111.

(44) Mizusaki, J.; Yamauchi, S.; Fueki, K.; Ishikawa, A. Non-stoichiometry of the perovskite-type oxide $La_{1-x}Sr_xCrO_{3-\delta}$. *Solid State Ionics* **1984**, *12*, 119−124.

(45) Mizusaki, J.; Yoshihiro, M.; Yamauchi, S.; Fueki, K. Non-stoichiometry and defect structure of the perovskite-type oxides $La_{1-x}Sr_xFeO_{3-\delta}$. *J. Solid State Chem.* **1985**, *58*, 257−266.

(46) Davenport, T. C.; Yang, C.-K.; Kucharczyk, C. J.; Ignatowich, M. J.; Haile, S. M. Maximizing fuel production rates in isothermal solar thermochemical fuel production. *Appl. Energy* **2016**, *183*, 1098−1111.

(47) Davenport, T. C.; Yang, C.-K.; Kucharczyk, C. J.; Ignatowich, M. J.; Haile, S. M. Implications of Exceptional Material Kinetics on Thermochemical Fuel Production Rates. *Energy Technol.* **2016**, *4*, 764−770.

(48) Davenport, T. C.; Kemei, M.; Ignatowich, M. J.; Haile, S. M. Interplay of material thermodynamics and surface reaction rate on the kinetics of thermochemical hydrogen production. *Int. J. Hydrogen Energy* **2017**, *42*, 16932−16945.

(49) Kresse, G.; Furthmüller, J. Efficient iterative schemes for ab initio total-energy calculations using a plane-wave basis set. *Phys. Rev. B: Condens. Matter Mater. Phys.* **1996**, *54*, 11169−11186.

(50) Kresse, G.; Furthmüller, J. Efficiency of ab-initio total energy calculations for metals and semiconductors using a plane-wave basis set. *Comput. Mater. Sci.* **1996**, *6*, 15−50.

(51) Zhai, S.; Rojas, J.; Ahlborg, N.; Lim, K.; Toney, M. F.; Jin, H.; Chueh, W. C.; Majumdar, A. The use of poly-cation oxides to lower the temperature of two-step thermochemical water splitting. *Energy Environ. Sci.* **2018**, *11*, 2172−2178.

Supporting Information

Favorable Redox Thermodynamics of SrTi$_{0.5}$Mn$_{0.5}$O$_{3-\delta}$ in Solar Thermochemical Water Splitting

Xin Qian,[†] Jiangang He,[†] Emanuela Mastronardo,[†,§] Bianca Baldassarri,[‡] Christopher Wolverton,[†,‡] Sossina M. Haile*[,†,‡,⊥]

[†]Department of Materials Science and Engineering, Northwestern University, Evanston, IL 60208, United States

[‡]Program of Applied Physics, Northwestern University, Evanston, IL 60208, United States

[⊥]Department of Chemistry, Northwestern University, Evanston, IL 60208, United States

[§]Institute of Catalysis and Petrochemistry, Spanish National Research Council (CSIC), C/ Marie Curie, 2. E-28049. Madrid, Spain

*Corresponding Author: sossina.haile@northwestern.edu

This File Includes:

Section A: Methods

Section B: Supplemental Figures and Tables

Section A: Methods

1. Computational Methods

All density functional theory (DFT) calculations are performed using the projector augmented wave (PAW) method,[1, 2] as implemented in the Vienna Ab initio Simulation Package (VASP).[3, 4] The Perdew-Burke-Ernzerhof (PBE) exchange-correlation functional,[5] a plane wave basis set with a cutoff energy of 520 eV, and Γ-centered k-mesh with more than 8000 KPPRA (k-point per reciprocal atom) for sampling the Brillouin zone were used for bulk and supercell calculations. The oxygen vacancy formation energy is calculated by removing one oxygen atom from a supercell of the bulk crystal, shown on the left side of below figure is the crystal structure of the bulk cubic (Fm-3m) Sr_2TiMnO_6 (rock-salt ordered $SrTi_{0.5}Mn_{0.5}O_3$) and shown on the right side is the $2\times2\times2$ supercell with one oxygen vacancy. The Hubbard U correction within the Dudarev framework[6] is applied to the $3d$ electrons of Mn with U = 2 eV. The reference energy of oxygen is corrected using the method in literature.[7, 8]
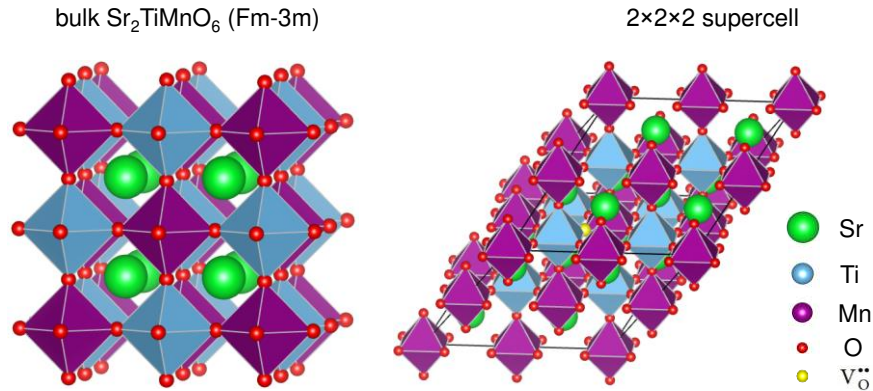
left: crystal structure of the bulk cubic (Fm-3m) Sr_2TiMnO_6 (rock-salt ordered $SrTi_{0.5}Mn_{0.5}O_3$)

right: the $2\times2\times2$ supercell ($8\times$ the primitive rhombohedral cell) with one oxygen vacancy

2. Sample Preparation

The perovskite $SrTi_{0.5}Mn_{0.5}O_{3-\delta}$ (STM55) was synthesized by solid state reaction. All solvents and chemicals were of reagent quality and used without further purification. Stoichiometric quantities

of SrCO$_3$ ($\geq$ 99.9% trace metal basis, Sigma-Aldrich), TiO$_2$ ($\geq$ 99.8% trace metal basis, Sigma-Aldrich) and MnO$_2$ (Reagent Plus, $\geq$ 99%, Sigma-Aldrich) were mixed with isopropanol (ACS reagent, $\geq$ 99.5%, Sigma-Aldrich) and ground with an agate mortar and pestle for a total of 60 min. The resulting paste-like mixture was dried to yield a powder, which was then formed into a disc and pressed under 20 MPa of uniaxial pressure (1 min). The green body was placed on an alumina sintering boat covered with a layer of Pt foil (99.99%, Strem Chemicals, Inc.) and was sintered at 1250 °C for 36 h under still air. The Pt foil was used to prevent reaction between STM55 and alumina sintering boat. After cooling to room temperature, the sintered disc was crushed, ground, and re-formed into a disc for additional sintering at 1400 °C in 12 h increments, with these steps repeated until no further changes in the diffraction pattern were observed (for a total of 36 h at 1400 °C under still air). The result was a single-phase perovskite as determined by X-ray powder diffraction, hereafter STM55. The STM55 powder resulting from this sequence of steps was used for all subsequent experiments.

For thermogravimetric analyses, ~1.388 g of powder was ground and mixed with isopropanol, then lightly pressed into porous monolith and sintered at 1400 °C for 2 h under still air. The resulting cylindrical porous monolith with a dimension of 8 mm (diameter) × 10 mm (height) was used for oxygen non-stoichiometry measurements under a set of temperature and oxygen partial pressure conditions. Similarly, a small sample (8 mm (diameter) × 3 mm (height)) with ~0.4 g mass was prepared for measurement of reference state oxygen non-stoichiometry via a complete reduction experiment. For thermochemical cycling experiments, two sintered cylindrical porous monoliths with ~0.52 g and ~0.25 g in mass were prepared in the same way, and the dimensions are 6 mm (diameter) × 7 mm (height) and 6 mm (diameter) × 3 mm (height), respectively. The porosity was ~51 % in all porous monoliths, as determined by measurement of sample mass and dimensions.

3. Sample Characterizations

The crystal structure of STM55 bulk powder (including (i) as-synthesized, (ii) after exposure to

extreme conditions for evaluation of thermal stability, and (iii) after all thermochemical water splitting measurements) was characterized by ex situ X-ray diffraction (XRD, Ultima IV, Rigaku) using Cu Kα (λ = 0.1541 nm) radiation (40 kV, 44 mA) in the scanning range (2θ) of either 10 − 120° or 20 − 80° with a step size of 0.05° and a scanning speed of 5° min⁻¹. XRD was also performed on the as-synthesized STM55 bulk powder using a high flux diffractometer (SmartLab, Rigaku) under Cu Kα (λ = 0.1541 nm) radiation in the scanning range (2θ) of 16 − 28° at a scanning speed of 5° min⁻¹, for detection of the existence of any superstructure peaks in order to distinguish ordered versus disordered structure. In addition, high-temperature in situ XRD (Ultima HTK 1200 Heating Chamber, Rigaku, mounted on the Ultima IV, Rigaku diffractometer using Cu Kα (λ = 0.1541 nm) radiation (40 kV, 44 mA)) was carried out upon heating at temperatures between 600 °C and 1400 °C in increments of 100 °C and heating rate of 10 °C min⁻¹ between measurement temperatures. Diffraction data were collected in the scanning range (2θ) of 20 − 80° (step size = 0.05° and scan rate = 5° min⁻¹). Once heated to the set temperature the sample was held at this temperature for equilibration of 10 min, then diffraction data were collected over a 12 min period, for a total hold time of 22 min at each temperature.

For phase composition analysis of the residual products after reduction of STM55 bulk powder under 3% H_2 for measurement of reference state oxygen content, diffraction data were collected in the scanning range (2θ) of 10 − 90° and all the other diffraction parameters were the same as described in ex situ measurement. The phase formation and evolution were analyzed by the whole pattern fitting (WPF) function implemented in the commercial software JADE by Materials Data, Inc (MDI). Crystallographic parameters were analyzed by Rietveld refinement using the GSAS-II Crystallography Data Analysis Software.[9]

The surface morphologies of the sintered porous monolith sample before and after thermochemical hydrogen production measurements were characterized with a Field Emission Scanning Electron Microscopy (FESEM, Hitachi SU8030). The elements of the synthesized material were confirmed

by the Energy Dispersive X-ray Spectroscopy (EDS, Oxford AZtec X-max 80 SDD) with an acceleration voltage of 20 kV. Chemical composition of bulk material was analyzed by Inductively Coupled Plasma – Optical Emission Spectrometry (ICP-OES, iCAP7000 ThermoFisher Scientific in axial configuration) for simultaneous detection of Sr, Ti and Mn. The bulk powder with mass in ~5 mg was dissolved by digestion in a solution of 5% aqua regia. The solution was held for 48 h at room temperature and then heated in a water bath at 65 °C for 30 min.

4. Thermogravimetric Analysis

4.1 Thermal Stability Evaluation of Bulk Material

In addition to high-temperature in situ XRD under air, thermal stability of STM55 bulk material was characterized by ex situ XRD collected on samples after exposure to extreme temperature (T) and low oxygen partial pressure (pO_2) conditions (Table S1). Under air, STM55 bulk powder was put in a Pt crucible and was exposed to 1500 °C or 1600 °C for 1 h in a tube furnace, then was crushed and ground for XRD measurements. For all other low pO_2 conditions (up to T = 1500 °C, and pO_2 as low as 3.00×10^{-5} atm), heat treatment of STM55 bulk powder was performed in a thermogravimetric analyzer (TGA, STA449C, Netzsch) and a low pO_2 atmosphere was created by mixing Ar with oxygen-poor gas, e.g., 10% O_2 or 10 ppm O_2 in Ar (certified by Air Liquide). The gas flow rate was controlled by four digital mass flow controllers (MFCs). The reported pO_2 values are those detected using an in situ pO_2 sensor (MicroPoas, Setnag) connected to the TGA exhaust, and held in a sealed quartz tube, in turn placed in a furnace held at a temperature of 700 °C. The thermal treatment protocols are specified in Table S1, along with the results of X-ray powder diffraction analysis of the product retrieved from the heat treatment.

4.2 Reference State Oxygen Non-stoichiometry and Cation Chemical Composition

A reference state (T = 1000 °C, pO_2 = 0.075 atm) was established for the measurement of absolute oxygen non-stoichiometry (δ) under desired T, pO_2 conditions. The absolutely oxygen content in the reference state was determined using a complete reduction procedure. Specifically, a sintered

porous monolith sample with 399.47 mg in mass was heated to reference temperature at a ramp rate of 5 °C min^{-1} and equilibrated for 1 h in the reference condition, the system was purged with Ar for 5 min, and then the sample was exposed to 3% H_2 (balance Ar) for additional 5 h followed by cooling under the same gas atmosphere. The residual material after reduction reaction under 3% H_2 (balance Ar) was crushed and ground for XRD measurement.

4.3 Continuous vs. Stepped Measurements

Based on the evidence of thermal stability of STM55, thermogravimetric analysis of the material was carried out over the temperature range of 300 – 1500 °C on a porous, self-supporting monolith sample with an as-prepared mass of 1.388 g. Significantly, STM55 was found to react with alumina above about 1200 °C, and hence all TGA studies were performed using an alumina plate covered by Pt foil. Thermodynamic profiles were collected under a constant ramp rate of 5 °C min^{-1} under reference gas (pO_2 = 0.075 atm) and 2 °C min^{-1} under ten desired experimental pO_2 conditions (Table 1), the total gas flow rate through the TGA chamber was controlled at 250 mL min^{-1}. The pO_2 profile along the entire thermogravimetric measurement was recorded by an in-situ oxygen sensor. Depending on pO_2, two different methods, either continuous heating or stepped heating, were employed in the measurement of mass loss under desired experimental pO_2.

Continuous Heating – Under relatively oxidizing pO_2 (0.208, 0.150, 0.075, 0.028, 0.0087 atm), a continuous heating protocol was utilized. Specifically, the sample was first ramped to the reference condition (T = 1000 °C, pO_2 = 0.075 atm) at a ramp rate of 5 °C min^{-1} and was held for an additional 1 h period. The measurement gas of interest was then introduced and the sample raised to a new equilibration temperature of 1500 °C at a ramp rate of 2 °C min^{-1}. The mass-temperature profile was measured upon cooling from 1500 °C to 300 °C at a rate of 2 °C min^{-1}. Following a 1 h hold at 300 °C, the sample was again heated to 1500 °C at the same rate of 2 °C min^{-1} and was held for 1 h, yielding a second mass-temperature profile. At the end of the measurement, the reference gas was introduced and the sample was returned to the reference condition to establish the reversibility

of the mass loss at a ramp rate of 5 °C min^{-1}. By tracking the oxygen partial pressure and by comparing the mass-temperature profiles under heating and cooling, it is possible to assess whether the mass has equilibrated under each experimental pO_2 condition, hence, continuous $\delta(T)$ profiles under five oxidizing pO_2 conditions can be obtained. It is also straightforward to check whether any material degradations (e.g., phase change, volatilization) have occurred after high temperature measurement by comparing the mass in the two reference states.

Stepped Heating – Thermogravimetric measurements under more reducing pO_2 (0.0046, 8.19 × 10^{-4}, 2.14 × 10^{-4}, 9.79 × 10^{-5}, 3.00 × 10^{-5} atm) were carried out using a stepped heating protocol instead, for the purpose to extract thermodynamic properties to a higher δ. Specifically, the sample was first held at the reference condition (T = 1000 °C, pO_2 = 0.075 atm) for a 1 h period. The measurement gas of interest was then introduced and a step-wise heating profile was employed, using temperature increments of 100 °C, a heating rate of 2 °C min^{-1} between steps, and long hold times (1 – 4 h) at each measurement temperature for equilibration of mass. At the end of the measurement, the sample was returned to the reference condition to establish the reversibility of the mass loss. The pO_2 profiles in the course of the TGA measurement were measured in situ using an integrated oxygen sensor. By tracking the pO_2-time and the mass-time profiles under each isothermal hold step, it is possible to extrapolate the equilibrium oxygen non-stoichiometry at each condition. The resulting discrete $\delta(T, pO_2)$ points under more reducing conditions can be obtained, together with continuous $\delta(T)$ profiles under oxidizing conditions, it is possible to extract the redox thermodynamic properties to a pretty large δ.

4.4 Uncertainty Analysis

By always returning to the initial condition it is established that there is no drift in the system or volatilization of any of the cations. The recovered mass is within the uncertainty of the instrument. Error bars in Figure 3(a) to indicate these mass uncertainties. In the case of the extrapolated values, the uncertainties are computed from the extrapolation functions (Figure S8). The uncertainty

cannot be fully quantified because no independent method of determining whether an extrapolation is legitimate was applied. The uncertainty is more realistically estimated at 0.004 in δ based on the disagreement between the non-stoichiometry determined directly from the TGA measurement and from the thermodynamic fitting functions (Figure 3(a)). The temperature in the TGA is calibrated using standard procedures. The uncertainty is less than 0.5 °C. For example, the melting point of Au is measured to be 1063.8 °C, compared to the reference value of 1064 °C. The uncertainty in temperature is far smaller than the size of the data points in Figure 3(a). The calibration of the oxygen sensors, used for both TGA and thermochemical cycling is performed using standard premixed gases. For a typical measurement when the input is synthetic air, the measured oxygen partial pressure is 0.2094 atm. Similarly, when the input is 0.1% O_2 (as designated by the supplier), the measured oxygen partial pressure is 0.0010 atm. The uncertainties in pO_2 for each TGA measurement condition are provided in Table 1. The uncertainties in mass and oxygen partial pressure of the TGA measurements translate into the uncertainties in the van't Hoff plot, as shown in Figure 3(b). These generally correspond to the size of the data points. Due to the inability to accurately measure δ at large non-stoichiometry and the increase in noise in the thermodynamic functions at high δ (Figure S9) the uncertainty in the thermodynamic prediction of δ under the experimental reduction conditions is estimated at 0.004 (Figure 5(a,c)).

5. Thermochemical Water splitting

The gas production from water splitting was measured in an in-house constructed thermochemical cycling station comprising an infrared gold imaging furnace (ULVAC RHL-E44VHT) capable of rapid heating and cooling of materials, a manifold of MFCs for control the flow rate of inlet gases, a quadrupole mass spectrometer (Pfeiffer Thermostar GSD301T2) for off-gas detection and a high-temperature oxygen sensor for in situ measurement of pO_2. The reactor for the cycling experiment was composed of one outer quartz tube with a diameter of 1/2" and one inner alumina tube with a diameter of 1/4". A sintered porous monolith sample of specified mass was placed within the hot zone of the furnace. The sample diameter was fixed to match that of the inner diameter of alumina

tube to ensure that most gases were passing through the sample. The furnace temperature was controlled by an alumina-sheathed S-type thermocouple whose tip was in contact with the upstream end of the sample. An additional thermocouple alumina shield was placed in contact with the downstream end of the sample in order to prevent sample from moving under high flow rate of reduction and oxidation gases. To ensure blackbody heating of the sample and thermocouples, the inside of the alumina tube was lined with Pt foil (99.9% purity, 0.025 mm thick, Alfa Aesar) along 3 cm of the tube centered on the sample. Calibration of the gases supplied through these MFCs was carried out on a primary standard air flow calibrator (Gilian Gilibrator-2, Sensidyne), and was referenced to 25 °C and 1 atm before execution of cycling experiments to ensure desired gas flow rate.

Prior to gas production measurements, the reduction gas was flowed for 30 min for establishment of the steady-state baseline of oxygen (O_2) and hydrogen (H_2) ion current in the mass spectrometer, followed by repeated cycling experiments. Upon cooling down, the gas lines were purged by Ar gas for 5 min, the calibration of O_2 and H_2 were performed consecutively with an additional purge by Ar in between the two calibrations. For example, during the reduction half-cycle, 10 ppm O_2 in Ar gas was supplied at a flow rate of 500 mL min^{-1}. The oxygen partial pressure recorded by the pO_2 sensor was used for the prediction of O_2 release in Figure 5. Oxidation was carried out using an atmosphere of either 20% H_2O or 40% H_2O in Ar, achieved by passing 300 mL min^{-1} Ar through a bubbler inside a temperature-controlled oven at either 60 °C or 76 °C prior to its delivery to the furnace. All the gas lines in which steam flowed through were wrapped with heating ropes and covered with alumina foil, the temperature of heated lines was controlled at ~150 °C to prevent steam from condensation. In the oxidation half-cycle, excessive O_2 and H_2 were generated by steam thermolysis within the furnace (distinct from hydrogen production by reaction with the oxide material), and they were eliminated by flowing the exhaust gas through a hollow, porous cylinder of Rh-decorated ceria passing through the alumina shield placed at the downstream end of the furnace at which the temperature was around 800 °C. The exhaust gas after the reactor was passed

through a glass condenser held at 4 °C achieved by a ThermoCube 300 Thermoelectric Chiller (Hyland Scientific) and the steam in the gas was condensed. The remaining gases were partially delivered to mass spectrometer and were sampled every 1.8 s. The produced O_2 or H_2 concentration in the gas stream was determined from the recorded ion current using an eight-point calibration curve with known compositions of O_2 or H_2, achieved by mixing 'pure' Ar gas with either 10% O_2 in Ar or 3% H_2 in Ar. The majority of the downstream gas was passed to the oxygen sensor held in a sealed quartz tube at 700 °C, its calibration under air was completed before each set of cycling experiments in order to obtain accurate real-time oxygen partial pressure. An uncertainty of ~ 2% in the evolved gas mass flow measurements is estimated based on the accuracy of the calibration procedures and the tendency of the calibration to drift over a relatively short period of time.

In this study, two categories of thermochemical water splitting experiments were performed. The first set of experiments aimed for establishing the level of agreement of the gas evolution profiles with the thermo-kinetic model (results shown in Figure 5) were carried out using the temperature and gas profile displayed in Figure S11. Specifically, the material was annealed under flowing synthetic air at 1000 °C and cooled down to ambient condition to establish a fully oxidized state of the oxide in the initiation of thermal reduction, the oxide was then ramped to 1400 °C (nominal) at a ramp rate of 500 °C min^{-1} under 500 mL min^{-1} 10 ppm O_2 (balance Ar) and was reduced for a total of 30 min, followed by quenching (500 °C min^{-1}) to the water splitting temperature of 1000 °C and was re-oxidized by humidified Ar (300 mL min^{-1} flow rate) with $pH_2O = 0.4$ atm for 60 min. The oxygen and hydrogen production profiles were compared with the predicted profiles using a thermo-kinetic model for assessment of the gas evolution behavior. The second set of experiments comprised a set of selected cycling conditions that were repeated for 8 – 15 cycles to identify the optimal water splitting conditions and to evaluate the hydrogen production stability (details shown in Table 2).

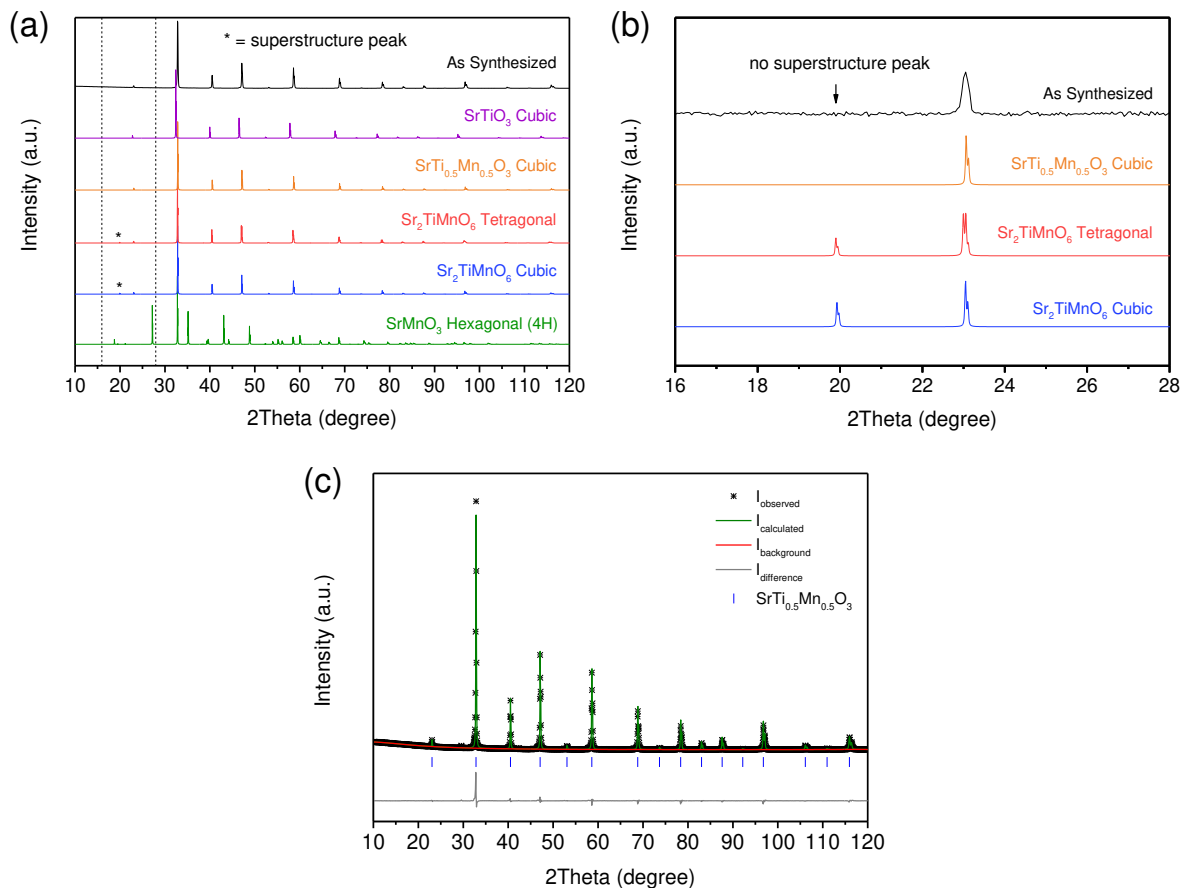# Section B: Supplemental Figures and Tables

Figure S1. The measured X-ray powder diffraction patterns of synthesized STM55 powder, data are collected using: (a) Ultima IV; (b) high flux SmartLab diffractometer. Theoretical diffraction patterns of the endmembers 4H-hexagonal $SrMnO_3$ ($P6_3/mmc$)[10] and cubic $SrTiO_3$ (Pm-3m)[11], as well as the cubic B-site disordered perovskite $SrTi_{0.5}Mn_{0.5}O_3$ (Pm-3m)[12], and the B-site ordered double perovskites Sr_2TiMnO_6 (cubic, Fm-3m[13] and tetragonal, I4/m[14]) are simulated in the VESTAT[15] software by using Crystallographic Information Files (CIF) from Inorganic Crystal Structure Database (ICSD) and Springer Materials online databases; (c) The GSAS refinement against the XRD pattern collected on the synthesized STM55 bulk material on the Ultima IV, for the B-site disordered perovskite with refined lattice parameter a = 3.8548(1) Å.
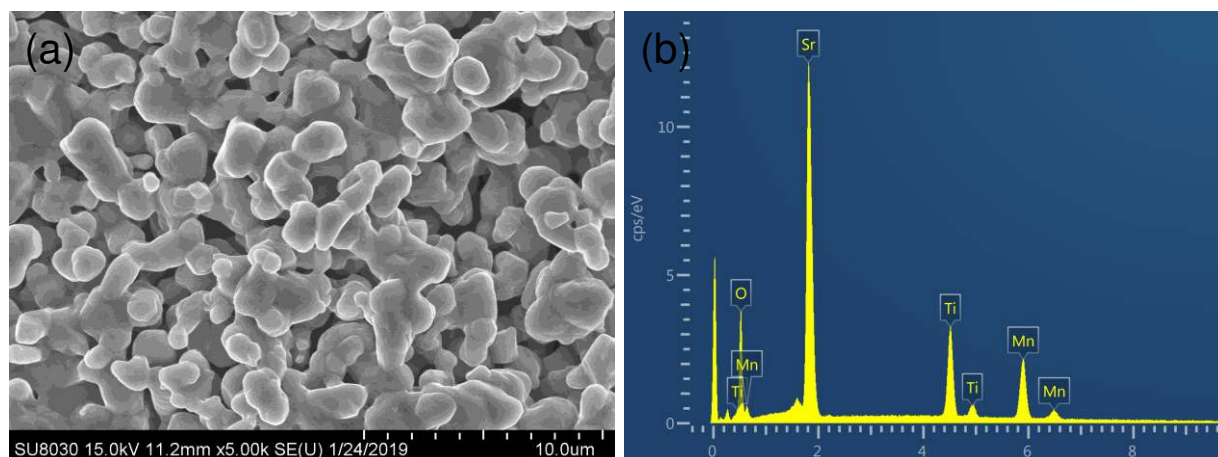
Figure S2. (a) Scanning electron microscopy top-view of the surface morphologies of lightly pressed porous monolith using synthesized STM55 powder and annealed at 1400 °C for 2 h under air; (b) EDS spectrum collected on the porous monolith, from which the elements of Sr, Ti and Mn are confirmed.

The surface morphologies of the sintered porous monoliths and the EDS spectrum are shown in Figure S2. The particle size of the porous structure lies in the range of 1 – 2 μm and the porosity is ~51%. The porous structure provides high surface area, short solid-state diffusion lengths, and enables direct flow of the gas through the entire structure, which creates more reaction sites on the surface and enhance ion diffusion in the bulk material. From the EDS spectrum, the synthesized material is confirmed to be composed of metal elements of Sr, Ti and Mn without any impurities.
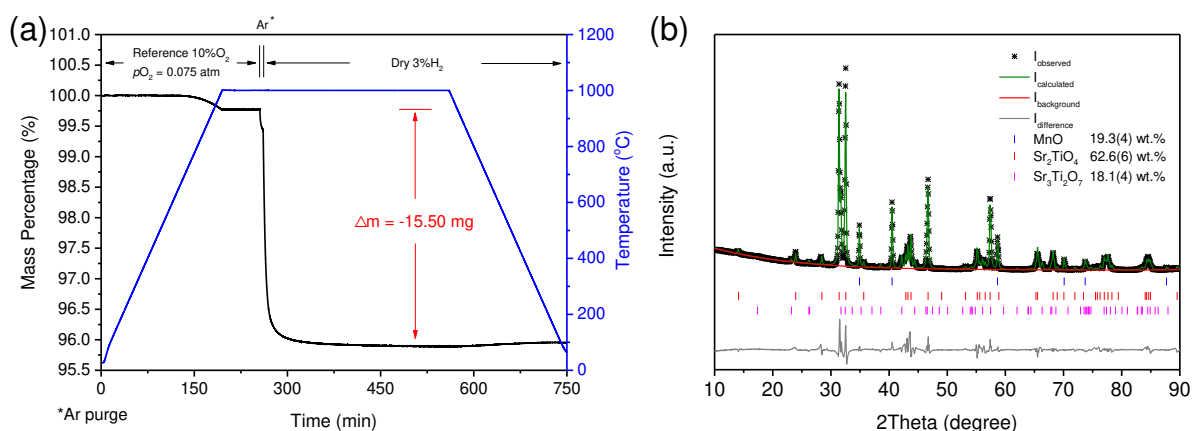
Figure S3. Behavior of STM55 upon complete reduction by 3% H_2 (balance Ar) at 1000 °C: (a) mass and temperature profiles recorded by TGA, $m_0 = 399.47$ mg; (b) XRD Rietveld refinement analysis of the reduction product and the refined weight fraction of each phase is displayed.

Because thermogravimetric analysis (TGA) yields the relative change of mass of a sample, it is necessary to determine the absolute oxygen content at some (convenient) reference state, where the mass measurement under the reference state conditions is included as part of each suite of TGA experiments. Here, a reference state of 1000 °C and $pO_2 = 0.075$ atm was selected. A sintered porous pellet sample, 399.47 mg in mass, was heated to the reference temperature at a ramp rate of 5 °C min^{-1} and equilibrated for 1 h in reference condition. After purging the system with Ar for 5 min, and the sample was exposed to 3% H_2 (balance Ar) for 5 h to induce reduction. In the final step, the sample was cooled in the same hydrogen gas and then collected for diffraction analysis.

The mass loss from this reference condition to complete reduction after exposure to 3% H_2 was 15.50 mg, Figure S3(a), and the total mass loss is 16.41 mg. Ex situ X-ray diffraction analysis of the product mixture revealed the presence of the stoichiometric phases of MnO, Sr_2TiO_4 and $Sr_3Ti_2O_7$. Thus, the Mn was completely reduced to the 2+ oxidation state. The appearance of a small amount of $Sr_3Ti_2O_7$, along with the majority reduction product Sr_2TiO_4 implies a slight excess of Ti in the synthesized material relative to Mn and Sr. The wight fractions of MnO, Sr_2TiO_4

and $Sr_3Ti_2O_7$ in the reduction product were analyzed by Rietveld refinement analysis of the diffraction pattern, Figure S3(b), and were determined to be 19.3(4), 62.6(6) and 18.1(4) wt.%, respectively. These values imply a Sr:Ti:Mn molar ratio of 1:0.551:0.486, which is in agreement with the ICP-OES chemical analysis result of 1:0.539:0.490. Ignoring the nature of the perovskite crystal structure, the reduction reaction from complete oxidation (Mn^{4+}) to complete reduction (Mn^{2+}) upon exposure to 3% H_2 is given by

$$SrO + xTiO_2 + yMnO_2 + yH_2 \rightarrow SrO + xTiO_2 + yMnO + yH_2O \tag{S1}$$
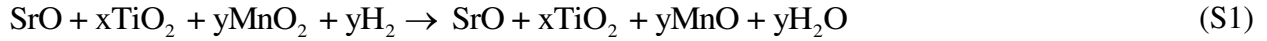
From the later studies, it is apparent that the initial mass (at 400 °C, under 0.075 atm pO_2) corresponds to the fully oxidized state. Thus, the total mass loss (16.41 mg) corresponds to the moles of oxygen lost (0.001026 moles), which in turn, corresponds to the moles of Mn in the material. The mass of MnO in the product is thus 72.77 mg, implying that the MnO mass fraction is 18.22%. This value is consistent with the 18.1(4) wt. % determined by Rietveld refinement.

Recognizing that A-site vacancies are the most common cation defect type in perovskites,[16] we write the perovskite stoichiometry normalized relative to the total B-site cation content (B-site fully occupied). Using the average of ICP and Rietveld refinement results and retaining only two significant digits, this is Sr:Ti:Mn = 0.97:0.53:0.47 (with an uncertainty of ~3% in each elemental stoichiometry). The complete reduction reaction (from the fully oxidized state) is explicitly

$$Sr_{0.97}Ti_{0.53}Mn_{0.47}O_{2.97} + 0.47H_2 \rightarrow 0.35Sr_2TiO_4 + 0.09Sr_3Ti_2O_7 + 0.47MnO + 0.47H_2O \tag{S2}$$
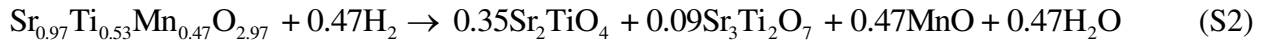
The reduction from the reference state is

$$\begin{aligned} Sr_{0.97}Ti_{0.53}Mn_{0.47}O_{2.97-\delta_{ref}} &+ (0.47\text{-}\delta_{ref})H_2 \\ &\rightarrow 0.35Sr_2TiO_4 + 0.09Sr_3Ti_2O_7 + 0.47MnO + (0.47\text{-}\delta_{ref})H_2O \end{aligned} \tag{S3}$$
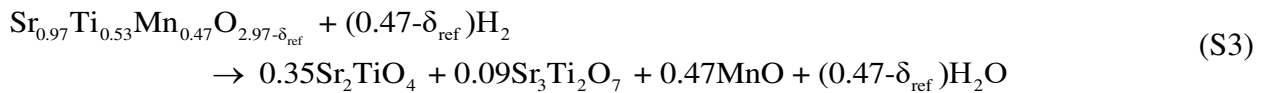
in which δ_{ref} is the oxygen non-stoichiometry at the reference condition. Based on the TGA results, δ_{ref} is found to be 0.026. The oxygen non-stoichiometry is reported relative to the deduced material stoichiometry of $Sr_{0.97}Ti_{0.53}Mn_{0.47}O_{2.97}$, which differs only slightly from the target composition in the fully oxidized state of $SrTi_{0.5}Mn_{0.5}O_3$. For notational ease, the acronym STM55 is used to describe the material despite the slight cation off-stoichiometry. The oxygen content is variable,

as discussed throughout the main manuscript, and thus is not indicated in the sample naming scheme.

Table S1. Exposure conditions to evaluate thermal stability, followed by ex situ XRD. For all but the exposure to air, the heat treatment was performed in the TGA in which the mass could also be monitored. The heating and cooling rates were 2 °C min^{-1}. The maximum temperatures possible in furnace and TGA employed are 1600 and 1500 °C, respectively. In all cases, the annealed product was a single, solid-solution perovskite, demonstrating exceptional stability of the material to extreme conditions, refined lattice constants of the annealed products were analyzed by Rietveld refinements of these XRD patterns.

Heating and Anneal pO_2 (atm)	Temperatures (°C)	Hold Time (h)	Cooling pO_2 (atm)	Ex Situ XRD	Refined Lattice Constant (Å)
Air (0.21)	1500 (furnace)	1	Air (0.21)	Cubic	a = 3.8533(4)
Air (0.21)	1600 (furnace)	1	Air (0.21)	Cubic	a = 3.8535(2)
4.35×10^{-3}	1200 (TGA)	2	4.35×10^{-3}	Cubic	a = 3.8536(3)
4.35×10^{-3}	1400 (TGA)	2	4.35×10^{-3}	Cubic	a = 3.8533(5)
4.35×10^{-3}	1500 (TGA)	2	4.35×10^{-3}	Cubic	a = 3.8532(4)
4.00×10^{-5}	1500 (TGA)	2	4.00×10^{-5}	Cubic (expanded)	a = 3.8830(2)
3.00×10^{-5}	1500 (TGA)	2	3.00×10^{-5}	Cubic (expanded)	a = 3.8825(1)
3.00×10^{-5}	1500 (TGA)	2	0.075	Cubic	a = 3.8532(3)
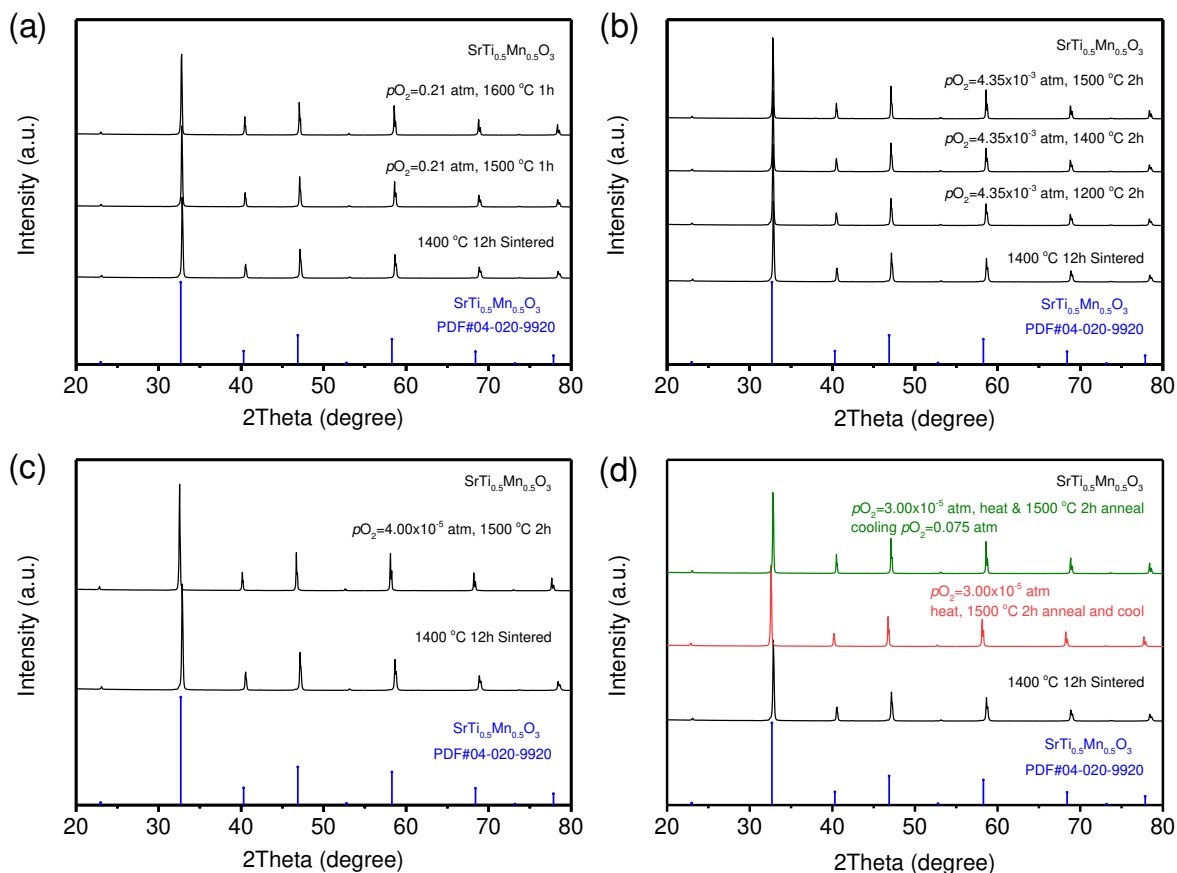
Figure S4. X-ray powder diffraction patterns collected ex situ, after exposure of the samples to the temperatures and time indicated: (a) under $pO_2 = 0.21$ atm ; (b) under $pO_2 = 4.35 \times 10^{-3}$ atm; (c) under $pO_2 = 4.00 \times 10^{-5}$ atm; and (d) under $pO_2 = 3.00 \times 10^{-5}$ atm with cooling in either $pO_2 = 3.00 \times 10^{-5}$ atm or $pO_2 = 0.075$ atm. The material STM55 is stable under all conditions examined, including up to at least 1600 °C under $pO_2 = 0.21$ atm and up to at least 1500 °C under $pO_2 = 3.00 \times 10^{-5}$ atm.

Ex situ XRD characterization of STM55 exposed to the conditions summarized in Table S1 revealed that the cooled product was in all cases a single-phase, solid-solution perovskite, Figure S4. Thus, STM55 remains in the perovskite phase up to at least 1600 °C under air ($pO_2 = 0.21$ atm) and up to at least 1500 °C under $pO_2 = 3.00 \times 10^{-5}$ atm. This high thermal phase stability is

extremely beneficial for STCH cycling, and also indicates that the thermodynamic measurements reflect the properties of the perovskite phase.

We note that upon cooling (2 °C min^{-1}) from a reduced condition under a gas atmosphere of pO_2 = 4.00 × 10^{-5} or 3.00 × 10^{-5} atm, the mass loss was not recovered (TGA profile not shown), although the thermodynamic equilibrium state for these atmospheres and ambient temperature is the fully oxidized state, see Figure 3(a). The expansion of the lattice for these two experiments reflects the retention of a non-zero oxygen non-stoichiometry. The slow rate of re-oxidation during cooling, presumably because of gas phase limitations with insufficient oxygen being supplied at the low gas flow rate of the experiment, as well as material kinetic limitations at low temperature, suggest that one may not need to use extremely high cooling rates (e.g., 500 °C min^{-1} used here) to avoid re-oxidation prior to introduction of steam for hydrogen production in real solar reactors.
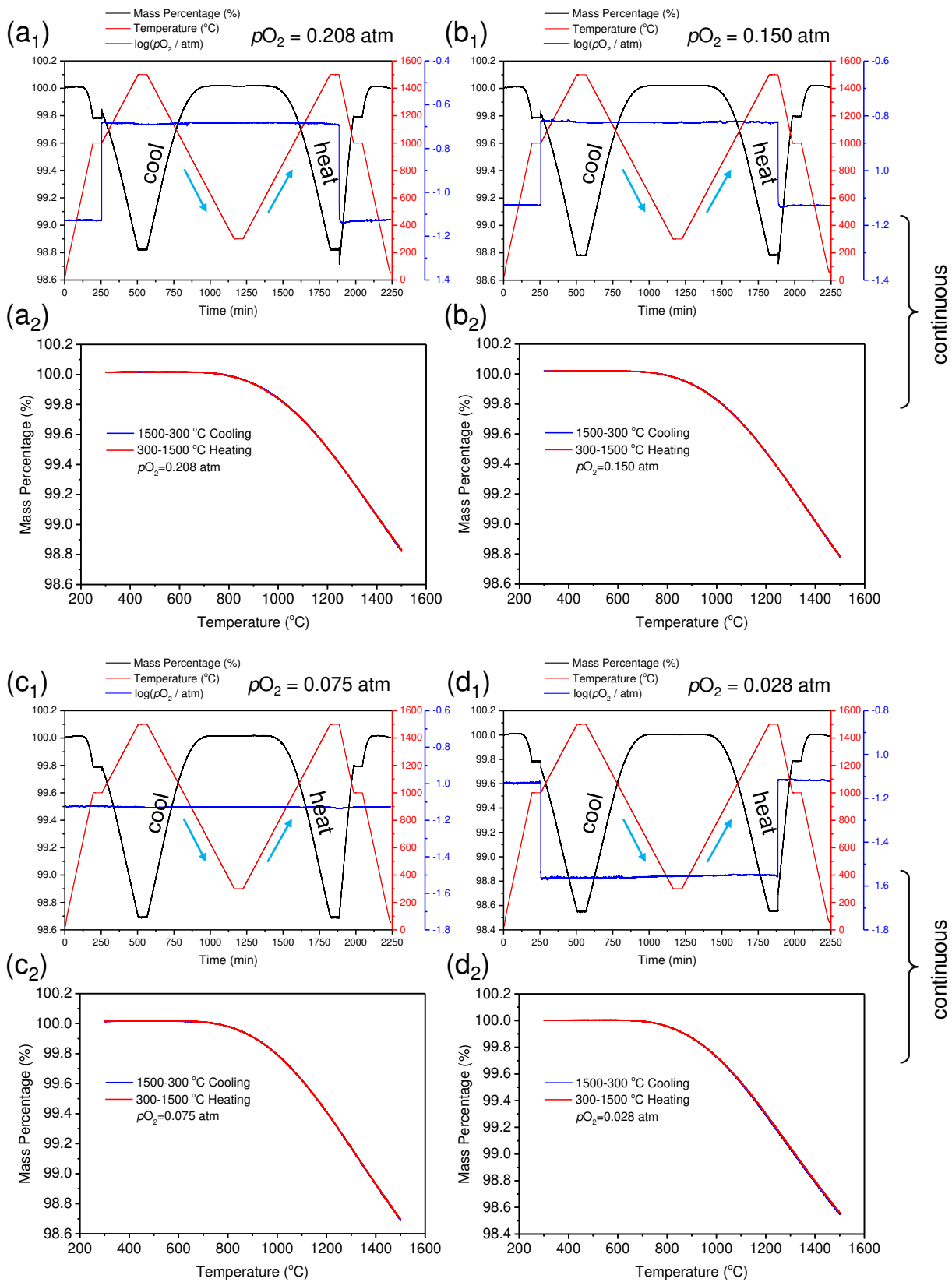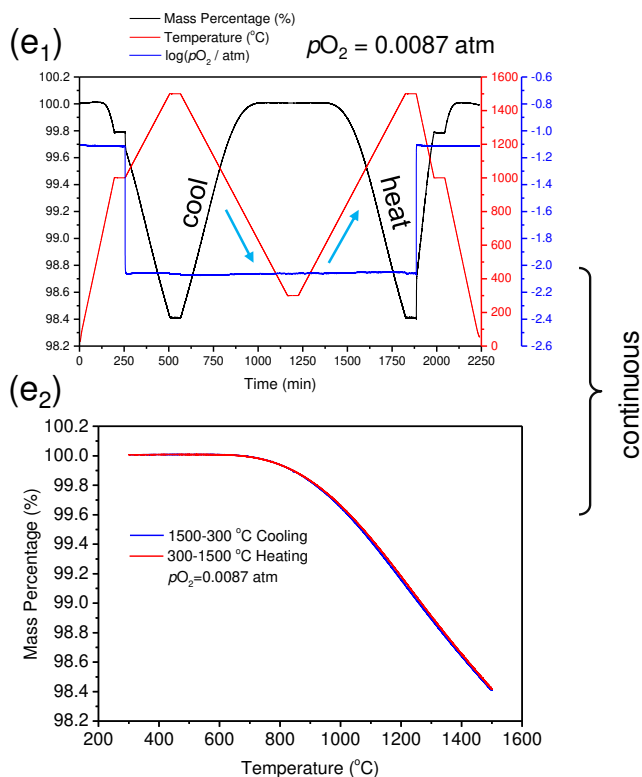
Figure S5. Mass, temperature and pO_2 profiles of STM55 under relatively oxidizing atmospheres using continuous heating protocol: (a$_1$), (a$_2$) pO_2 = 0.208 atm, m_0 = 1388.64 mg; (b$_1$), (b$_2$) pO_2 = 0.150 atm, m_0 = 1388.54 mg; (c$_1$), (c$_2$) pO_2 = 0.075 atm, m_0 = 1388.48 mg; (d$_1$), (d$_2$) pO_2 = 0.028 atm, m_0 = 1388.17 mg; (e$_1$) (e$_2$) pO_2 = 0.0087 atm, m_0 = 1388.02 mg.

After determination of the reference state (T = 1000 °C, pO_2 = 0.075 atm) oxygen content from the measurement shown in Figure S3, the absolute oxygen content of STM55 under ten different pO_2 conditions were carried out on a porous, self-supporting monolith sample with an as-prepared mass of 1.388 g under temperature range and pO_2 conditions indicated in Table 1 in either continuous or stepped heating protocol. Thermogravimetric profiles were collected under a constant heating rate of 2 °C min^{-1}, a continuous heating protocol was employed for mass loss measurement over the temperature range of 300 – 1500 °C under relatively oxidizing pO_2 conditions (0.208, 0.150, 0.075, 0.028, 0.0087 atm), Figure S5. In all of the five measurements, the mass is confirmed to be in true equilibrium with the gas phase at each condition from the

observations that the pO_2 remains constant without any fluctuations under experimental gas of interest and the mass-temperature profiles under heating and cooling match very well, and the excellent mass reversibility in the two reference states before and after mass measurement further reflect the exceptional thermal stability of STM55 under extreme conditions. Representative results, reflecting the most oxidizing ($pO_2 = 0.208$ atm) and the most reducing ($pO_2 = 0.0087$ atm) conditions examined using the continuous heating protocol, are shown in Figure S5(a_1, a_2) and S5(e_1, e_2). In both cases, the pO_2 detected at the oxygen sensor remains fixed over the course of the heating and cooling cycles, indicating that the gas flow rate is sufficiently high to maintain a fixed thermodynamic state, a condition that can be challenging to meet when the pO_2 is low and the change in oxygen content of the material, for a given change in temperature, is large. Consistent with the absence of perturbations in the detected oxygen partial pressure, the mass-temperature profiles in heating and cooling for both cases are essentially identical, Figure S5(a_2) and S5(e_2), and we can readily conclude thermodynamic behavior has been measured. In addition, the raw profiles in Figure S5(a_1) and S5(e_1), further show sharp changes in mass when the delivered pO_2 is changed, suggesting that the material kinetics are also favorable. Thermogravimetric measurements under the other three moderate pO_2 conditions (0.150, 0.075, 0.028 atm) are shown in Figure S5(b_1, b_2), S5(c_1, c_2), and S5(d_1, d_2), respectively, equilibrium of mass is also confirmed in each condition. Significantly, the pO_2 does not remain fixed and the heating and cooling profiles mismatch when the measurement is performed under an even lower pO_2 condition (< 0.0087 atm) at ramp rate of 2 °C min^{-1} (data not shown) indicating a condition that is too challenging for the material to maintain a fixed thermodynamic state.
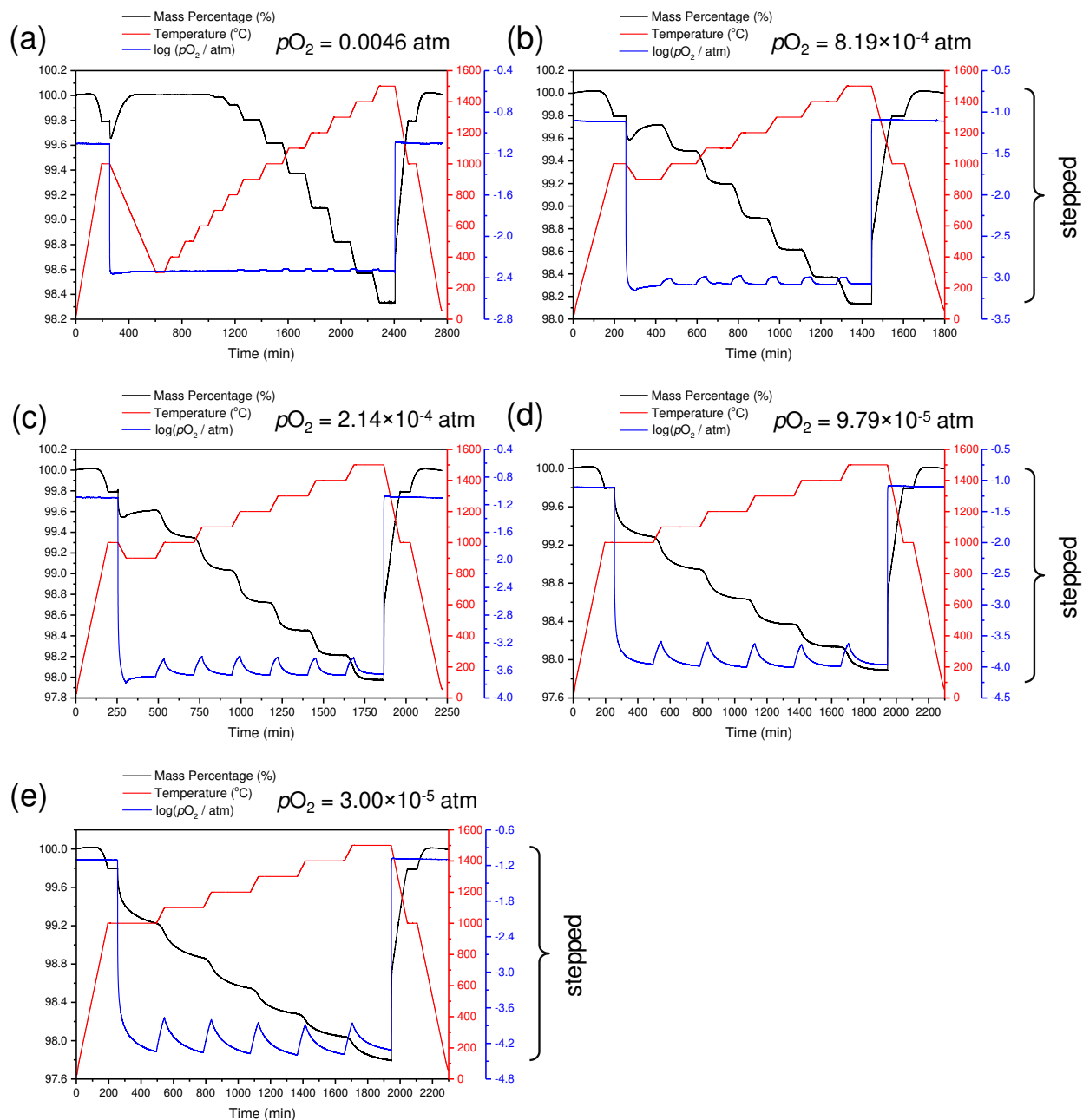
Figure S6. Mass, temperature and pO_2 profiles of STM55 under relatively reducing atmospheres using stepped heating protocol: (a) $pO_2 = 0.0046$ atm, $m_0 = 1387.94$ mg; (b) $pO_2 = 8.19 \times 10^{-4}$ atm, $m_0 = 1387.90$ mg; (c) $pO_2 = 2.14 \times 10^{-4}$ atm, $m_0 = 1387.89$ mg; (d) $pO_2 = 9.79 \times 10^{-5}$ atm, $m_0 = 1387.68$ mg. (d) $pO_2 = 3.00 \times 10^{-5}$ atm, $m_0 = 1387.82$ mg.

Since oxygen release is significant under more reducing conditions, equilibration of the sample mass is slow. To avoid possible non-equilibrium effects, instead, a stepped heating protocol was utilized for thermogravimetric measurements under more reducing pO_2 conditions (0.0046, 8.19×10^{-4}, 2.14×10^{-4}, 9.79×10^{-5}, 3.00×10^{-5} atm) with a focus on the high temperature range of 900 – 1500 °C, for the purpose to extract thermodynamic properties to a much higher δ. Mass loss profile under gas of interest was collected only in the heating process using temperature increments of 100 °C and a heating rate of 2 °C min^{-1} between steps, specifically, upon reaching a specific temperature, the sample was isothermally held for several hours (up to 4 h, depending on pO_2) for the equilibration of mass, the corresponding pO_2 profile in the entire isothermal hold was recorded by an oxygen sensor. By tracking the simultaneous relaxation of the pO_2-time and the mass-time profiles under each isothermal hold step, it offers a new pathway to extrapolate the equilibrium δ at each condition. Representative results from these measurements, reflecting the most oxidizing ($pO_2 = 0.0046$ atm) and most reducing ($pO_2 = 3.00 \times 10^{-5}$ atm) conditions examined, are shown in Figure S6(a) and S6(e), respectively. In both cases, the pO_2 detected at the sensor is not a fixed value over the course of the heating, especially at high temperatures (≥ 1000 °C). Under these reducing pO_2 conditions, the oxygen release from the sample is large relative to the oxygen concentration in the gas and significant time is required for the oxygen released by the sample to be swept out of the system. The situation is more severe at even lower pO_2, at which the oxygen content in the gas is low, and at high temperature, at which the oxygen release for a given temperature change is higher than at low temperature. In Figure S6(a), the mass underwent a small relaxation in the first ~5 min in the isothermal hold period at each high temperature (≥ 1000 °C) and quickly equilibrated afterwards, correspondingly, the recorded pO_2 underwent a slight increase during the ramp of temperature and then a small relaxation to the inlet gas oxygen partial pressure (pO_2^{inlet}) in the isothermal hold period. While, in Figure S6(e), the lowest pO_2 examined here, the mass did not equilibrate at any high temperature steps even after 4 h isothermal hold, the recorded pO_2 underwent a sharp increase during the ramp and then a large relaxation process to lower the pO_2 around the sample, reflecting the increased difficulty for the oxygen released by the sample to

be swept out of the system, the pO_2 was not able to relax to the pO_2^{inlet} level at the end of the isothermal hold. Thermogravimetric profiles under the other three reducing pO_2 conditions (8.19 × 10^-4, 2.14 × 10^-4, 9.79 × 10^-5 atm) are shown in Figure S6(b), S6(d) and S6(e), respectively, similar relaxation behavior of mass and pO_2 are also observed.
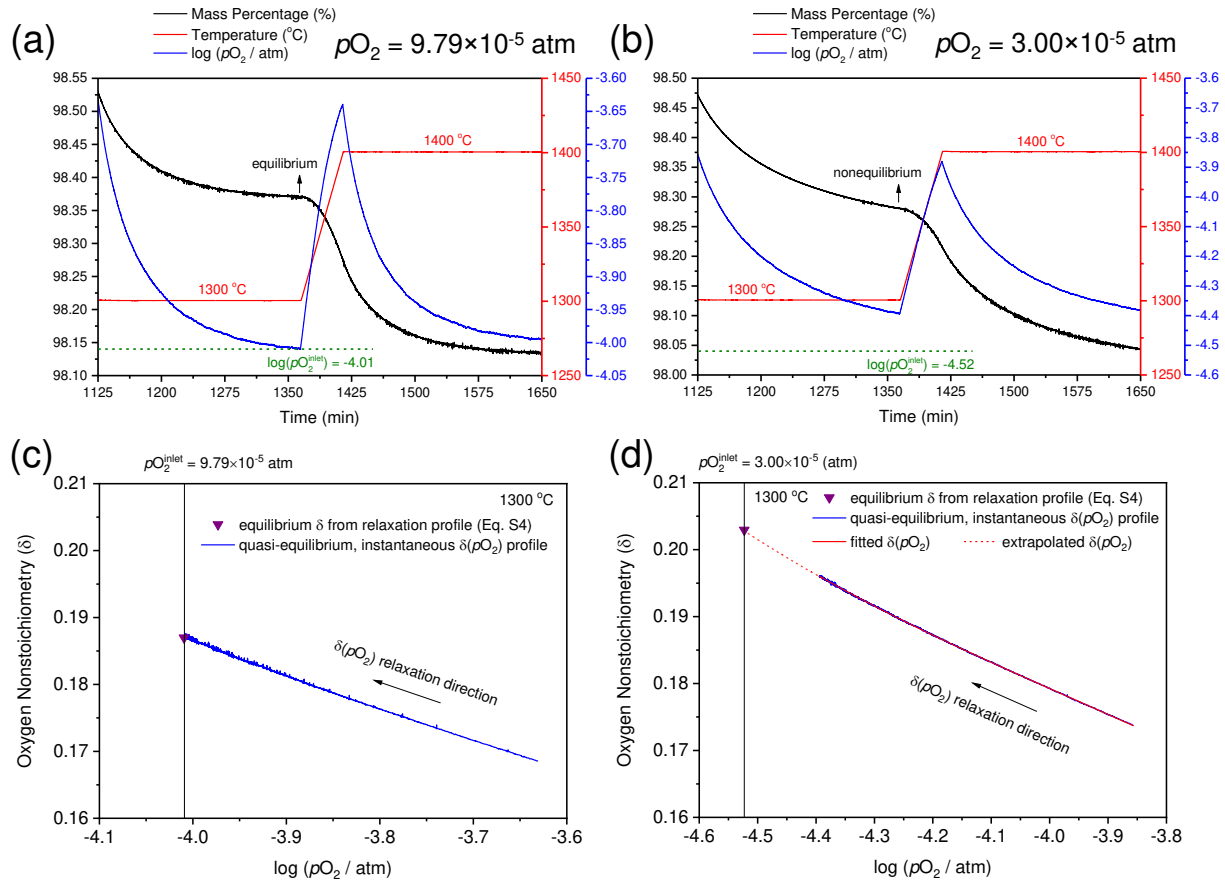
Figure S7. Mass, temperature and oxygen partial pressure profiles between 1300 °C and 1400 °C in the stepped thermogravimetric measurements of STM55 under (a) $pO_2 = 9.79 \times 10^{-5}$ atm, $m_0 = 1387.68$ mg; (b) $pO_2 = 3.00 \times 10^{-5}$ atm, $m_0 = 1387.82$ mg. (c) and (d) shows the predicted equilibrium δ from mass relaxation profile and the instantaneous $\delta(pO_2)$ profile in the isothermal period of 1300 °C in (a) and (b), respectively.

Under relatively oxidizing pO_2 conditions (0.0046, 8.19×10^{-4}, 2.14×10^{-4} atm) the system was observed to have reached equilibrium at the end of each isothermal hold such that the pO_2 detected at the exhaust matched the inlet pO_2. In contrast, under more reducing conditions under more reducing pO_2 conditions (9.79×10^{-5}, 3.00×10^{-5} atm) the isothermal hold was, in most cases, not long enough for the system to reach an equilibrium state. Here, two methods, which yielded identical results, were explored for determining the equilibrium δ at each T and pO_2 condition for

both classes of experiments. In the first method, reported in our previous work[17], the equilibrated mass in each step is obtained for the T-pO_2 pairs of the isothermal holds by assuming an exponential decay of mass towards the final value, which is given by

$$\Delta m_{step}(t) = \Delta m_{0,step} + A\exp(-\frac{t}{t_0}) \tag{S4}$$

where $\Delta m_{0,step}$ refers to the final equilibrium mass loss and $\Delta m_{step}(t)$ refers to the instantaneous mass loss at arbitrary time t in that isothermal step, and t_0 refers to the characteristic time required to relax towards equilibrium. In the second method, the exhaust pO_2 is measured and the pO_2-time and the mass-time profiles under each isothermal hold step used to generate a parametric plot of $\delta(pO_2)$. A third order polynomial is then fit to the measured data and used to compute $\delta(pO_2^{inlet})$. In principle, this yields δ for all of the pO_2 values encountered during the relaxation, but likely because of the time lag between mass detection and pO_2 detection, the data did not adequately provide these intermediate values.

Two examples are shown in Figure S7 to illustrate the analysis process. The mass, temperature and pO_2 profiles for the heating step from 1300 °C to 1400 °C and the isothermal hold at 1400 °C under pO_2^{inlet} of 9.79 × 10^{-5} and 3.00 × 10^{-5} atm are displayed in Figure S7(a) and S7(b), respectively. In both cases, the pO_2 increases during the ramp from 1300 to 1400 °C, reaches a maximal value once the temperature stops ramping, and then undergoes a relaxation towards pO_2^{inlet}. In parallel, the mass drops during the ramping period, then drops more gently during the isothermal hold as it relaxes towards the equilibrium value. In Figure S7(a), it is apparent that under T = 1300 °C, pO_2^{inlet} = 9.79 × 10^{-5} atm the recorded pO_2 reaches pO_2^{inlet} after 4 h of relaxation. Not surprisingly, as shown in Figure S7(c), the equilibrium δ calculated using Eq. S4 (single dot) under this condition corresponds to the value directly measured in the quasi-equilibrium profile. This reflects the fact that the oxygen released by the sample is completely swept out of the system by the end of the isothermal hold for these conditions. In Figure S7(b),

under the more reducing condition of $pO_2^{inlet} = 3.00 \times 10^{-5}$ atm, the recorded pO_2 does not reach

pO_2^{inlet}, indicating that more time would be required for the oxygen released from the sample to

be swept out of the system. Furthermore, the mass does not reach a plateau value. Under these

conditions, as shown in Figure S7(d), the equilibrium δ predicted from the extrapolated relaxation

profile (single dot) and from the extrapolated third order polynomial fit to the quasi-equilibrium

$\delta(pO_2)$ profile (dotted line) are in agreement.
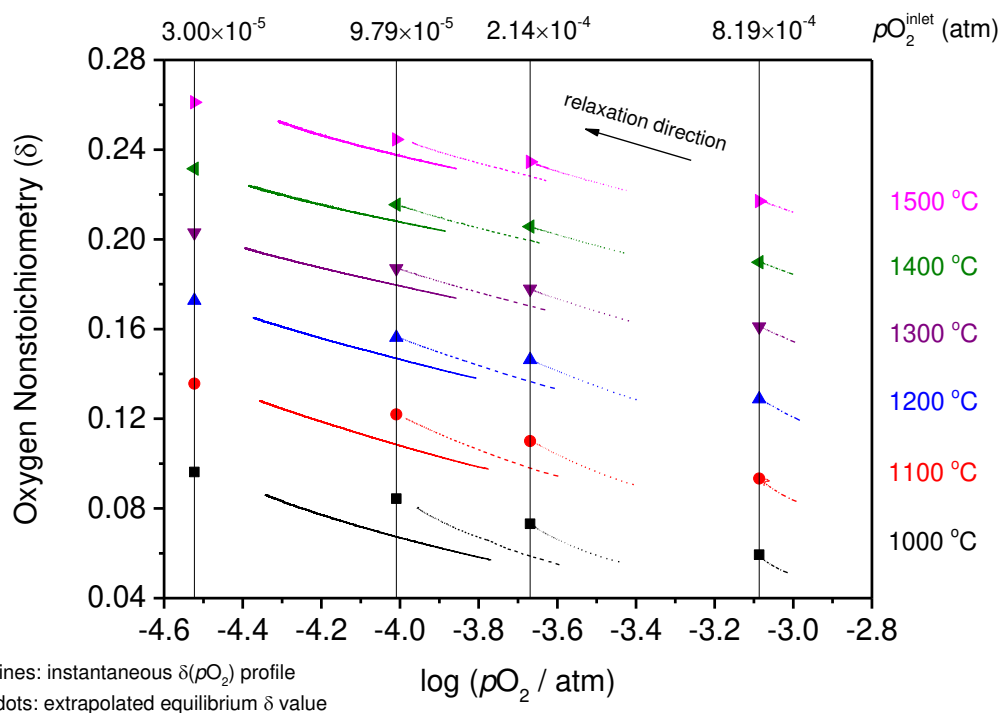
Figure S8. The instantaneous oxygen non-stoichiometry as a function of the logarithm of oxygen partial pressure at each temperature step (lines) under reducing pO_2 conditions and the extrapolated equilibrium δ values (dots) by tracking of the instantaneous δ(pO_2) profiles. These vertical solid black lines are the logarithm values of inlet gas oxygen partial pressures.

The extrapolated equilibrium δ (dots) together with the corresponding δ(pO_2) profiles (lines) at all measured temperature steps under pO_2 conditions (8.19×10^{-4}, 2.14×10^{-4}, 9.79×10^{-5}, 3.00×10^{-5} atm) are displayed in Figure S8. The extrapolated values were obtained by fitting the quasi-equilibrium curves to third order polynomial functions. In most cases, the pO_2 relaxes to that of the inlet value by the completion of the isothermal hold, providing further confidence in the data analysis. After a negligible baseline shift correction caused by gas switching, these discrete δ(T, pO_2) points and continuous δ(T) curves are summarized in Figure 3(a).
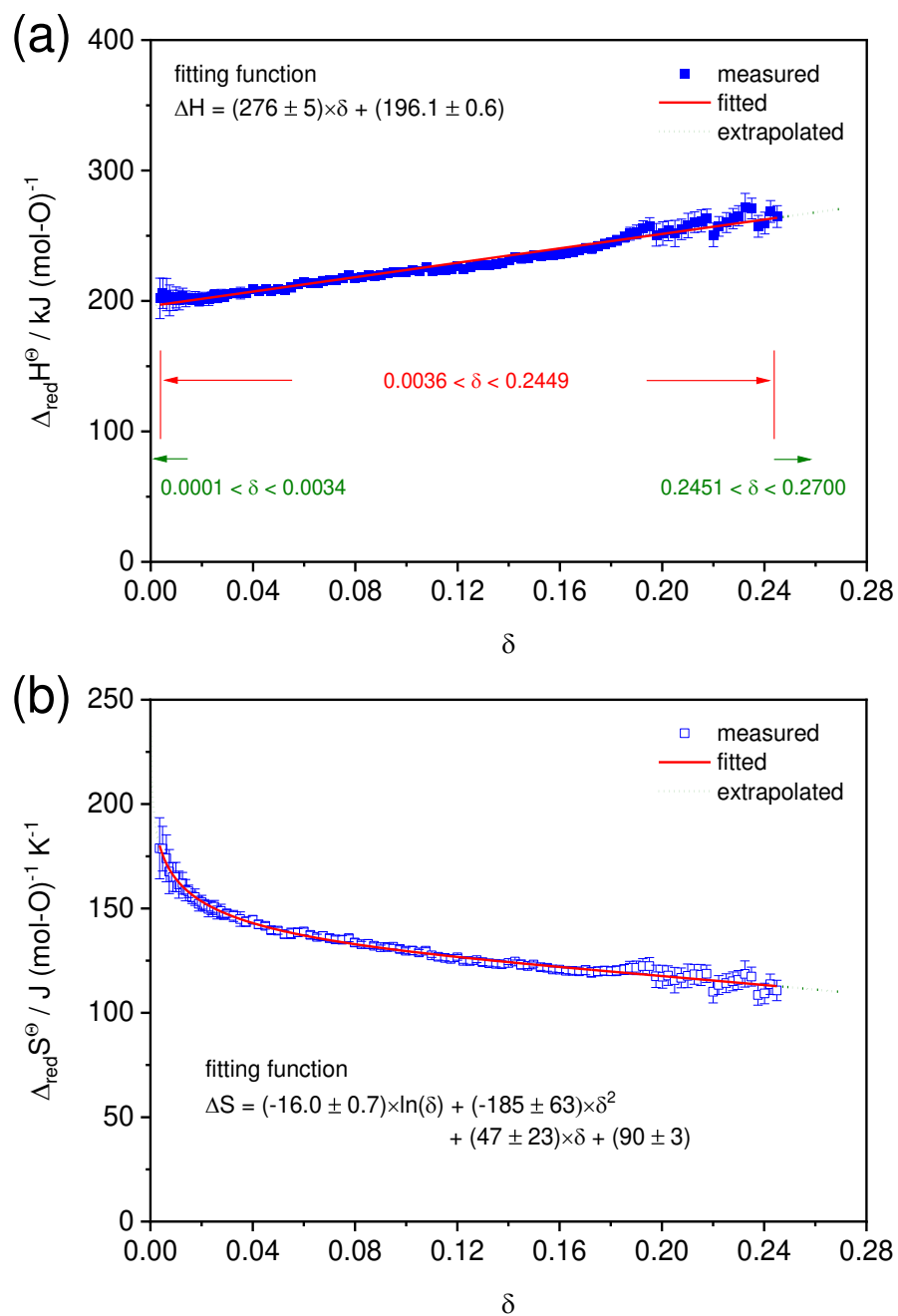
Figure S9. The experimentally measured (dots in blue color) and numerically fitted (solid lines in red color) thermodynamic properties: (a) enthalpy and (b) entropy of reduction in the range of $0.0036 < \delta < 0.2449$. The extrapolated (dash lines in olive color) enthalpy and entropy of reduction are calculated using corresponding fitting functions in the range of $0.0001 < \delta < 0.0034$ and $0.2451 < \delta < 0.2700$.
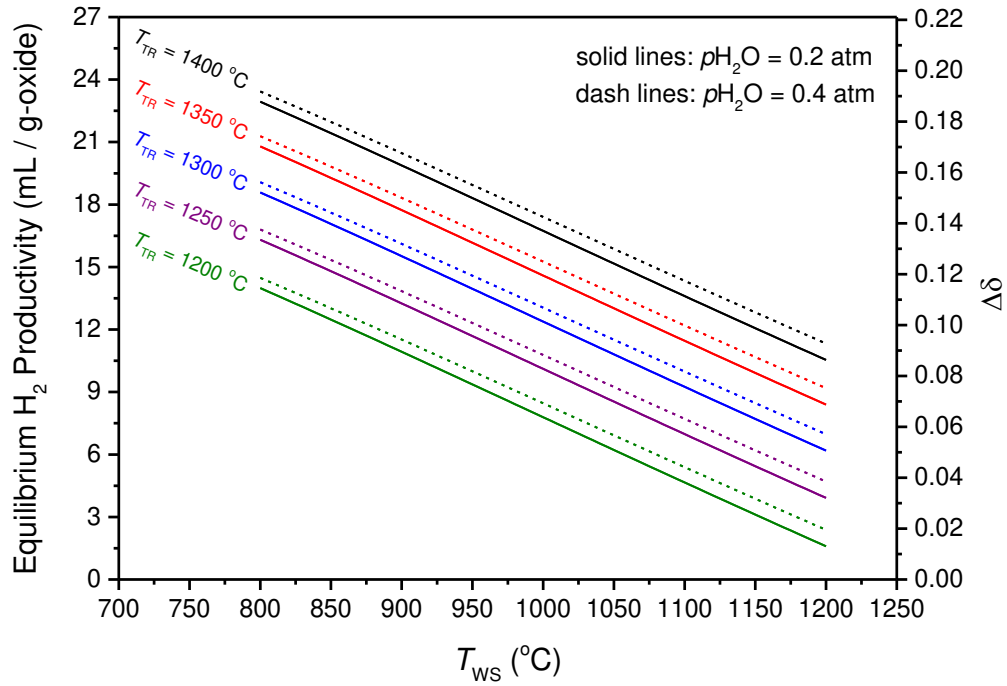
Figure S10. Predicted equilibrium fuel productivity of STM55 with thermal reduction under pO_2 = 1.0×10^{-5} atm at the temperatures indicated, and water splitting under pH_2O = 0.2 atm (solid lines) and 0.4 atm (dash lines), shown as functions of water splitting temperature.

Based on the fitted thermodynamic data of STM55 shown in Figure S9, it is possible to compute the non-stoichiometry at almost any arbitrary condition. Thus, the equilibrium fuel productivity – the quantity of hydrogen which results from allowing the oxide to react with the supplied gas for sufficiently long time that equilibrium is achieved – can be easily predicted for any given cycle. The equilibrium fuel productivities for cycles with thermal reduction carried out at temperatures between 1200 and 1400 ° and water splitting performed at a variable temperature, T_{WS}, between 800 and 1200 °C, using a steam partial pressure of either pH_2O = 0.2 or 0.4 atm, are shown in Figure S10. The near linear increase in equilibrium fuel productivity with decreasing T_{WS} reflects the fact that STM55 cannot reach full re-oxidation under the conditions considered. It is also to be noted that with a decreasing T_{WS}, the benefits of using a gas with a high steam content diminish as a consequence of the decreasing oxidation potential of steam at low temperatures.
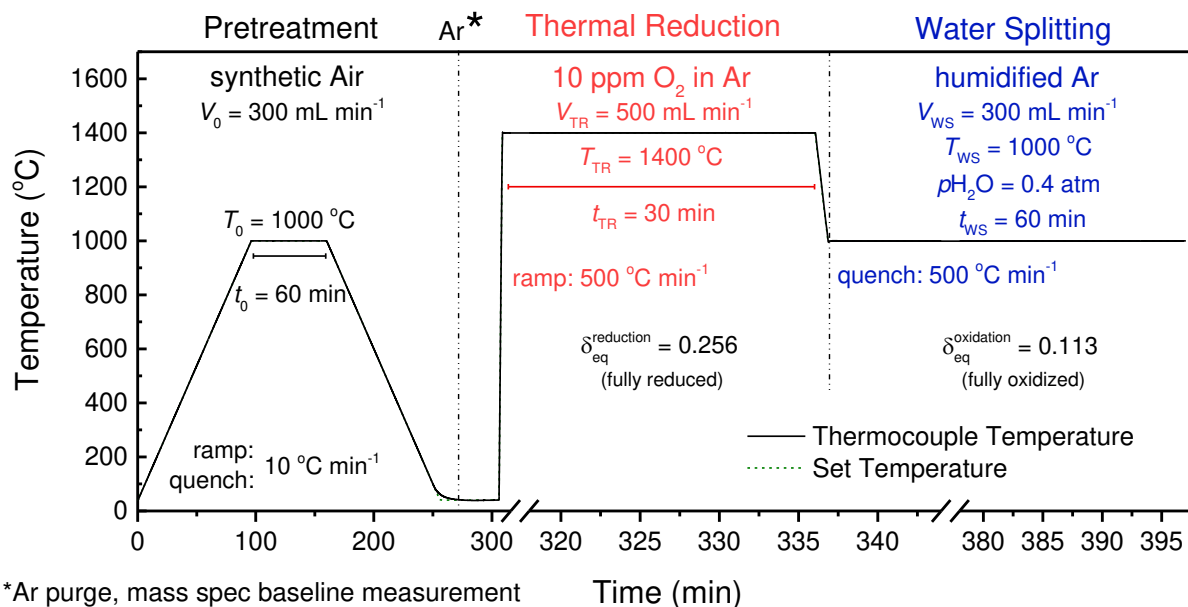
Figure S11. Temperature and gas profile (nominal) used for evaluating the thermo-kinetic response of STM55 perovskite during thermal reduction and subsequent oxidation by steam in a single-cycle experiment, using a sample 0.5225 g in mass.

To permit evaluation of the thermo-kinetic response of STM55, a thermochemical cycle with the temperature and gas profiles shown in Figure S11 was carried out using a porous cylindrical monolith sample with a mass of 0.5225 g. An initial pretreatment of the sample was carried out at $T_0 = 1000$ °C for 60 min under a flow rate of $V_0 = 300$ mL min^{-1} synthetic air and cooled to 25 °C at a rate of 10 °C min^{-1}, to ensure that the cycle was initiated with the material in the fully oxidized state. Subsequent to pretreatment, gas lines were purged with Ar (residual O_2 on the order of a few ppm). At the sample temperature of 25 °C this step does not induce reduction. Following the brief room temperature exposure to Ar, the reduction sweep gas of 10 ppm O_2 in Ar ($V_{TR} = 500$ mL min^{-1}) was introduced, and the O_2 and H_2 baseline signals in mass spectrometer were measured, as was the oxygen partial pressure. Upon stabilization of these signals (~30 min), the measured pO_2 was recorded and taken as the true experimental input value. The sample was then heated at a ramp rate of 500 °C min^{-1} to the reduction temperature, T_{TR} (here, set value of 1400 °C, actual value of 1404 °C) and held at T_{TR} for a reduction period, t_{TR}, of 30 min. In the first minute of the < 3 min

reduction period, the average temperature of the sample slightly exceeded that recorded at the thermocouple, as evidenced by slight oxygen release initiating at a thermocouple temperature of 450 °C. Upon completion of the reduction half-cycle, the sample was quenched at a ramp rate of 500 °C min^{-1} to the water splitting temperature, T_{WS}, of 1000 °C. During the quench process, the thermocouple temperature lagged very slightly behind the set temperature. Once the thermocouple temperature reached T_{WS}, the oxidation gas with a set water partial pressure, $p\mathrm{H_2O}$, and set flow rate, V_{WS}, was introduced and the sample held at this condition for a given reaction time, t_{WS}, of 60 min. The equilibrium oxygen non-stoichiometry values under the given reduction and oxidation half-cycles under nominal conditions are 0.256 and 0.113, respectively.
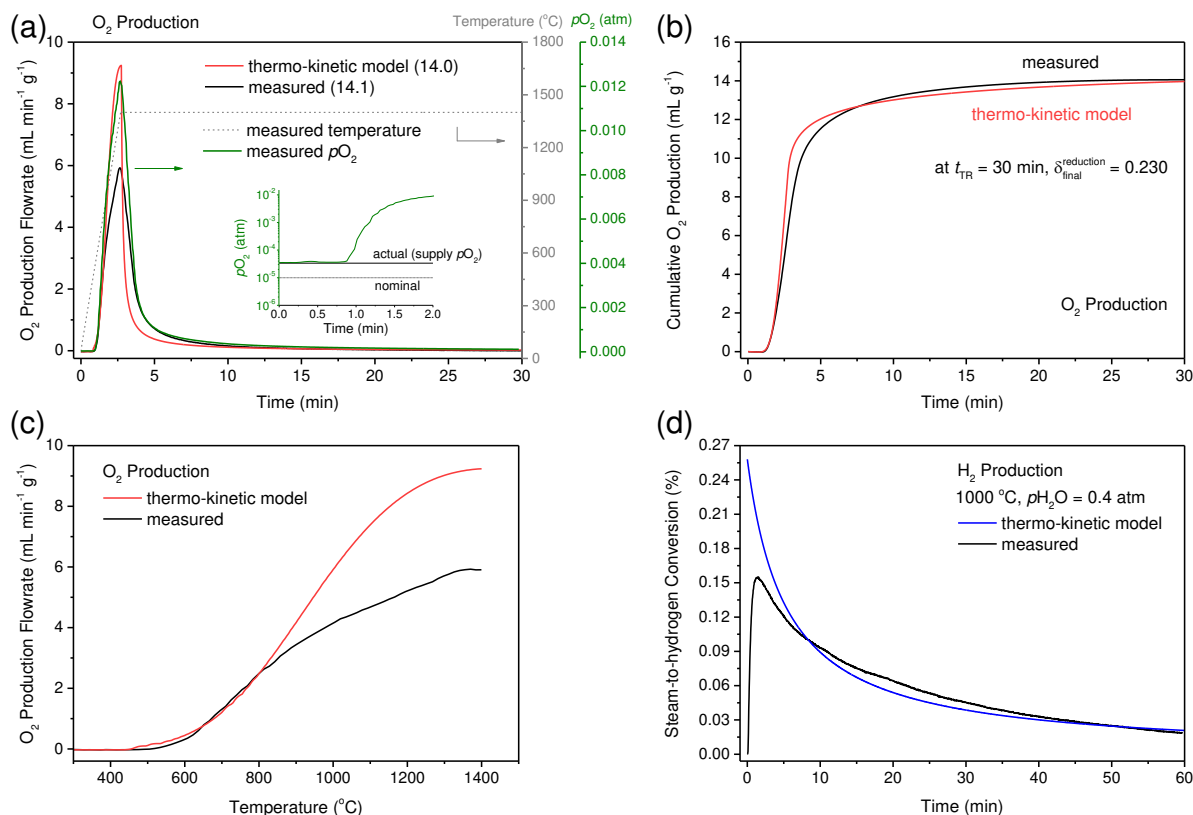
Figure S12. Evaluation of gas evolution characteristics of STM55 by the comparison of the measured and thermodynamically predicted behavior of a porous sample 0.5225 g in mass using the nominal conditions described in Figure S11: (a) instantaneous oxygen production profile along with the pO$_2$ profile recorded by an oxygen sensor and the temperature profile measured by thermocouple, and (b) cumulative oxygen production profile; in both (a) and (b) experimental results are compared to thermo-kinetic model calculations for a thermal reduction temperature of 1400 °C and oxygen partial pressure of 33.5 ppm. The inset data in (a) shows the measured pO$_2$ at the initiation of the reduction experiment. (c) Comparison of measured and predicted oxygen evolution as a function of temperature; (d) steam-to-hydrogen conversion profile. Calculation in (c) is performed at 1404 °C with the oxygen partial pressure of 33.5 ppm in the reduction, and corresponds to the initial ~2.7 min of oxygen release. Calculation of hydrogen production profile in (d) is performed at T_{WS} = 1000 °C, pH$_2$O = 0.4 atm under an Ar carrier gas flow rate of 300 mL min^{-1}.

From the detailed analysis of the gas evolution data in Figure S12 several conclusions can be drawn. The inset data in (a) shows the true inlet pO_2 to be 33.5×10^{-6} atm rather than nominal condition of 10×10^{-6} atm, the value recorded at the downstream sensor using an inlet gas stream of 10 ppm O_2 in Ar. The temperature recorded by the thermocouple during the reduction hold is 1400 °C. The true sample temperature and the thermocouple temperature can differ by a few degrees for a variety of experimental reasons. The calculations presented here show that an overshoot of 4 °C brings the measured O_2 release in alignment with the measured O_2 (compare Figure S12(b) above to Figure 5(b) in the main paper), but the differences for the two conditions are in any case small. On heating under the low pO_2 atmosphere, the experimentally measured and predicted oxygen evolution are in good agreement until the temperature reaches ~800 °C, Figure S12(c). As noted in the main text, the deviation at higher temperatures is a signature of process limited (or co-limited) by material kinetic factors. The steam-to-hydrogen conversion, Figure S12(d), displays a peak experimental value of around 0.155 %. The low steam-to-hydrogen conversion is attributed to the moderate driving force for water splitting half-cycle, which is a common challenge for perovskite-based STCH materials operated within the framework of non-stoichiometric oxygen release and uptake.
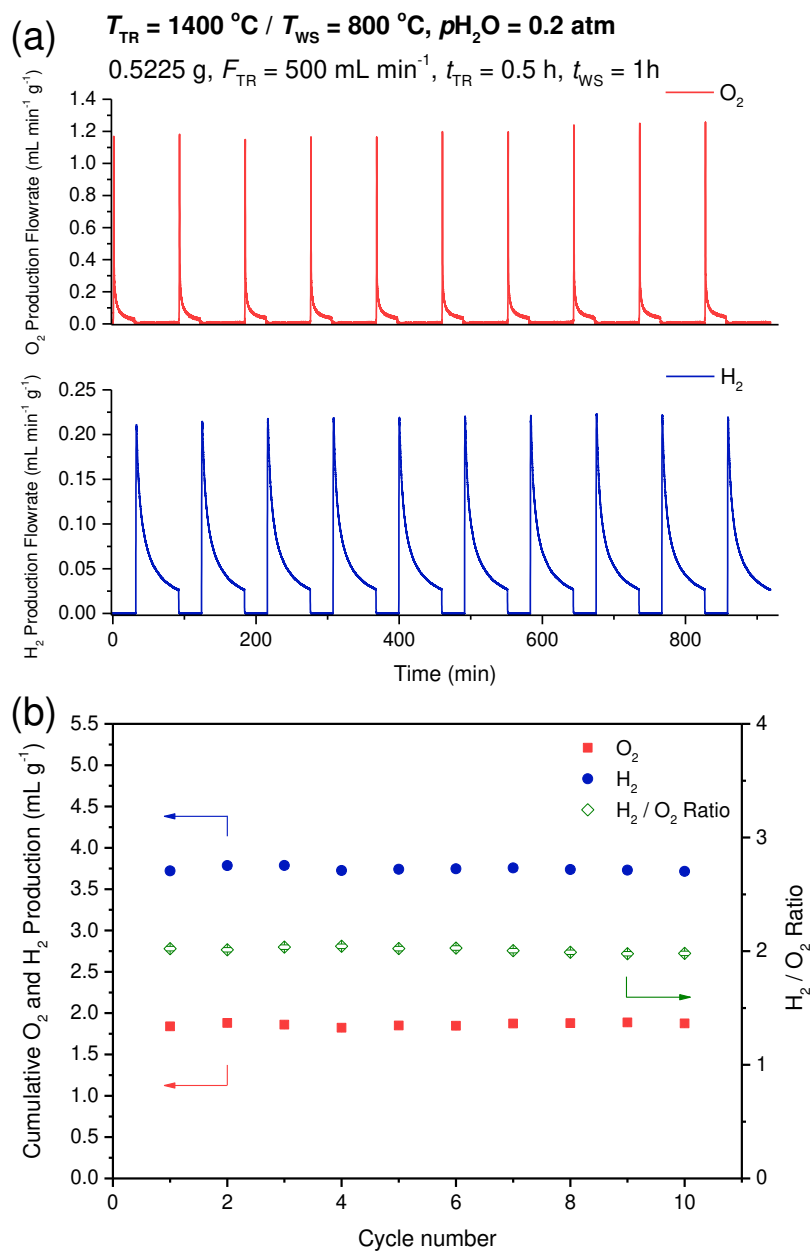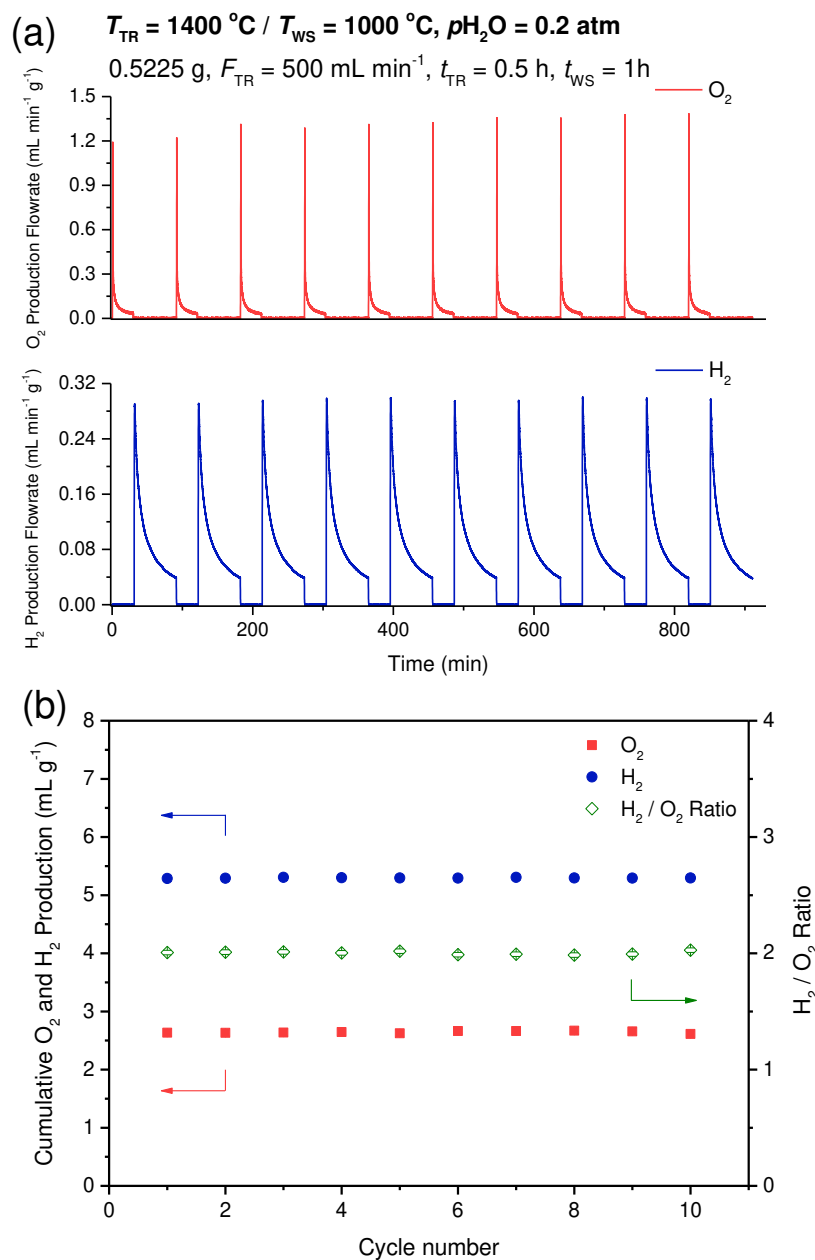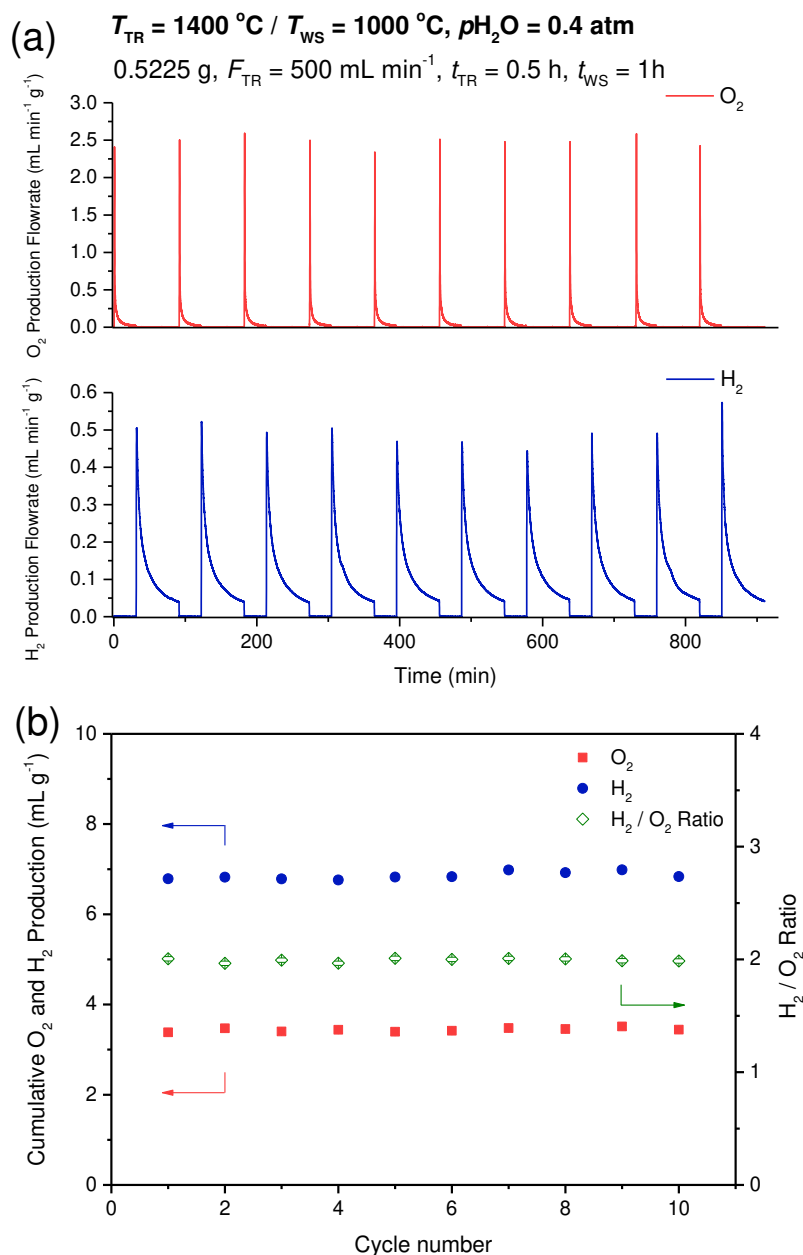
Figure S13. Thermochemical cycle using 0.5225 g STM55 porous monolith with reduction under a flowrate of 500 mL min^{-1} of 10 ppm O_2 in Ar at 1400 °C for 30 min and oxidation under a flowrate of 300 mL min^{-1} of Ar with $pH_2O = 0.2$ atm at 800 °C for 60 min: (a) 10 continuous cycles for thermochemical water splitting; (b) total amount of H_2 and O_2 production in each cycle and corresponding H_2 / O_2 ratio. Red, blue and olive colors correspond to O_2, H_2 production and H_2 / O_2 ratio, respectively.
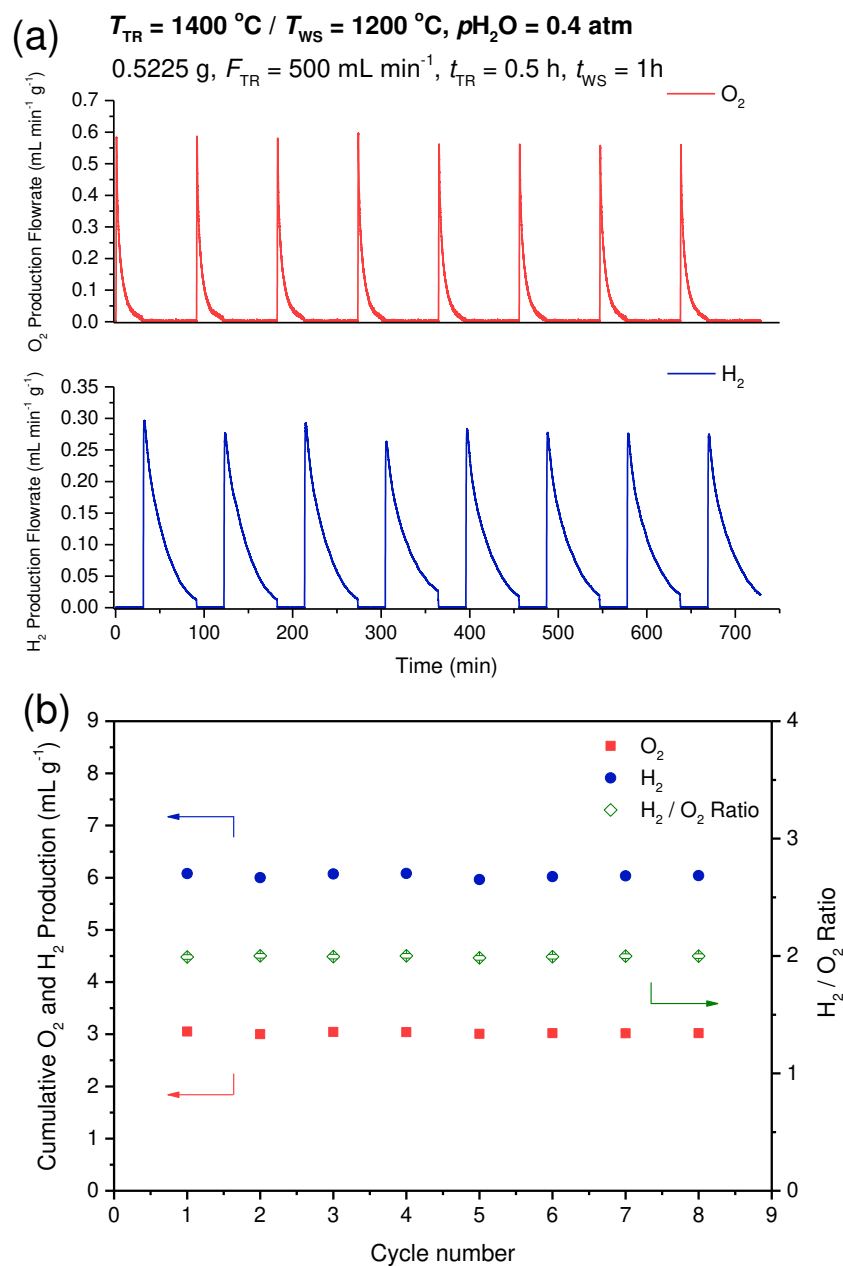
Figure S14. Thermochemical cycle using 0.5225 g STM55 porous monolith with reduction under a flowrate of 500 mL min^{-1} of 10 ppm O_2 in Ar at 1400 °C for 30 min and oxidation under a flowrate of 300 mL min^{-1} of Ar with $pH_2O = 0.2$ atm at 1000 °C for 60 min: (a) 10 continuous cycles for thermochemical water splitting; (b) total amount of H_2 and O_2 production in each cycle and corresponding H_2 / O_2 ratio. Red, blue and olive colors correspond to O_2, H_2 production and H_2 / O_2 ratio, respectively.

Figure S15. Thermochemical cycle using 0.5225 g STM55 porous monolith with reduction under a flowrate of 500 mL min^{-1} of 10 ppm O_2 in Ar at 1400 °C for 30 min and oxidation under a flowrate of 300 mL min^{-1} of Ar with $pH_2O = 0.4$ atm at 1000 °C for 60 min: (a) 10 continuous cycles for thermochemical water splitting; (b) total amount of H_2 and O_2 production in each cycle and corresponding H_2 / O_2 ratio. Red, blue and olive colors correspond to O_2, H_2 production and H_2 / O_2 ratio, respectively.
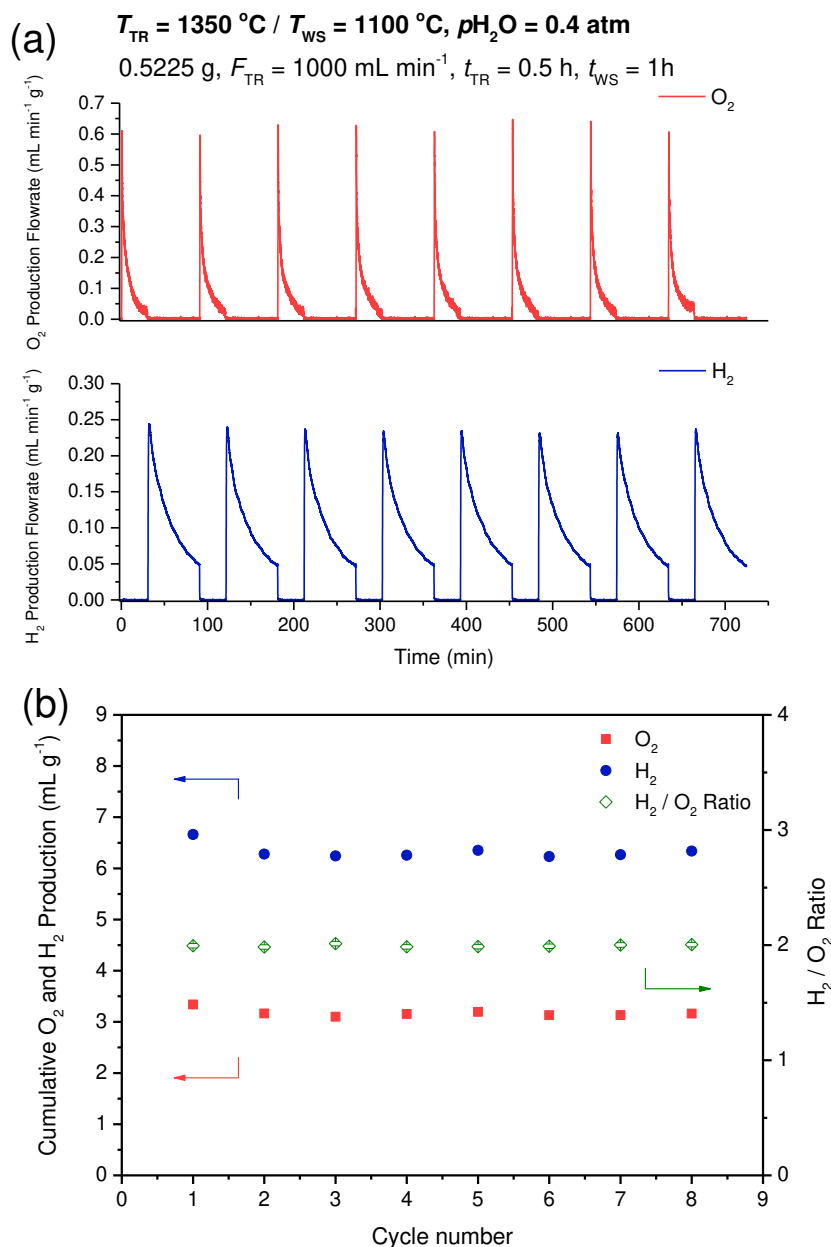
Figure S16. Thermochemical cycle using 0.5225 g STM55 porous monolith with reduction under a flowrate of 500 mL min^{-1} of 10 ppm O_2 in Ar at 1400 °C for 30 min and oxidation under a flowrate of 300 mL min^{-1} of Ar with $pH_2O = 0.4$ atm at 1200 °C for 60 min: (a) 8 continuous cycles for thermochemical water splitting; (b) total amount of H_2 and O_2 production in each cycle and corresponding H_2 / O_2 ratio. Red, blue and olive colors correspond to O_2, H_2 production and H_2 / O_2 ratio, respectively.
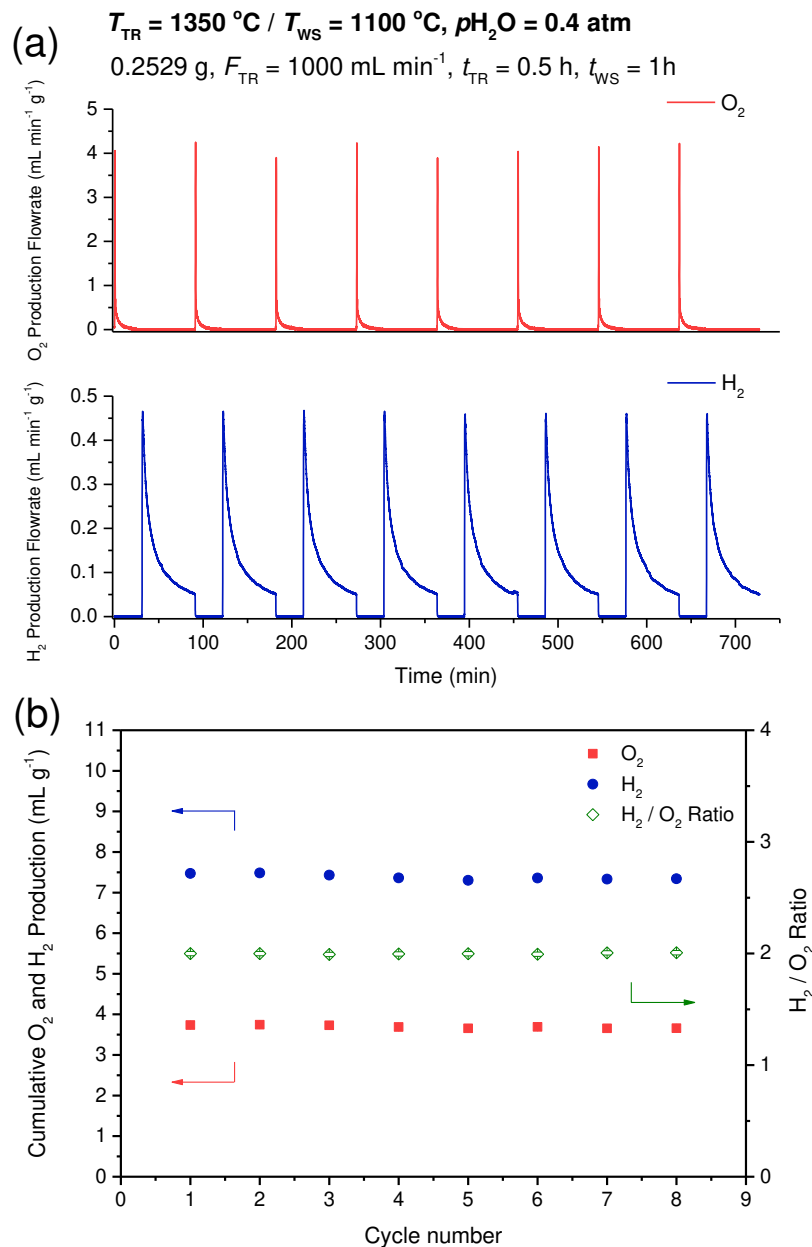
Figure S17. Thermochemical cycle using sintered STM55 porous monolith with reduction under a flowrate of 1000 mL min^{-1} (0.5225 g, oxide mass normalized flowrate 1914 mL min^{-1} g^{-1}) of 10 ppm O_2 in Ar at 1350 °C for 30 min and oxidation under a flowrate of 300 mL min^{-1} of Ar with $pH_2O = 0.4$ atm at 1100 °C for 60 min: (a) 8 continuous cycles for thermochemical water splitting; (b) total amount of H_2 and O_2 production in each cycle and corresponding H_2 / O_2 ratio. Red, blue and olive colors correspond to O_2, H_2 production and H_2 / O_2 ratio, respectively.
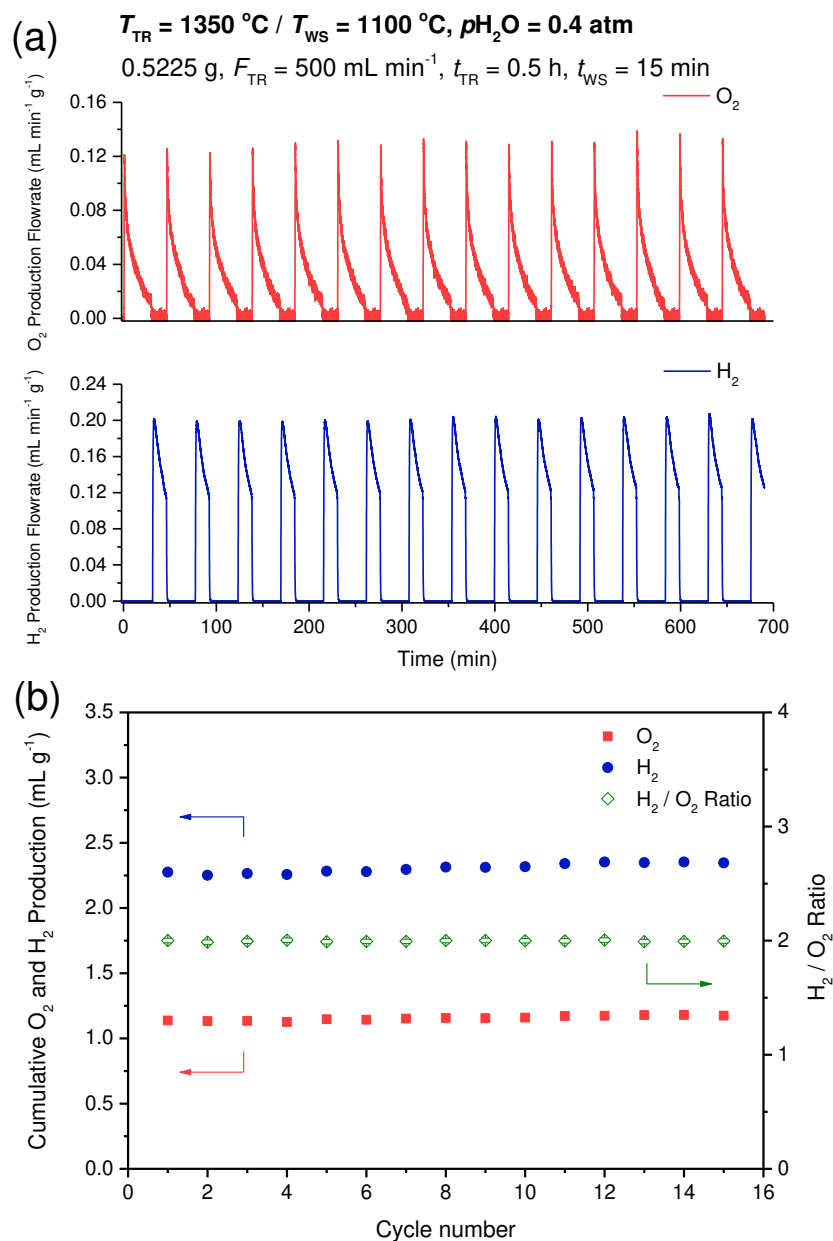
Figure S18. Thermochemical cycle using sintered STM55 porous monolith with reduction under a flowrate of 1000 mL min^{-1} (0.2529 g, oxide mass normalized flowrate 3954 mL min^{-1} g^{-1}) of 10 ppm O_2 in Ar at 1350 °C for 30 min and oxidation under a flowrate of 300 mL min^{-1} of Ar with $pH_2O = 0.4$ atm at 1100 °C for 60 min: (a) 8 continuous cycles for thermochemical water splitting; (b) total amount of H_2 and O_2 production in each cycle and corresponding H_2 / O_2 ratio. Red, blue and olive colors correspond to O_2, H_2 production and H_2 / O_2 ratio, respectively.
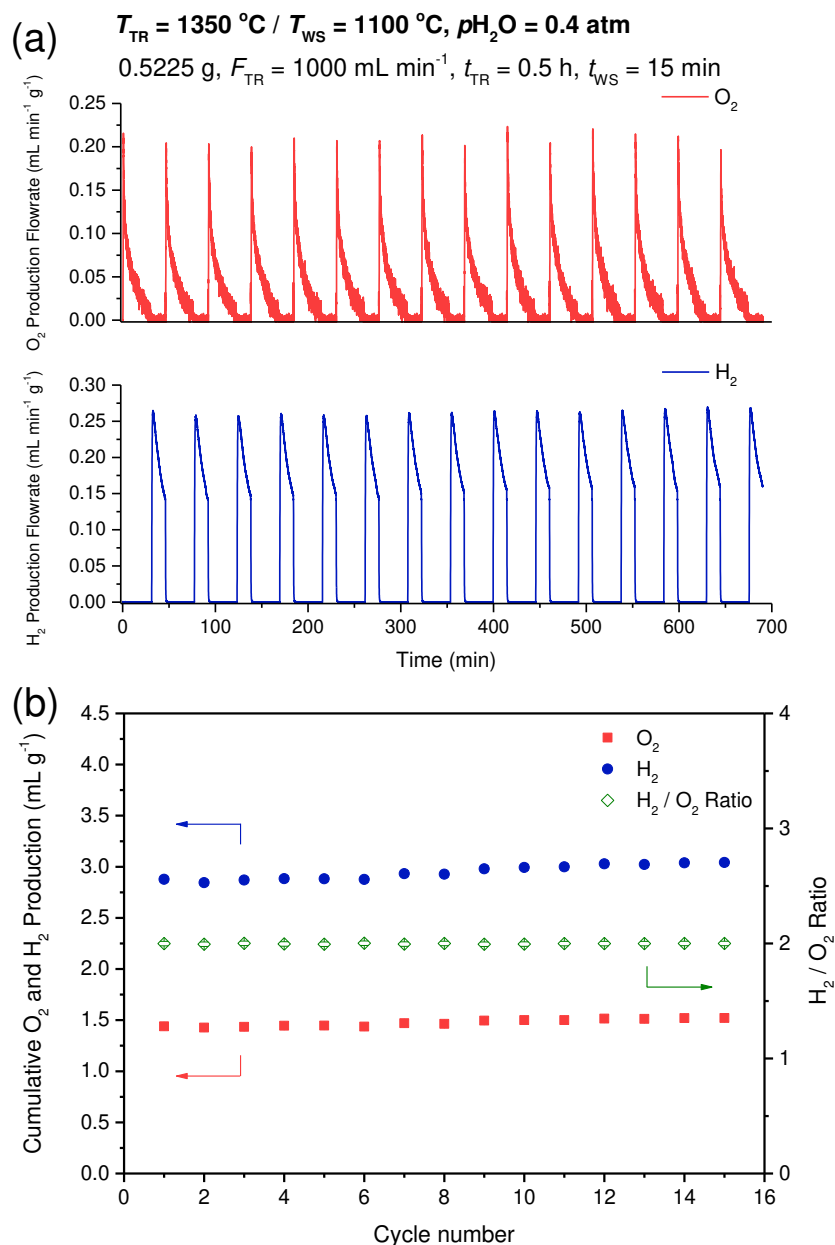
Figure S19. Thermochemical cycle using sintered STM55 porous monolith with reduction under a flowrate of 500 mL min^{-1} (0.5225 g, oxide mass normalized flowrate 957 mL min^{-1} g^{-1}) of 10 ppm O_2 in Ar at 1350 °C for 30 min and oxidation under a flowrate of 300 mL min^{-1} of Ar with $pH_2O = 0.4$ atm at 1100 °C for 15 min: (a) 15 continuous cycles for thermochemical water splitting; (b) total amount of H_2 and O_2 production in each cycle and corresponding H_2 / O_2 ratio. Red, blue and olive colors correspond to O_2, H_2 production and H_2 / O_2 ratio, respectively.

Figure S20. Thermochemical cycle using sintered STM55 porous monolith with reduction under a flowrate of 1000 mL min^{-1} (0.5225 g, oxide mass normalized flowrate 1914 mL min^{-1} g^{-1}) of 10 ppm O_2 in Ar at 1350 °C for 30 min and oxidation under a flowrate of 300 mL min^{-1} of Ar with $pH_2O = 0.4$ atm at 1100 °C for 15 min: (a) 15 continuous cycles for thermochemical water splitting; (b) total amount of H_2 and O_2 production in each cycle and corresponding H_2 / O_2 ratio. Red, blue and olive colors correspond to O_2, H_2 production and H_2 / O_2 ratio, respectively.
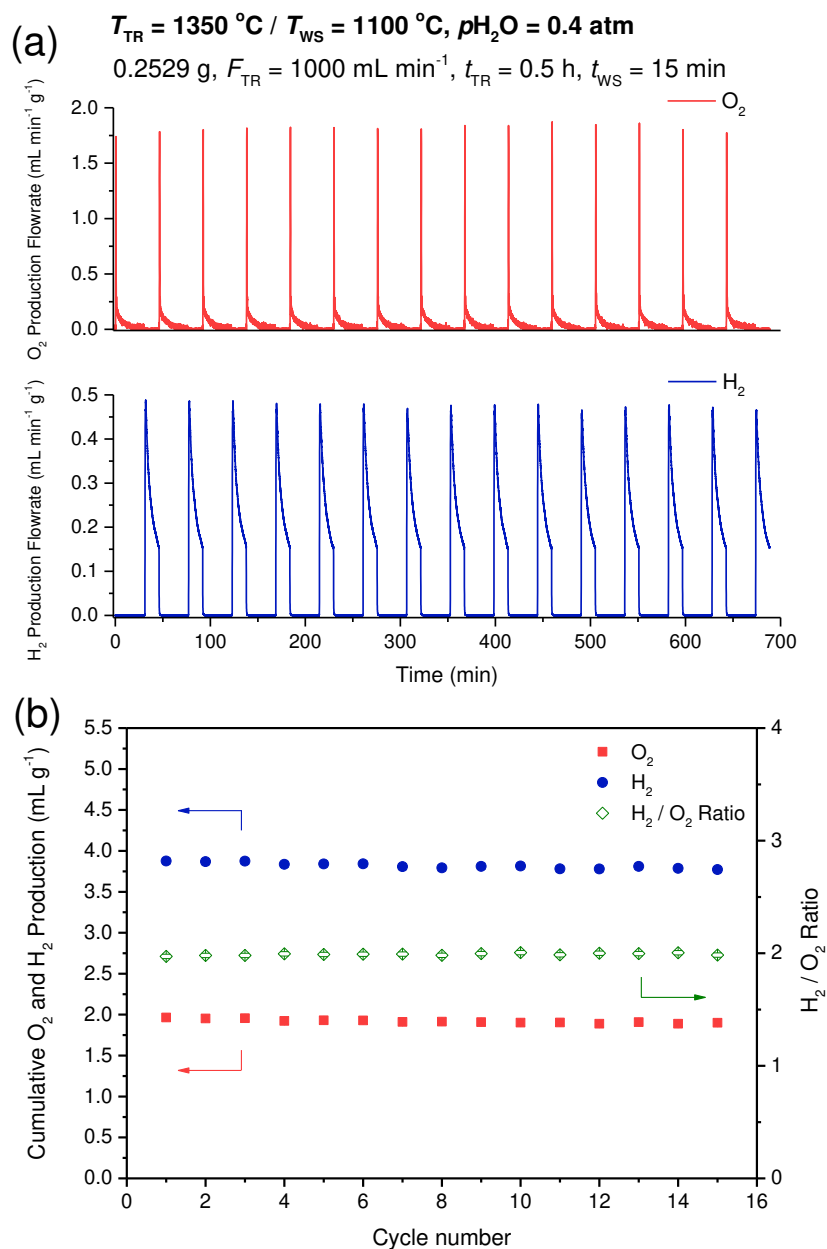
Figure S21. Thermochemical cycle using sintered STM55 porous monolith with reduction under a flowrate of 1000 mL min^{-1} (0.2529 g, oxide mass normalized flowrate 3954 mL min^{-1} g^{-1}) of 10 ppm O_2 in Ar at 1350 °C for 30 min and oxidation under a flowrate of 300 mL min^{-1} of Ar with $pH_2O = 0.4$ atm at 1100 °C for 15 min: (a) 15 continuous cycles for thermochemical water splitting; (b) total amount of H_2 and O_2 production in each cycle and corresponding H_2 / O_2 ratio. Red, blue and olive colors correspond to O_2, H_2 production and H_2 / O_2 ratio, respectively.
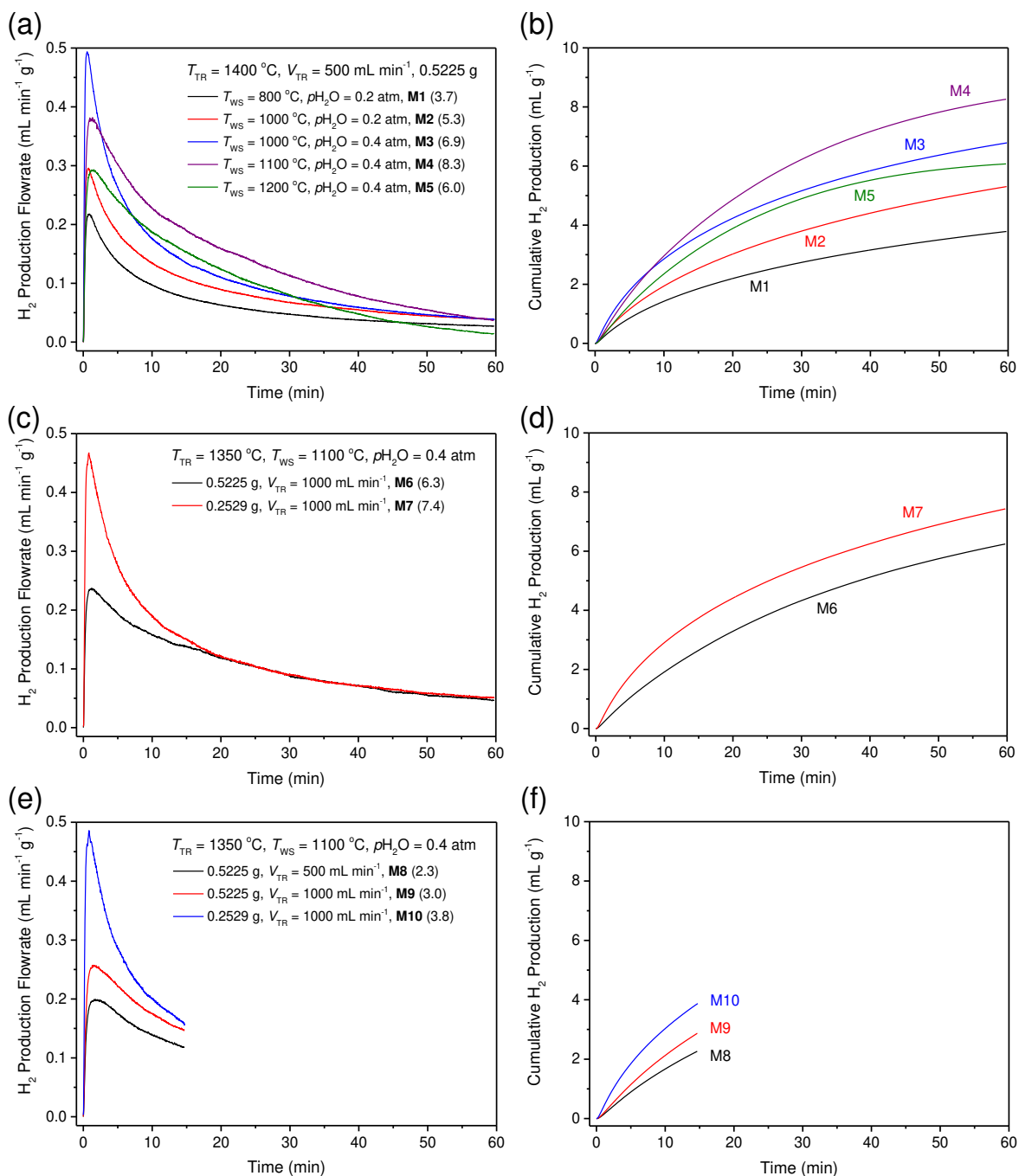
Figure S22. Experimental H_2 production profiles: (a), (c), (e) the instantaneous H_2 production flowrate; (b), (d), (f) the cumulative H_2 productivity over sintered STM55 porous monolith sample for thermochemical experiments described in Table 2. (a) and (b) show associated H_2 production in oxidation half-cycles under the impact of changing water splitting temperature and steam partial pressure with thermal reduction conditions held fixed; (c), (d) and (e), (f) show the associated H_2

production in oxidation half-cycles under the impact of varying the oxide mass, the reduction gas flow rate and the oxidation time. Shown in parentheses (mL g^{-1}) in (a) (c) and (e) is the total amount of H$_2$ generated per cycle under indicated conditions.

The repeated multiple-cycle water splitting experiments with short cycle time (t_{Total} = 90 min) were measured under ten different conditions, results of both H$_2$ and O$_2$ production are summarized in Table 2. Shown in Figure S22(a,b) is the H$_2$ production profiles under conditions of M1 – M5, in which 0.5225 g oxide is reduced under a fixed thermal reduction condition at 1400 °C under 10 ppm O$_2$ gas flow rate of 500 mL min^{-1} for 30 min followed by a series of oxidation temperatures and steam partial pressures, the peak H$_2$ productivity is achieved at T_{WS} = 1100 °C and pH$_2$O = 0.4 atm which is suggestive of the optimal water splitting condition. For thermochemical cycling carried out at a reduced reduction temperature of 1350 °C, the impact of the oxide mass (0.5225 or 0.2529 g), the reduction gas flow rate (500 or 1000 mL min^{-1}) and the oxidation time (60 or 15 min) on hydrogen production are evaluated, the associated H$_2$ production profiles measured with oxidation for 60 min (M6 – M7) and 15 min (M8 – M10) are shown in Figure S22(c,d) and S22(e,f), respectively. In both sets of experiments, it is demonstrated that the H$_2$ productivity increases with oxide mass-normalized gas flow rate, which is consistent with that implied by the thermo-kinetic model and is suggestive of the gas-phase as a rate-limiting factor in hydrogen production.
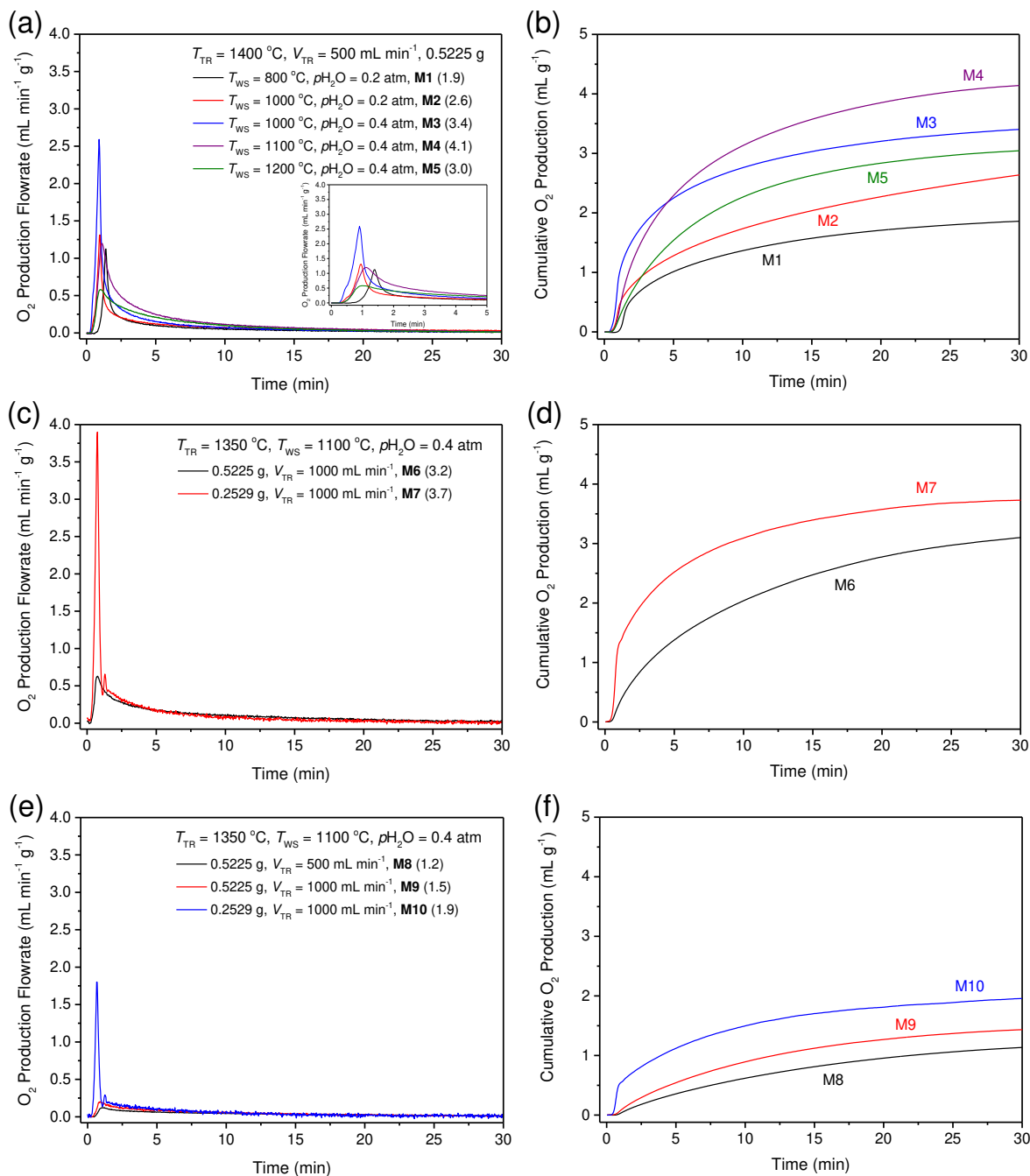
Figure S23. Experimental oxygen production profiles: (a), (c), (e) the instantaneous O_2 production flowrate; (b), (d), (f) the cumulative O_2 productivity over sintered STM55 porous monolith sample for thermochemical experiments described in Table 2. (a) and (b) show associated O_2 production in thermal reduction half-cycles under the impact of changing water splitting temperature and steam partial pressure in oxidation half-cycles; (c), (d) and (e), (f) show associated O_2 production

in thermal reduction half-cycles under the impact of varying the oxide mass, the reduction gas flow rate and the oxidation time. Shown in parentheses (mL g^{-1}) in (a) (c) and (e) is the total amount of O_2 generated per cycle under indicated conditions.

The cumulative O_2 production in the ten water splitting experiments are shown in Figure S23(a,b) (M1 – M5), Figure S23(c,d) (M6 – M7) and Figure S23(e,f) (M8 – M10). From M1 to M5, the O_2 productivity achieves the maximum amount under conditions of M4, in which the H_2 productivity is the highest. From the O_2 production profiles measured by varying the oxide mass normalized gas flow rate and oxidation time, M6 – M10, the O_2 productivity increases with mass-normalized gas flow rate, suggesting that the gas-phase thermodynamics are playing an important role in the rate-limiting steps in oxygen production.
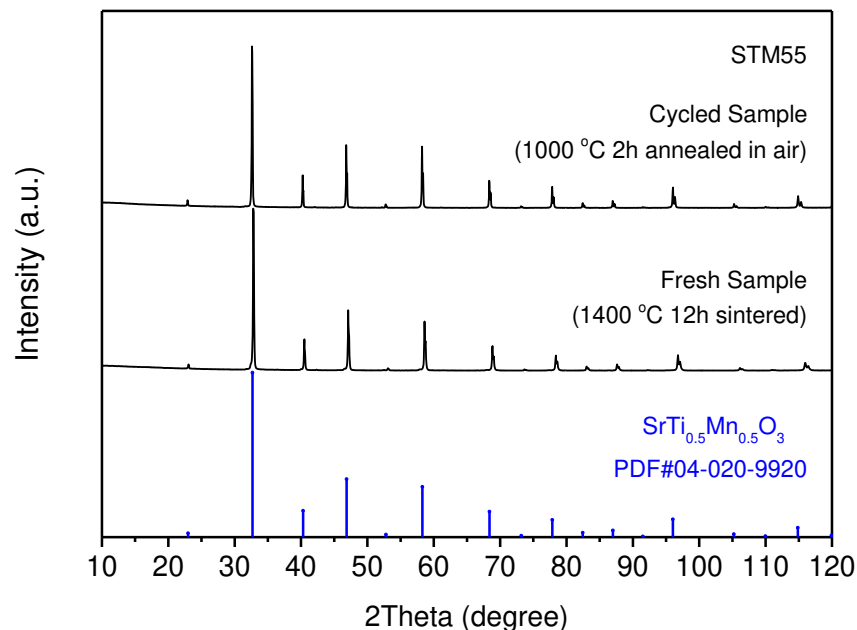
Figure S24. Ex situ X-ray diffraction patterns of STM55 porous monolith sample before and after all thermochemical water splitting measurements, the cycled sample was annealed at 1000 °C for 2 h under still air to achieve a fully oxidized state prior to diffraction measurement.

On the basis of XRD patterns collected on STM55 porous monolith sample before and after these thermochemical hydrogen production measurements, Figure S24, the STM55 sample is revealed to remain in the single-phase cubic crystal structure without any evidence of phase decomposition, suggesting the exceptional phase stability of STM55 under thermochemical cycling conditions. The refined lattice constants given by Rietveld refinement analysis of the XRD patterns before and after water splitting experiments are a = 3.8548(1) Å and a = 3.8762(3) Å, respectively. In addition, the SEM characterizations of the microstructures of porous monolith before and after all water splitting tests, Figure 7, shows that the porous structure with a solid-state diffusion distance of several microns is largely retained, however, an obvious coarsening of the grains is observed after long-term hydrogen production measurements. Overall, the exceptional phase stability, robust porous structure against high temperatures and high capacity hydrogen production renders STM55 perovskite a promising candidate for solar thermochemical fuel production.

References

1.   Blöchl, P. E., Projector augmented-wave method. *Physical Review B* **1994,** 50, (24), 17953-17979.

2.   Kresse, G.; Joubert, D., From ultrasoft pseudopotentials to the projector augmented-wave method. *Physical Review B* **1999,** 59, (3), 1758-1775.

3.   Kresse, G.; Furthmüller, J., Efficient iterative schemes for ab initio total-energy calculations using a plane-wave basis set. *Physical Review B* **1996,** 54, (16), 11169-11186.

4.   Kresse, G.; Furthmüller, J., Efficiency of ab-initio total energy calculations for metals and semiconductors using a plane-wave basis set. *Computational Materials Science* **1996,** 6, (1), 15-50.

5.   Perdew, J. P.; Burke, K.; Ernzerhof, M., Generalized gradient approximation made simple. *Physical Review Letters* **1996,** 77, (18), 3865-3868.

6.   Dudarev, S. L.; Botton, G. A.; Savrasov, S. Y.; Humphreys, C. J.; Sutton, A. P., Electron-energy-loss spectra and the structural stability of nickel oxide: An LSDA+U study. *Physical Review B* **1998,** 57, (3), 1505-1509.

7.   Wang, L.; Maxisch, T.; Ceder, G., Oxidation energies of transition metal oxides within the GGA+U framework. *Physical Review B* **2006,** 73, (19), 195107.

8.   Grindy, S.; Meredig, B.; Kirklin, S.; Saal, J. E.; Wolverton, C., Approaching chemical accuracy with density functional calculations: Diatomic energy corrections. *Physical Review B* **2013,** 87, (7), 075150.

9.   Toby, B. H.; Von Dreele, R. B., GSAS-II: the genesis of a modern open-source all purpose crystallography software package. *Journal of Applied Crystallography* **2013,** 46, (2), 544-549.

10.   Daoud-Aladine, A.; Martin, C.; Chapon, L. C.; Hervieu, M.; Knight, K. S.; Brunelli, M.; Radaelli, P. G., Structural phase transition and magnetism in hexagonal $SrMnO_3$ by magnetization measurements and by electron, x-ray, and neutron diffraction studies. *Physical Review B* **2007,** 75, (10), 104417.

11.   Yamanaka, T.; Hirai, N.; Komatsu, Y., Structure change of $Ca_{1-x}Sr_xTiO_3$ perovskite with

composition and pressure. *American Mineralogist* **2002,** 87, (8-9), 1183-1189.

12.   Qasim, I.; Kennedy, B. J., Structural characterization of the perovskite series $Sr_{1-x}La_xTi_{0.5}Mn_{0.5}O_3$. *Journal of Solid State Chemistry* **2013,** 200, 39-42.

13.   Meher, K. R. S. P.; Savinov, M.; Kamba, S.; Goian, V.; Varma, K. B. R., Structure, dielectric, and magnetic properties of Sr_2TiMnO_6 ceramics. *Journal of Applied Physics* **2010,** 108, (9), 094108.

14.   Álvarez-Serrano, I.; Arillo, M. Á.; García-Hernández, M.; López, M. L.; Pico, C.; Veiga, M. L., Microstructural origin of magnetic and giant dielectric behavior of $Sr_2MnTiO_{6-\delta}$ perovskite nanocrystals. *Journal of the American Ceramic Society* **2010,** 93, (8), 2311-2319.

15.   Momma, K.; Izumi, F., VESTA 3 for three-dimensional visualization of crystal, volumetric and morphology data. *Journal of Applied Crystallography* **2011,** 44, (6), 1272-1276.

16.   Akhtar, M. J.; Akhtar, Z.-U.-N.; Jackson, R. A.; Catlow, C. R. A., Computer simulation studies of strontium titanate. *Journal of the American Ceramic Society* **1995,** 78, (2), 421-428.

17.   Hao, Y.; Yang, C.-K.; Haile, S. M., Ceria–zirconia solid solutions ($Ce_{1-x}Zr_xO_{2-\delta}$, $x \leq 0.2$) for solar thermochemical water splitting: a thermodynamic study. *Chemistry of Materials* **2014,** 26, (20), 6073-6082.